Data-driven time-frequency analysis of multivariate data

by
Naveed ur Rehman

A Thesis submitted in fulfilment of requirements for the degree of Doctor of Philosophy of Imperial College London

Communications and Signal Processing Group
Department of Electrical and Electronic Engineering
Imperial College London
November 2011

Abstract

Empirical Mode Decomposition (EMD) is a data-driven method for the decomposition and time-frequency analysis of real world nonstationary signals. Its main advantages over other time-frequency methods are its locality, data-driven nature, multiresolution-based decomposition, higher time-frequency resolution and its ability to capture oscillation of any type (nonharmonic signals). These properties have made EMD a viable tool for real world nonstationary data analysis.

Recent advances in sensor and data acquisition technologies have brought to light new classes of signals containing typically several data channels. Currently, such signals are almost invariably processed channel-wise, which is suboptimal. It is, therefore, imperative to design multivariate extensions of the existing nonlinear and nonstationary analysis algorithms as they are expected to give more insight into the dynamics and the interdependence between multiple channels of such signals.

To this end, this thesis presents multivariate extensions of the empirical mode decomposition algorithm and illustrates their advantages with regards to multivariate nonstationary data analysis. Some important properties of such extensions are also explored, including their ability to exhibit wavelet-like dyadic filter bank structures for white Gaussian noise (WGN), and their capacity to align similar oscillatory modes from multiple data channels. Owing to the generality of the proposed methods, an improved multivariate EMD-based algorithm is introduced which solves some inherent problems in the original EMD algorithm. Finally, to demonstrate the potential of the proposed methods, simulations on the fusion of multiple real world signals (wind, images and inertial body motion data) support the analysis.

Acknowledgment

First and foremost, I would like to acknowledge my supervisor Professor Danilo Mandic for his consistent support and help throughout my PhD. I always found him willing to discuss any problems which I encountered during my work and give his insightful comments into my research. My discussions with him over the course of my PhD has definitely made me a better researcher. I appreciate all his contributions of time, ideas, and financial support to make my PhD experience productive and enjoyable.

I would also like to thank my fellow PhD students and post-graduate researchers, in the Communications and Signal Processing group at Imperial College, who have contributed immensely to making my time at Imperial a success. In particular, I am very grateful to Dr. Clive Cheong Took for being a wonderful friend over the years. I am also thankful to Dr. David Looney, Dr. Ling Li and Cheolsoo Park whom I worked with on different aspects of Empirical Mode Decomposition algorithm. It is due to our fruitful collaboration, under with the supervision of Dr. Danilo Mandic, that our group is currently leading in this field.

I would also like to acknowledge my sponsors Higher Education Commission (HEC), Government of Pakistan, for funding my PhD studies. During the four years of my PhD studies, HEC never delayed paying my monthly stipend and yearly tuition fee for which I am truly grateful.

Most Importantly, I would like to thank my mother and father; my wife, Usara; and my brothers, Ubaid and Khawar, for their support and patience through out my PhD work. I would not have finished my degree without their help!

Contents

List of Figures

Statement of Originality

I declare that this is an original thesis and it is entirely based my own work. I acknowledge the sources in every instance where I used the ideas of other writers, where I used any diagrams or visuals, I acknowledged the source in every instance. This thesis was not and will not be submitted to any other university or institution for fulfilling the requirements of a degree.

List of Symbols

$a(t)/a(k)$:	amplitude function continuous time/discrete time
$c_m(k)$:	mth IMF
Cov :	covariance function
$d(k)$:	high frequency oscillatory part in the EMD sifting process
$e_{max}(t)/e_{min}(t)$:	upper/lower envelope function
$f(t)$:	input function (continuous time)
$f(k)$:	evaluation function in EMD sifting process
$F(x, y)$:	fused image
H :	Hurst exponent
k/K :	time index/total number of samples
$m(t)/m(k)$:	local mean function continuous time/discrete time
$p_\theta(t)$:	Projected signal along direction θ
$q(t)$:	quaternion signal
$r(k)$:	residual signal from EMD
$S_H(f)$:	Power spectral density for Hurst exponent H
v/V :	index of direction vector/Total direction vectors
$w(k)$:	WGN series
$z(t)$:	complex function
$\mathrm{d}\Omega$:	differential solid angle
$\psi(t)$:	wavelet function
$\Upsilon(m, m')$:	Normalised cross-covariance measure between mth and m'th IMFs

List of Abbreviations

1D: 1-dimensional

2D: 2-dimensional

3D: 3-dimensional

AAFT: Amplitude Adjusted Fourier Transform

AM: Amplitude Modulation

CEEMD: Complementary ensemble empirical mode decomposition

CEMD: Complex Empirical Mode Decomposition

EEG: Electroencephalography

EMD: Empirical Mode Decomposition

fBm: Fractional Brownian Motion

FFT: Fast Fourier Transform

fGn: fractional Gaussian noise

FM: Frequency Modulation

iAAFT: iterative Amplitude Adjusted Fourier Transform

IMF: intrinsic mode function

MEMD: Multivariate Empirical Mode Decomposition

PSD: Power Spectral Density

STFT: Short-time Fourier Transform

TEMD: Trivariate Empirical Mode Decomposition

WGN: White Gaussian Noise

List of Publications

Book Chapters:

- **N. Rehman**, D. Looney, C. Park, and D. P. Mandic, "Adaptive Multiscale Analysis using Multivariate Empirical Mode Decomposition", *Springer Handbook on Bio- and Neuro-Informatics*, Springer. October, 2011. (Submitted)

Referred Journals:

- C. Park, D. Looney, **N. Rehman**, and D. P. Mandic, "Motor Imagery signal classification using Multivariate Empirical Mode Decomposition", *Submitted to IEEE Transactions on Rehabilitation and Neural Engineering*, 2011.

- **N. Rehman** and D. P. Mandic, "Filter bank property of Multivariate Empirical Mode Decomposition", *IEEE Transactions on Signal Processing*, vol. 59, no. 5, pp. 1059-1068, 2011.

- **N. Rehman** and D. P. Mandic, "Multivariate Empirical Mode Decomposition", *Proceedings of the Royal Society A*, vol. 466, no. 2117, pp. 1291-1302, 2010.

- **N. Rehman** and D. P. Mandic, "Empirical Mode Decomposition for Trivariate Signals", *IEEE Transactions on Signal Processing*, vol. 58, no. 3, pp. 1059-1068, 2010.

Conferences:

- M. U. Ahmed, N. Rehman, and D. P. Mandic, "An MEMD-based multiscale sample entropy method for nonlinear analysis" *Submitted to the Proceedings of the IEEE International Conference on Acoustic Speech and Signal Processing (ICASSP)*, 2012.

- L. Li, D. Looney, C. Park, **N. Rehman** and D. P. Mandic, "Power Independent EMG based Gesture Recognition for Robotics", *Accepted for publication in the Pro-*

ceedings of the International conference of the IEEE Engineering in Medicine and Biology society, 2011, Boston, USA.

- **N. Rehman** and D. P. Mandic, "Quadrivariate Empirical Mode Decomposition", *Proceedings of the IEEE World Congress of Computational Intelligence (WCCI)*, 2010, Barcelona, Spain.

- **N. Rehman** and D. P. Mandic, "Application of Multivariate Empirical Mode Decomposition for Seizure detection in EEG signals", *Proceedings of the International conference of the IEEE Engineering in Medicine and Biology society*, 2010, Buenos Aires, Argentina.

- **N. Rehman**, D. Looney, T.M. Rutkowski and D. P. Mandic, "Bivariate EMD based Image Fusion", *Proceedings of the IEEE Workshop on Statistical Signal Processing*, 2009, Cardiff, Wales, UK.

- **N. Rehman** and D. P. Mandic, "Qualitative analysis of rotational modes within three dimensional empirical mode decomposition", *Proceedings of the IEEE International Conference on Acoustic Speech and Signal Processing*, pp. 3449-3452, 2009.

- D. Looney, T. M. Rutkowski, A. Heidenreich, D. Beyer, **N. Rehman**, and D. P. Mandic, "Conditioning Multimodal Information for Smart Environments", *Proceedings of the ACM/IEEE International Conference on Distributed Smart Cameras*, Italy, 2009.

Chapter 1

Introduction

1.1 Background and Motivation

TRADITIONAL linear statistical inference methods are well established and form a powerful tool for time series analysis. Since their inception, these methods have extensively been used in diverse fields; for instance, in signal estimation and detection [1] [2] and time-frequency (TF) analysis [3]. However, besides the requirement that the input signal is obtained from a linear system, these methods also assume that the statistical characteristics (at least first and second order properties) of the signal do not change with time, a property known as (weak)stationarity.[1] These assumptions of linear systems and the stationarity of the input signal limit the effectiveness of these methods in most natural phenomena, as they mostly involve nonstationary data obtained from nonlinear sources.

Among these linear and stationary time series methods, the Fourier series has historically been the most established and popular tool for signal analysis. Using Fourier series, smooth and periodic functions in $\mathbb{R}$ can be expanded into a weighted sum of orthogonal sines and cosines (basis functions), whose frequencies are integral multiples of a fundamental frequency, determined from the period of the input signal. In other words, by using Fourier series, any periodic function can be fully specified via a set of coefficients (weights) of the sines and cosines (trignometric functions); these coefficients are calculated

[1] In more formal terms, a stationary signal is the one whose joint probability properties are independent of the time lag within the observation period of the whole signal.

based on the linear dependence of the original signal with their corresponding trignometric function, making the Fourier series a linear time series method.

The Fourier series uses global predefined functions (sines and cosines) as its basis which also makes it unsuitable for nonstationary signal analysis. Due to the choice of fixed basis functions, expansion through the Fourier series is achieved by projecting the input signal onto a set of predefined trignometric functions which may not accurately represent the signal in hand. Also, since these trignometric functions are defined globally (over the whole observation interval), the time information is lost in the Fourier transformed signal: by looking at the Fourier spectrum, one cannot tell at which precise instant a particular event took place. This problem is not relevant for stationary signals whose properties do not change over time, but for most real world signals, this is a major issue that must be addressed.

Furthermore, due to predefined basis functions, additional harmonic terms are more often required to approximate the input signal, causing the spread of signal energy over a wide frequency range. This, in turn, results in the introduction of physically meaningless harmonics in the corresponding spectral representation. For instance, while Fourier series can effectively deal with the pure sine function, addition of any perturbations in the fixed amplitude and/or frequency of the original signal will result in many spurious harmonics in the Fourier spectrum even though the perturbed signal is similar to the original signal with effectively the same frequency. This is due to the inflexibility in the choice of the basis functions being used in the Fourier analysis, and will continue to cause problems in other similar techniques which are based on projecting the input signal onto fixed a priori chosen basis functions.

To alleviate the problem of loss of time information in traditional Fourier analysis, Gabor came up with the idea of a Short-time Fourier Transform (STFT) method which effectively operates by sliding the Fourier window along the time axis, resulting in a time-frequency-amplitude distribution [4]. However, since the Fourier transform is being applied across multiple windows of same sizes along the time axis, one must at least align the data so as to ensure their stationarity within each window (piecewise stationarity); this

is difficult to achieve, especially in real world nonstationary signals. Moreover, the choice of window width, though crucial in estimating an accurate TF spectrum, poses conflicting requirements regarding time and frequency resolution: a narrower window localizes the signal in time better, however, a longer time series is required for a higher frequency resolution. Despite its shortcomings, STFT has attracted much attention in practical fields due to its ease of implementation via Fast Fourier Transform (FFT).

STFT adopts the same window length for all frequencies, which limits its resolution in both time and frequency. A wavelet-based approach corrects this deficiency by adopting a windowing technique with variable window lengths: wider windows are used to obtain more precise low frequency information and narrow windows for high frequency information. In wavelet analysis, a function is decomposed by scaled and translated copies of an a priori chosen finite length oscillating function, known as mother wavelet. Due to the flexibility in choosing the mother wavelet function, the wavelet transform has shown superiority over traditional Fourier methods, especially in representing signals with sharp peaks and discontinuities [5].

Though the wavelet transform is quite effective in performing local analysis, the method is still based on projecting the input signal on a fixed a priori chosen set of wavelets. Moreover, once a mother wavelet function is selected, it is used for the whole analysis. This may be problematic for nonstationary signals which do not correlate well linearly with the chosen wavelet kernel, resulting in unwanted harmonics in the resulting decomposition and TF spectrum.

Other methods for TF analysis employ quadratic time-frequency distributions which, unlike the Fourier and the wavelet transform, do not use predefined basis functions as templates. While these methods provide a more 'crisp' TF representation in certain cases, they also introduce cross-interference terms in multi-component signals, thus, making their TF distributions more complicated to analyse [6]. Though such interference can be mitigated to some extent by additional processing, this is not without introducing a blur in the resulting TF representation.

In scenarios involving nonstationary data, there are instances when the convenience

of choosing an a priori fixed set of basis functions, and their orthogonality (in strict sense), are less significant than the compactness and the physically meaningful nature of the expansion. To this end, it might be worth investigating a class of methods which may compromise the orthogonality and the choice of a fixed 'dictionary' of basis functions, but provide a more compact and physically meaningful representation of the signal in hand. This can be achieved by adopting a set of data-driven basis functions, where the expansion terms are chosen based on the input signal. This way, each expanded term is expected to carry significant information about the input signal in hand; otherwise, it is bound to get spread over a large number of terms, causing unwanted distortion in the TF spectrum, as experienced in the case of Fourier transform, STFT, and to some extent, the wavelet transform.

The Empirical Mode Decomposition (EMD) is a recently developed algorithm by N. Huang *et al.* which is specifically designed to address these issues [7]. It expands any given function $f(t)$ into a set of narrowband oscillatory modes, known as intrinsic mode functions (IMFs), which, unlike the basis functions in the Fourier and wavelet transform, are constructed from the input signal $f(t)$ itself. This set of data-driven IMFs is more generic as compared to the Fourier and wavelet basis functions and, due to the nonlinearity of the EMD algorithm, also leads to a compact expansion of the input signal. These IMFs are designed to ensure that the application of the Hilbert transform to the IMFs yields physically meaningful frequency estimates, resulting in more accurate TF representation of the signal [8]. Given that the IMFs are extracted from the input signal, they are expected to carry more useful information in a variety of real world applications.

While the data-driven approach employed by EMD has its advantages in terms of a compact expansion and more accurate TF representation, EMD also inherits its share of flaws for that same reason: It lacks a theoretical foundation and is presently only defined as an output of an iterative 'sifting' algorithm. As a result, the corresponding IMFs lack a formal analytic definition that could be used for their performance evaluation. However, recently, much emphasis is being put to understand the theoretical foundations of various aspects of EMD, including its nonlinear nature, frequency resolution, and the dyadic filter

bank properties.

The standard EMD algorithm by N. Huang *et al.* only deals with univariate time series [7], i.e. a time series having a single data channel. However, several important signal processing areas involve handling simultaneous recordings from multiple sources; for instance, neurophysiological signals [9] [10], wind signals [11] [12] [13], inertial body motion, and finance data [14] [15] [16].

In order to effectively process these signals within the EMD framework, general multivariate extensions of EMD must be developed, which is the main aim of this thesis. The proposed extensions will not only directly process the multivariate signal containing any number of data channels, but are also expected to provide added information regarding the correlation between multiple data channels.

1.2 Thesis Aims

This thesis mainly focuses on EMD, a data-driven technique for adaptively decomposing a signal into its constituent oscillatory modes [7]. EMD considers an input signal at the level of its 'local' oscillations, and does so by directly looking at a signal between its consecutive local extrema; this attribute renders it suitable for describing real world phenomena of nonlinear and nonstationary nature.

The main aim of this thesis is to develop multivariate extensions of EMD to make it possible to be applied to a wide class of multivariate real world signals with an arbitrary number of channels. Depending on the application at hand, the input multivariate signal might constitute simultaneous recordings from the same system (e.g. neurophysiological signals [9]) or signals from different systems (e.g. as used in heterogeneous image fusion [17]).

Next, the properties and the benefits associated with using these multivariate extensions over the standard ones are investigated. More specifically, this thesis studies properties of these extensions in the presence of white Gaussian noise (WGN) and compares their benefits over those obtained from standard EMD. Further, a noise-assisted

EMD algorithm is presented which aims to provide a better decomposition as compared to the standard EMD algorithm.

Finally, the potential applications of the proposed algorithms in the realm of data fusion are illustrated.

1.2.1 Multivariate Extensions of EMD

Recently, multivariate time series analysis has gained immense popularity mainly because of the advances in the sensor and data acquisition technology. As a result, we often come across real world applications involving multiple recordings of signals from a single system: simultaneous recordings of neurophysiological (Electroencephalography (EEG)) signals [9], trivariate wind signals corresponding to horizontal and vertical wind speed [12], multivariate inertial body sensor data [18], and financial time series data [14] [15] [16] are few examples. To this end, an assessment of the correlation between multiple channels of these signals can give a new insight into the signal-generating systems. The univariate algorithms applied to each channel of these multivariate signals separately cannot accomplish this task as they, by design, do not consider correlations between multiple data channels. This calls for the development of multivariate algorithms which can process multiple channels of a signal directly and, hence, can reveal hidden features of the system under consideration.

Given that EMD, due to its local and data-driven nature, has become a viable tool for nonstationary signal processing, its multivariate extensions are a prerequisite for the analysis of a wide range of nonstationary multivariate signals encountered in real world applications. To this end, several complex or bivariate extensions of EMD have been recently proposed, which have already shown potential in various applications [19] [17].

Among these extensions, the most trivial is the complex empirical mode decomposition (CEMD) which cleverly uses the properties of a complex plane to apply standard EMD to two time series, corresponding to the negative and the positive half of the spectrum. Subsequently, the resulting set of IMFs are combined together into a single set of complex-valued IMFs [20]. While CEMD preserves the desired feature of dyadic fil-

ter bank (on the average) for white Gaussian noise (WGN), it fails to produce so-called 'aligned' IMFs, as two separate instances of standard EMD are applied to a set of time series. This results in two disjointed sets of IMFs which are difficult to merge into a single set of complex IMFs.

The other two complex extensions, namely the rotation invariant EMD [21] (RI-EMD) and bivariate EMD (BEMD) [22], are based on similar rationale: they attempt to directly process a bivariate signal by estimating its local mean in two dimensional (2D) space. This results in a set of bivariate IMFs which, unlike complex IMFs from CEMD, have same number of IMFs for both real and imaginary parts, and generally are more 'aligned' in terms of the local oscillations they carry. Due to the above properties, RI-EMD and BEMD have already found applications in data fusion [17] and measuring phase synchronization in EEG signals [19].

In this thesis, the extensions of EMD to process multivariate signals with an arbitrary number of channels are proposed. The rationale behind these extensions is similar to those of RI-EMD and BEMD, i.e. to directly process a multivariate signal by estimating its local mean in higher dimension, where the signal resides. However, these extensions are not trivial since accurate estimation of the local mean in higher domains, a key step in the proposed multivariate extensions of EMD, requires the implementation of uniform sampling schemes in multidimensional spheres. Once the local mean of a multivariate signal is estimated this way, the stopping criteria catering for multivariate IMFs must also be designed to complete the decomposition process.

1.2.2 Properties and Advantages of Multivariate Extensions of EMD

The next aim of this thesis is to study the properties of multivariate extensions of EMD, and the benefits of their use as compared to the standard EMD, applied channel-wise.

The standard (univariate) EMD[2] algorithm, when applied channel-wise on a multivariate signal, produces disjointed sets of IMFs in terms of their oscillatory components, in turn, making it unsuitable for real world applications, such as data fusion [23], phase

[2]In the sequel, term 'standard EMD' will be used to refer to the original univariate EMD algorithm.

synchronisation measurement [24], and classification [25]. In this thesis, the benefits of using multivariate extensions of EMD in such cases are accentuated by showing that they have a tendency to align similar oscillatory modes across the corresponding multivariate IMFs, yielding improved results.

Another important property of multivariate extensions of EMD is their dyadic filter bank structure; like standard EMD, decompositions obtained from multivariate extensions of EMD also act as a dyadic filter bank for WGN inputs, resembling those found in wavelet-based decompositions [26]. The study gives a better understanding of the way the proposed extensions decompose WGN, and can serve to enhance the performance of EMD against the well known mode-mixing problem, whereby, a single IMF contains multiple oscillatory modes and/or a single mode resides in multiple IMFs, compromising their physical meaning.

1.2.3 Applications in Data Fusion

Data fusion involves multiple signals (either from the same source or from different sources) to be combined together in order to achieve improved accuracies and more specific inferences that could not be achieved by the use of only a single signal [27] [28] [29] [30]. It may also refer to the decomposition of a signal into a set of features and the subsequent process of combining only the most informative ones.

At the first glance, EMD may seem a viable candidate in the latter case, since it can adaptively decompose intrinsic data features at a 'local' level; however, it is yet to show any significant potential in the context of data fusion. This is mainly because of a lack of rigorous mathematical treatment regarding the significance of the extracted IMFs, and also due to its undesirable tendency to depend heavily on parameter values and the various methods to estimate these parameters. As a result, different number of IMFs can be extracted from signals with similar statistics causing the problem of non-uniqueness among EMD-based decomposition. The 'correct' estimation of the IMFs, therefore, is currently an active area of research, with several computationally expensive methods like Ensemble EMD (EEMD) and genetic based algorithms being proposed in an attempt to

rectify the problem [31] [32] [33].

In this thesis, the multivariate extensions of EMD will be used to present a more robust framework for data fusion. The problem of non-uniqueness observed in standard EMD, which hindered its application in data fusion, is resolved by making use of the ability of multivariate extensions of EMD to align common oscillatory modes across same-index IMFs.

1.3 Original Contributions

Briefly, the main contributions presented in this thesis include:

1. Developing a trivariate extension of EMD (TEMD) which is capable of processing signals containing three data channels.

2. Extending TEMD to develop a multivariate extension of EMD (MEMD) which can process multivariate signals containing any number of data channels.

3. Demonstrating that MEMD exhibits a dyadic filter bank structure for white Gaussian noise (WGN) inputs.

4. Based on the dyadic filter bank property of MEMD for WGN, developing a noise-assisted MEMD (N-A MEMD) method and showing that it outperforms traditional EMD-based methods in reducing the mode-mixing problem.

5. Showing that the proposed multivariate extensions of EMD achieve mode-alignment in multivariate IMFs, and using this property to develop a robust MEMD-based data fusion framework.

1.4 Thesis Outline

In Chapter 2, a review of the current time-frequency (TF) analysis methods has been presented, with the main emphasis on standard EMD. Moreover, details of the available complex or bivariate extensions of EMD algorithm are also included in this chapter.

In Chapter 3, a trivariate extension of EMD (TEMD) is presented. It is based on the principle of estimating the local mean of a trivariate input signal by taking signal projections in 3D space. It has also been shown that TEMD is not a trivial extension of bivariate extensions of EMD as it aims to find a uniform point set (for set of uniform direction vectors) in 3D space; a point set based on a spherical coordinate system is used in TEMD. Furthermore, the mode-alignment property of TEMD has been validated via simulations on synthetic and real world signals, while its usefulness in TF analysis has been shown on real world wind speed signal. Finally, an experimental study has been included to observe if the IMFs retain the (non)linearity in the original input signal.

Next, in Chapter 4, a multivariate extension of EMD (MEMD) capable of handling any number of data channels, has been proposed. Again, it is not a straightforward extension of TEMD since a trivial extension of the point set used in TEMD has been shown to be suboptimal in higher domains. Therefore, a uniform point set in n-dimensional spaces is proposed for MEMD which is derived from a low-discrepancy Hammerseley sequence; it has been shown to retain its uniformity better as compared to the hyperspherical coordinate system, which is nothing but an extension of spherical coordinate system in an n-dimensional Euclidian space. Like TEMD, MEMD has also been shown to ensure the mode-alignment property on synthetic signals, while simulations on real world inertial motion data have also supported this property.

The main focus of Chapter 5 is on the study of the dyadic filter bank property of the proposed multivariate extensions of EMD. This is of considerable importance since standard EMD has been shown to have similar characteristic in the presence of WGN. It has been shown in this chapter that not only the multivariate extension of EMD obeys similar characteristics for WGN, but it also aligns similar oscillatory modes across the same-indexed IMFs, facilitating its use in data fusion applications.

Furthermore, by using the property of multivariate EMD to behave as a filter bank in the presence of white noise, a noise-assisted multivariate EMD (N-A MEMD) algorithm is given in Chapter 6, whereby by introducing extra channels of multivariate noise, the effects of mode-mixing and mode-misalignment in multivariate IMFs can be reduced.

In Chapter 7, an application of multivariate EMD algorithm has been presented in the context of image fusion. This application makes use of the mode-alignment property of MEMD to achieve better results as compared to conventional techniques.

Finally, in Chapter 8, the conclusions of the thesis have been presented and some directions for future work are also outlined.

Chapter 2

Empirical Mode Decomposition and its Complex Extensions

EMPIRICAL Mode Decomposition (EMD) is a data-driven method designed to decompose any data set into a finite number of oscillatory modes, known as the intrinsic mode functions (IMFs) [7]. The IMFs are zero-mean amplitude-frequency modulated (AM-FM) signals, especially designed to ensure that the application of Hilbert transform, known as Hilbert-Huang transform, yields physically meaningful instantaneous frequency estimates of the input signal [8]. Due to the ability of EMD and the Hilbert-Huang transform to process nonstationary data, it has found a number of different real world applications [34] [35] [24] [36] [13] [11].

2.1 Review of Conventional Time-Frequency (TF) Analysis Techniques

Historically, the prowess and the simplicity of the Fourier spectral analysis had made it one of the most widely used tools for the examination of global amplitude-frequency distributions. However, as evident from its definition given in equation (2.1); where $f(t)$ represents the input signal at hand, and $X(w)$ denotes the Fourier transformed signal; the Fourier analysis provides a global representation of the signal, resulting in a complete loss

of time information, hence, making it unsuitable for nonstationary signal analysis.

$$X(\omega) = \int_{-\infty}^{\infty} f(t) e^{-\imath\omega t}\, dt \tag{2.1}$$

Before presenting a review of the established time-frequency (TF) analysis methods for nonstationary signals, let us revise the definition of stationarity; A time series $f(t)$ is strictly stationary if the joint distributions of

$$\big[f(t_1), f(t_2), \ldots, f(t_n)\big] \text{ and } \big[f(t_1+\tau), f(t_2+\tau), \ldots, f(t_n+\tau)\big] \tag{2.2}$$

are independent of the time difference τ. In most practical cases, however, one is more interested in wide sense stationarity which is limited to the preservation of only first and second order statistics with respect to time:

$$\begin{aligned} E\big(|f(t)|^2\big) &< \infty \\ E\big(f(t)\big) &= m \\ Cov\left(f(t), f(t+\tau)\right) &= Cov(\tau), \end{aligned} \tag{2.3}$$

Here, $E(\cdot)$ and $Cov(\cdot)$ denote the expectation and the covariance operators, respectively.

To incorporate the time information within the Fourier analysis, a short-time Fourier transform (STFT) method was developed by Gabor which obtained the TF distribution by successively sliding a window along the time axis and applying the Fourier transform. Mathematically, the STFT of a time series $f(t)$ can be written as

$$X(\tau, \omega) = \int_{-\infty}^{\infty} w(t-\tau) f(t) e^{-\imath\omega t}\, dt \tag{2.4}$$

where $w(t)$ represents the window function centered at the origin. Since STFT effectively applies the conventional Fourier spectral analysis on each window, data must be linear and stationary within each window (piece-wise stationarity) for the analysis to be valid. This assumption of piece-wise stationarity, however, may not be always valid for real world nonstationary data and even in those cases where it can be imposed, it is hard to make sure

that the window length coincides with the stationary scales, as evident by the constant window length used in STFT. Furthermore, the approach has conflicting requirements regarding the window size, resulting in a compromise between the localization in time and frequency domain.

In wavelet analysis, the window length can be adjusted according to the temporal scales being observed and can thus be seen as an adjustable window Fourier transform analysis [37]. However, unlike the Fourier transform which only uses sines and cosines as basis functions, wavelet analysis adopts a broad class of signals as its basis functions, $\psi(t)$, which satisfy very general conditions[1] [38]. Mathematically, the continuous wavelet transform of a signal $f(t)$ can be given by:

$$W(a,b;f,\psi) = a^{-\frac{1}{2}} \int_{-\infty}^{\infty} f(t)\psi^* \left(\frac{t-b}{a}\right) dt \tag{2.5}$$

in which a is the dilation factor, also known as the scale factor, and b denotes the translation from the origin and $(\cdot)^*$ represents the operation of complex conjugate.

Though the wavelet transform has become very popular over the past two decades, it still uses predefined basis functions on to which the input signal is linearly projected, and hence yields a less compact and less meaningful decomposition, especially for 'non-harmonic' signals [39].

Another established method for TF analysis of nonstationary signals is known as the Wigner-Ville distribution, which uses the Fourier transform of central covariance function to give the following distribution:

$$V(\omega,t) = \int_{-\infty}^{\infty} f\left(t-\frac{\tau}{2}\right) f\left(t+\frac{\tau}{2}\right) e^{-\imath\omega t}\, dt \tag{2.6}$$

where $f(t)$ represents the input signal to be transformed. A major drawback of the approach is that it suffers from the interference between signal components, which causes spurious artifacts in the spectrogram [4].

[1] Function $\psi(t)$ is normally taken as a zero average function, centered around zero and with finite energy.

2.2 The Concept of Instantaneous Frequency

In the previous section, some established algorithms for time-frequency (TF) analysis of nonstationary data were briefly reviewed. In order to define a local frequency estimate [40], which is an essential requirement for nonstationary data analysis, the above methods projected the input signal on some fixed basis functions of certain frequency.

Another class of methods for nonstationary signal analysis define the local frequency estimates based on the Hilbert transform [7]; they perform highly localised analysis, unlike the projection-based schemes, such as STFT and wavelet analysis, which require at least one full oscillation to define the local frequency value. For an input signal $x(t)$, its Hilbert transform is given by:

$$y(t) = \frac{1}{\pi} P \int_{-\infty}^{\infty} \frac{x(t')}{t - t'}\, dt \tag{2.7}$$

where $x(t)$ and $y(t)$ represent the input and the output signals respectively, and P denotes the principal Cauchy value. Using this definition, $x(t)$ and $y(t)$ form a complex conjugate pair and can be combined to form an analytic signal, $z(t)$, defined as:

$$z(t) = x(t) + \imath y(t) = a(t) e^{\imath \theta(t)}, \tag{2.8}$$

where

$$a(t) = \left[x^2(t) + y^2(t)\right]^{\frac{1}{2}} \text{ and } \theta(t) = \tan^{-1} \frac{y(t)}{x(t)}. \tag{2.9}$$

Essentially $y(t)$, as given in equation (2.7), is the convolution of $x(t)$ with $\frac{1}{t}$, highlighting the local properties of $x(t)$. Using equation (2.8), a local estimate of the instantaneous frequency can be defined as

$$\omega(t) = \frac{d\theta(t)}{dt} \tag{2.10}$$

However, for instantaneous frequency given in equation (2.10) to be meaningful, some limitations must be imposed on the data; since, the instantaneous frequency ω can only take a single value at a time, it can only represent one component (narrowband) signals.

The standard bandwidth measure, denoted as ν, can be defined in terms of the ith

moment (m_i) of the spectrum as follows [41] [42] [43]:

$$N_1^2 - N_0^2 = \frac{\nu}{\pi^2} = \frac{1}{\pi^2}\frac{m_4 m_0 - m_2^2}{m_2 m_0} \tag{2.11}$$

where N_0 and N_1 denote the number of zero crossings and extrema per unit time, respectively. Hence, for a narrow-band signal $\nu = 0$, the number of zero crossings and the number of extrema should be approximately equal.

It has also been argued in [44] [45] [7] that real part of the Fourier transform of a signal must have only positive frequencies for the local frequency estimate to be physically meaningful. Furthermore, simple examples have been given in [7] to illustrate these restrictions locally, and shown that, for such signals, instantaneous frequency estimates can only be defined accurately if the function is restricted to have a zero local mean. This local restriction, along with the global restrictions given in equation (2.11), leads to defining a class of functions, designated as intrinsic mode functions (IMFs), for whom the instantaneous frequency can be defined everywhere. EMD aims to decompose input data as a summation of these 'local' IMFs via an iterative procedure, known as the sifting algorithm. The properties of IMFs are listed in the next section.

2.3 Intrinsic Mode Functions

Intrinsic mode functions (IMFs) belong to a class of functions designed to conform to the global and local conditions which are necessary to yield accurate and meaningful instantaneous frequency estimates, obtained via Hilbert transform [46]. Formally, these functions must satisfy the following two conditions:

1. The upper and lower envelope are symmetric: at every point the mean value of the upper and lower envelope should be zero;

2. The number of zero crossings and the number of extrema are equal or they differ at most by one.

2.4 Empirical Mode Decomposition

Empirical mode decomposition is a data-driven technique to decompose a signal, by means of an iterative process called the sifting algorithm, into a finite set of oscillatory components called intrinsic mode functions (IMFs), which represent the temporal modes (scales) present in the data [7]. Given an arbitrary time series $x(k)$, EMD decomposes it into a sum of IMFs $\{c_m(k)\},\ m = 1, \ldots, M$ and the residual $r(k)$, that is

$$x(k) = \sum_{m=1}^{M} c_m(k) + r(k) \tag{2.12}$$

The residual $r(k)$, unlike $\{c_m(k)\}_{m=1}^{M}$, does not contain any oscillations and its physical meaning is a trend within the signal.

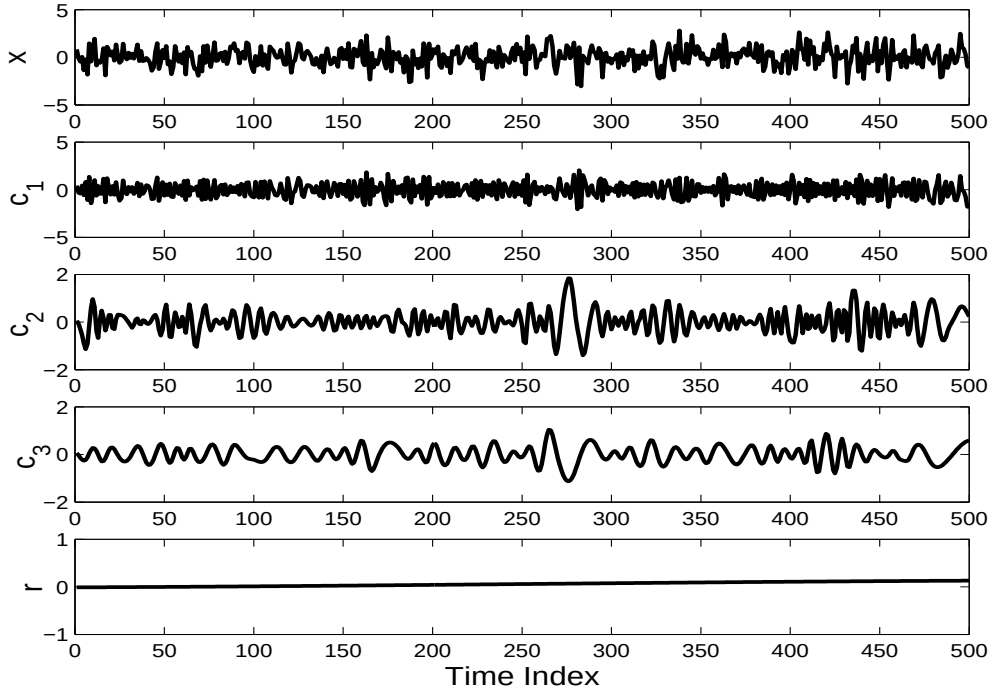

Figure 2.1: An example of the EMD sifting operation applied to white Gaussian noise (x in the top panel) for which seven IMFs (only first three are shown) and a trend were obtained.

Algorithm 1 The sifting algorithm for univariate EMD

1: Find the locations of all the extrema of $x(k)$

2: Interpolate (using spline interpolation) between all the minima (resp. maxima) to obtain the signal envelope passing through the minima, $e_{min}(k)$ (resp. $e_{max}(k)$)

3: Compute the local mean $m(k) = \big(e_{min}(k) + e_{max}(k)\big)/2$

4: Subtract the mean from the signal to obtain the 'oscillating' signal $d(k) = x(k) - m(k)$

5: If the resulting signal $d(k)$ obeys the stopping criterion, it becomes the first IMF, otherwise set $x(k) = d(k)$ and repeat the process from Step 1 until the first IMF is obtained.

2.4.1 Sifting Algorithm

The IMFs are extracted from an input signal $x(k)$ by means of an iterative algorithm called the sifting algorithm, described in Algorithm 1. The listed algorithm only describes the method to extract the first IMF ($d_1(k)$) from the input signal $x(k)$, and the same iterative process is applied again on the local trend, $x(k) - d_1(k)$, to obtain the second IMF and so on. The process is repeated until all oscillatory modes in the input signal are extracted in the form of IMFs and we are left with a monotonic function, which can be characterized by lack of enough extrema to form an oscillation. At the end of the sifting operation, a data-driven decomposition of the input signal in the form of equation (2.12) is obtained. An example decomposition is shown in Figure 2.1, where EMD was applied to a realisation of white Gaussian noise (denoted by x in the top panel) which gave seven IMFs ($c_1, \ldots, c_7$) and a trend (r).

As is evident in the Algorithm 1, an important step in the sifting process is to estimate the local mean of the input signal via upper and lower envelopes. These envelopes are in turn obtained by locating all the extrema (both maxima and minima) of the input signal. The maxima of the input signal are then interpolated to yield an upper envelope and, similarly, the minima are connected to obtain the lower envelope of the signal; this process is shown graphically in Figure 2.2. Though, any interpolation method can be used in the sifting process, cubic spline interpolation scheme is widely used in practice [47].

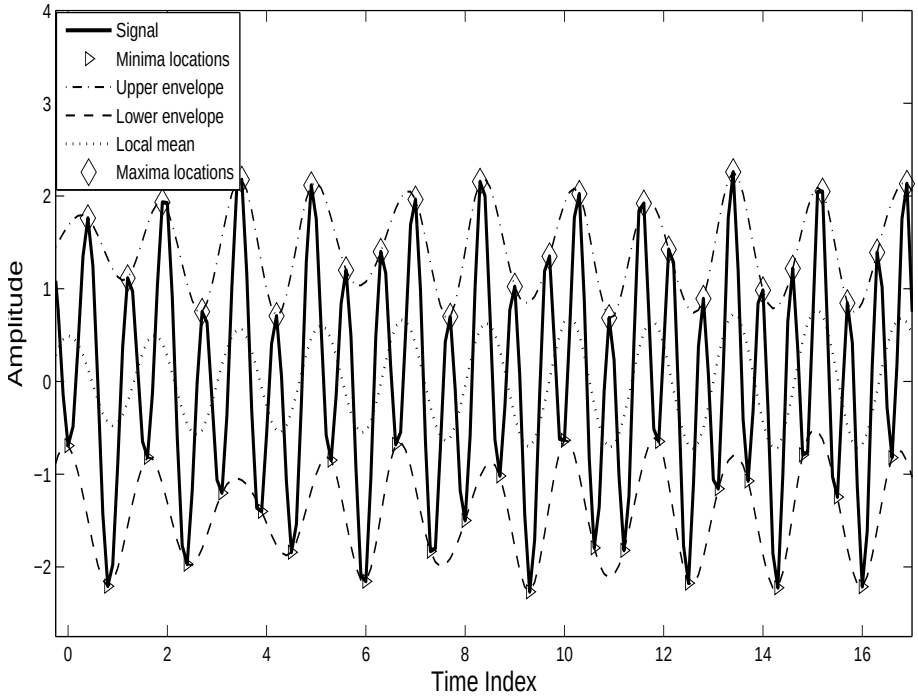

Figure 2.2: Local mean estimation during sifting process in EMD. Upper envelope and lower envelope (dashed lines) of the input signal (solid line) are averaged to obtain the local mean signal (dotted line).

However, selecting extrema of the input signal as interpolation points and employing cubic splines for their interpolation is not the only available method for envelope estimation. In [48], a method is given for the optimization of both the interpolation points and the piece-wise interpolating polynomials for the estimation of the upper and lower envelopes of the signal. For a set of well-defined multicomponent signals, the method performed optimization of the EMD free parameters within a genetic algorithm framework and yielded improved results as compared to the standard approach involving extrema points and cubic spline interpolation [49].

Next, the upper and the lower envelopes are averaged to obtain the local mean of an input signal, as shown in Figure 2.2. The local mean is then subtracted from the input signal to yield the 'local detail'. As described earlier, the sifting process is iteratively applied on a 'local detail' until it fulfils the requirement for an IMF.

2.4.2 Stopping Criteria in EMD Sifting Process

The stopping criterion in the sifting process of EMD is used to check whether the 'local trend' $d(k)$, obtained in Step 5 of the Algorithm 1, fulfills the IMF criteria. The choice of a suitable stopping criterion is important as if the data is over-sifted, it will result in over-decomposition of IMFs with uniform amplitude modulations, whereas, under-sifted IMFs will not satisfy mono-component criteria and the estimate of instantaneous frequency will be erratic. The sifting criterion also determines the compactness of EMD-based decomposition: A strict criterion results in more sifting iterations of the algorithm and hence the greater number of IMFs, whereas a weak criterion gives comparatively less number of IMFs. The following are some of the most commonly used stopping criteria used in EMD:

The stoppage criterion proposed by Huang in [7] uses the normalized squared difference between two successive sifting iterates $d_n(k)$ and $d_{n-1}(k)$, that is

$$\sum_{k=0}^{K} \frac{\|d_{n-1}(k) - d_n(k)\|^2}{d_{n-1}^2(k)} \leq SD \tag{2.13}$$

where K represents the total number of samples in the original series $x(k)$, and the empirical value of SD is usually set within the range (0.2-0.3). A low value of SD, that is, sifting to the extreme, would remove all the amplitude modulation from the signal which would result in purely frequency modulated components. This is not desired as IMFs in that case will not have a physical meaning. The downside of this criterion is that it does not depend on the actual definition of IMF, and may underperform in practice.

A more robust criterion, based on the original definition of IMF, stops the sifting process only after the condition of an IMF is met for S consecutive times [46]; the condition checked for an IMF is that the difference between the number of extrema and zero crossings should not exceed by more than one. It has also been shown in [46] that the empirical range of S should be chosen between 4 and 8.

In [50], another stopping criterion is presented, which defines the envelope amplitude, $a(k)$, as

$$a(k) = \frac{e_{max}(k) - e_{min}(k)}{2} \tag{2.14}$$

Next, the evaluation function is defined based on the envelope amplitude and the local mean of the data, as

$$f(k) = \left| \frac{m(k)}{a(k)} \right| \tag{2.15}$$

where $m(k) = \frac{e_{max}(k)+e_{min}(k)}{2}$ is the local mean signal. The sifting process is continued till the value of the evaluation function, $f(k)$, is greater than or equal to some predefined thresholds; Sifting is performed until $f(k) < \theta_1$ for some preselected fraction $(1 - \alpha)$ of the total duration, while $f(k) < \theta_2$ for the remaining fraction. In this way, the stopping criterion ensures globally small fluctuations in local mean while taking into account the overall large excursions in the input signal.

In [50], the values of the three parameters recommended were $[\theta_1 = 0.05,\ \theta_2 = 0.5,\ \alpha = 0.05]$. The criterion involving the equality of the number of extrema and zero crossings of a signal can also be used in combination with equation (2.15) to yield a robust stopping criterion. For all the simulations involving univariate signals in this thesis, this composite criterion has been used with parameter values taken as $[\theta_1 = 0.05,\ \theta_2 = 0.5,\ \alpha = 0.05]$ and $S = 1$, unless stated otherwise.[2]

2.5 The Hilbert-Huang Spectrum

After obtaining the IMFs using the EMD method, the Hilbert transform can be applied to each IMF separately and the instantaneous frequency can be computed according to equation (2.10). Given a signal $x(k)$ and its corresponding IMFs $\{c_m(k)\}_{m=1}^{M}$, application of the Hilbert transform to the decomposition given in equation (2.12) yields

$$x(k) = \sum_{m=1}^{M} a_m(k) e^{\imath\theta_m(k)} = \sum_{m=1}^{M} a_m(k) e^{\imath \int w_m(k)dt} \tag{2.16}$$

The residual r is left purposely as it is either a monotonic function or a constant. Note that equation (2.16) yields a variable amplitude $a_m(k)$ and instantaneous frequency $w_m(k)$, making the corresponding expansion suitable for processing nonstationary data. The

[2]For simulations involving multivariate signals, a multichannel variant of this criterion, formally presented in Chapter 4, has been used as a stopping criterion.

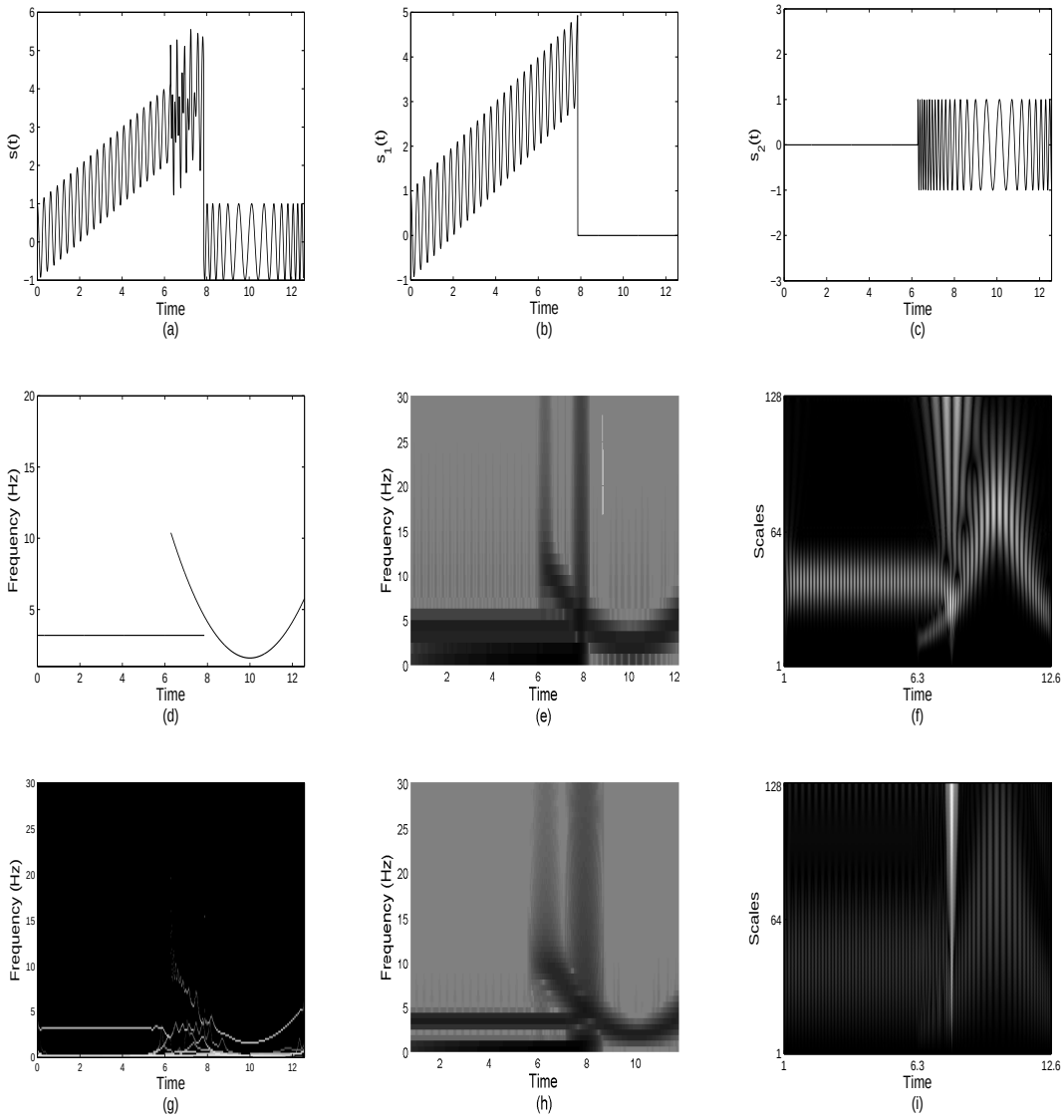

Figure 2.3: Comparing the Hilbert-Huang spectrum with established linear time-frequency methods on a carefully chosen synthetic signal $s(t)$. (a, b, c) The signal $s(t) = s_1(t) + s_2(t)$ and its two components $s_1(t)$ and $s_2(t)$. (d) The instantaneous frequency of $s_1(t)$ and $s_2(t)$. (e, h) Two examples of short-time Fourier transform (STFT) with a narrow window (128) (e) and wide window (256) (h). (f, i) Two examples of a scalogram generated via continuous Wavelet transform (CWT) with Morlet wavelet (f) and Haar wavelet (i). (g) The Hilbert-Huang spectrum generated by applying EMD to $s(t)$. A comparison between the Hilbert-Huang transform and other linear TF analysis methods demonstrates the superiority of EMD due to its data-driven nature; the Hilbert-Huang spectrum clearly gives a 'crisp' TF representation of $s(t)$ than its spectrogram (STFT) and scalogram (wavelet transform). The presence of 'extra' low frequency component in the spectrum is due to the fact that $s(t)$ is not a zero mean signal.

amplitude $a_m(k)$ and instantaneous frequency $w_m(k)$ can be plotted versus time index k to yield a time-frequency-amplitude representation of the entire signal known as the Hilbert-Huang spectrum, $H(k, w)$.

To demonstrate the power of the Hilbert-Huang spectrum as a signal analysis tool, its results are compared with other established linear time-frequency representations, including the STFT and the wavelet transform. The synthetic signal chosen for this analysis was used in [51] for similar purposes; The signal $s(t) = s_1(t) + s_2(t)$ consists of two frequency components $s_1(t) = 0.5t + \cos 20t$ for $0 \leq t \leq \frac{5\pi}{2}$, and $s_2(t) = \cos\left(\frac{4}{3}[(t-10)^3 - (2\pi - 10)^3] + 10(t - 2\pi)\right)$ for $2\pi \leq t \leq 4\pi$, as shown in the top row of Figure 2.3. The instantaneous frequency for the two components are also shown in Figure 2.3(d) and are given by: $f_1(t) = \frac{20}{2\pi}$ for $s_1(t)$, and $f_2(t) = 4(t-10)^2 + 10$ for $s_2(t)$.

Next, the spectrogram and scalogram, obtained by applying the STFT and the continuous wavelet transform to $s(t)$ are plotted in the middle and the right columns of Figure 2.3, respectively. More precisely, Figures 2.3(e, h) show the spectrograms corresponding to the narrow window (128) and the wide window (256), whereas Figures 2.3 (f, i) show the scalograms obtained by applying the continuous Wavelet transform (CWT) to $s(t)$ using the Morlet and the Haar wavelets, respectively. It can be noticed that while the instantaneous frequency profile is recognizable in the case of these linear TF analysis methods, it is significantly blurred in each case depending on the choice of basis functions (transform method) and other parameters, e.g. window length in STFT, and type of wavelet function in CWT. On the other hand, the Hilbert-Huang spectrum of $s(t)$, plotted in Figure 2.3(h), clearly shows better resolution properties than the STFT and the wavelet analysis.

2.6 EMD Properties and Applications

Due to the empirical nature and the lack of solid mathematical foundation in EMD, most of the work in understanding its properties is based on performing extensive numerical

simulations in controlled situations. As a result, the performance evaluation of EMD as compared to other existing methods is hard to achieve. However, despite the above flaws, the empirical and data-driven nature of EMD makes it a viable tool in many real world scenarios, where the convenience of choosing an a priori fixed set of basis functions and their orthogonality are less significant than the compactness and the physically meaningful nature of the expansion. In this section, some of the important developments regarding the theory and properties of EMD algorithm will be presented.

The nature of the sifting process in EMD algorithm ensures the *completeness* of EMD algorithm, since equation (2.12) is an identity. Completeness is an important property for mathematical tractability of a decomposition.

The *orthogonality* of EMD output (IMFs) was studied in [7] and it was found that it was satisfied in practical sense but could not be guaranteed theoretically [7]. This is due to the approximations involved in the calculation of local mean of a signal through envelopes. Therefore, while the following equation[3]

$$E\{(x(k) - E\{x(k)\})E\{x(k)\}\} = 0 \tag{2.17}$$

holds 'locally' in practice by virtue of the EMD decomposition, it is not strictly applicable due to the fact that the local mean calculated here is only an approximation. As a result, leakage is unavoidable, but is negligible in most practical cases, as demonstrated in [7] via numerical simulations on real world wind speed data using the so called orthogonality index.

A study of the characteristics of white Gaussian noise (WGN) using EMD was carried out in [26] and [52], and it was found that EMD effectively acts as a dyadic filter bank similar to those found in the wavelet-based decompositions. The Fourier spectra of the IMF components were found to be 'self-similar' in a sense that they had similar shape and covered the same area (had same energy) on semi-logarithmic time scale.

Based on the above results on statistical characteristics of WGN, Wu and Huang

[3]The equation can be interpreted as an inner product of the first and second IMFs obtained from $x(k)$ given that only a single sifting iteration on $x(k)$ yielded the 'true' local mean and the hence the second IMF $E\{x(k)\}$.

proposed a denoising (detrending)[4] method by assigning 'statistical significance' to each IMF, extracted from an input noisy data, based on the a priori knowledge of IMF statistics in the case of WGN. The resulting denoising (detrending) method rejects (keeps) those IMFs whose energies are found to be similar to the ones obtained from the decomposition of reference WGN. A generalization of this method has been proposed in [53] to denoise a wider class of signals which are corrupted by fractional Gaussian noise (with known Hurst exponent, H). Moreover, recently, a number of EMD-based denoising techniques inspired from standard wavelet thresholding and translation invariant thresholding have also been developed, yielding improved results [54].

Though EMD fulfills the mathematical uniqueness property resulting in a unique set of IMFs for a given input data and a set of EMD parameters, it sometimes fails to observe 'physical uniqueness' due to its empirical nature and sensitivity to algorithm parameters [55]; this problem of EMD will be further highlighted in detail, via examples, in section 2.6.1. To alleviate this problem, an ensemble empirical mode decomposition (EEMD) method was proposed in [31] which adds multiple realizations of white noise, say $\{w_n(k)\}_{n=1}^{N}$, to the input signal, $x(k)$, resulting in the following set of multiple observations:

$$x_n(k)\}_{n=1}^{N} = x(k) + w_n(k)\}_{n=1}^{N} \tag{2.18}$$

The resulting data set, $x_n(k)$ is then decomposed via multiple applications of EMD algorithm to yield N sets of IMFs, which are averaged together to yield a single set of 'true' IMFs. As evident, the EEMD method is computationally expensive and its improved version in terms of computational requirements has been recently proposed in [56]. Another issue with EEMD is its reconstruction error due to the added WGN [31]; a new method avoiding this problem will be presented in Chapter 6. The main aim of such noise-aided EMD analysis is to establish a dyadic reference frame in time-frequency (TF) space, and owing to the filter bank property of EMD, this enables a more natural separation of the IMFs.

Since EMD was initially designed to offer improved TF analysis via its accurate in-

[4]Denoising refers to removing the modes identified as noise, whereas, detrending aims to keep them.

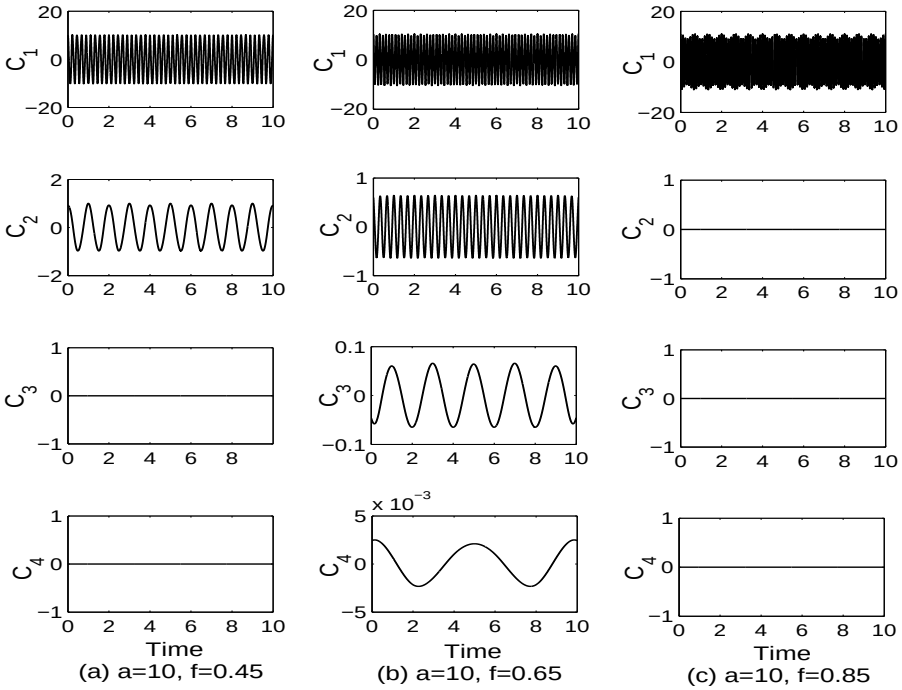

Figure 2.4: Two tone signal decomposition using EMD: (a) IMFs of the two tone signal corresponding to $a = 10$ and $f = 0.45$ in equation (2.19). EMD correctly decomposed two tones as separate IMFs. (b) IMFs of the two tone signal corresponding to $a = 10$ and $f = 0.65$; EMD created new frequency components in C_3 and C_4 which were not present in the input signal. (c) IMFs of the two tone signal corresponding to $a = 10$ and $f = 0.85$; EMD considered input signal as a single component.

stantaneous frequency estimates, several studies have focussed on its ability to distinguish neighboring frequency components [57] [58]. In [57], for instance, the behavior of EMD algorithm in the case of the following simplified two-tones model was studied:

$$x(t; a, f) = \cos 2\pi t + a\cos(2\pi f t + \phi), \tag{2.19}$$

where a and $f \in]0, 1[$ refer to the amplitude and frequency ratio respectively; therefore, the term $\cos 2\pi t$ effectively becomes the high frequency component and $\cos(2\pi f t + \phi)$ can be considered as low frequency component, by design.

It was shown in [57] that, depending on the value of relative amplitude a and frequency f in the above model equation (2.19), EMD answered the basic question of

two tone separation problem by revealing the following three scenarios: (1) when two individual tones were correctly separated, (2) when the input signal was seen as a single component, and (3) when something else was done by EMD. Though, the results mostly followed intuition, for instance, it was found that EMD only resolved two frequencies when f was below some threshold; it was also observed that the cutoff frequency depended on the amplitude ratio in a non-symmetric way, owing to nonlinear nature of the EMD algorithm.

The performance of the EMD algorithm was next analysed by exploring the three scenarios mentioned in the previous paragraph, by using a well defined set of two tone input signals. The set of signals was chosen such that each signal in the set corresponded to one of the three conditions mentioned above. For that cause, the value of amplitude parameter a was set to $a = 10$, whereas the frequency ratio was set to $f = 0.45$, $f = 0.65$ and $f = 0.85$ to obtain the three signals used in the analysis. The resulting signals were then decomposed using the EMD algorithm and the IMFs in each case are shown in Figure 2.4. It can be seen that for $f = 0.45$ (Figure 2.4(a)), EMD correctly decomposed the input signal to two input tones, whereas for $f = 0.85$ (Figure 2.4(c)) EMD considered the signal as a single component. For the signal corresponding to $f = 0.65$ (Figure 2.4(b)), however, the behaviour of EMD was not intuitive as it created new lower frequency components (IMF3 and IMF4) which were not present in the original signal. This example highlights a specific scenario where EMD failed to provide the correct answer as the new frequency components could be wrongly interpreted as intrinsic mode of the signal when its physical relevance is doubtful.

While studying the spectral resolution of EMD, it must be kept in mind that EMD doesn't always aim to separate closely spaced frequency components but, in effect, its goal is to extract physically meaningful components in accordance with the definition of IMF. Having said that, the separation of closely spaced components via EMD may be important in certain cases, and in [58], the addition of a masking signal (a high frequency component) has been proposed for this cause. However, this method needs some a priori information about input data to choose the appropriate frequency for the masking signal, thus, compromising the data-driven nature of EMD algorithm.

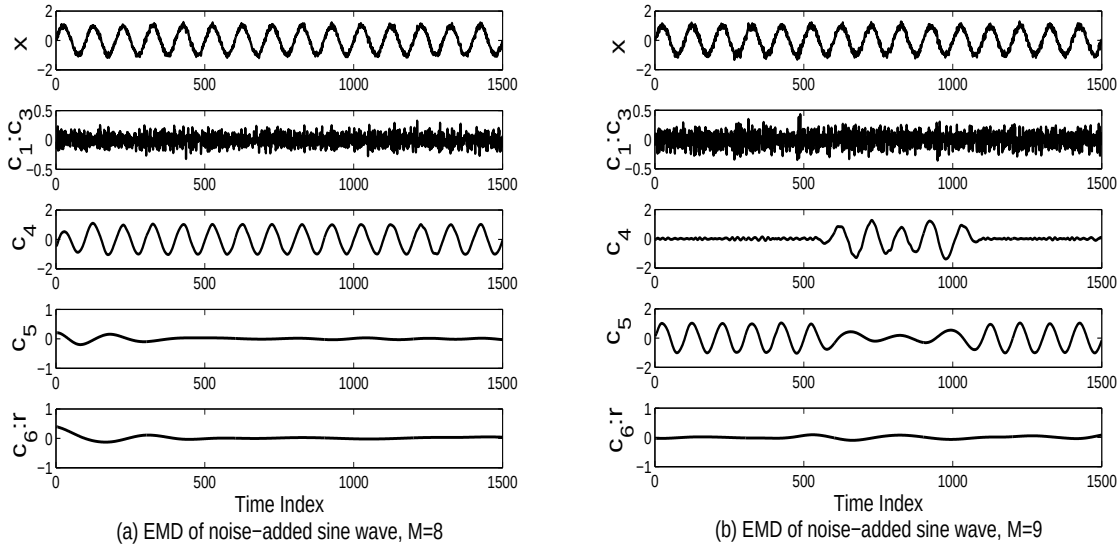

Figure 2.5: Non-uniqueness of EMD: Decomposition of a sinusoid corrupted by two different realizations of white Gaussian noise, obtained by EMD. Different number of intrinsic mode functions, $M = 8$ in (a) and $M = 9$ in (b) are obtained. Moreover, the original sinusoid is located in different modes: c_4 in (a) and $c_4 + c_5$ in (b), highlighting the non-uniqueness of decomposition.

Recently, Daubechies *et al.* have proposed a method which yields IMF-like components by using a combination of wavelet transform and reallocation method [51]. Specifically, they first give a precise definition of the class of these IMF-like functions and then show that their method can decompose arbitrary functions within that class. The resulting synchrosqueezed wavelet transform method is expected to overcome the difficulties in EMD which makes it hard to analyse mathematically. This method is still in infancy though and requires further studies regarding its properties and scope of application.

In addition, a method has been proposed recently for the optimization of the interpolation points and the interpolating polynomials in order to estimate the upper and the lower envelopes of an input signal. The method adopts genetic algorithm framework to perform the optimization of the EMD free parameters [48] [49].

2.6.1 Non-uniqueness in EMD-based Decomposition

The data-driven nature of EMD, though having its clear advantages, also compromises the uniqueness of EMD-based decomposition. As a result, signals with similar statistics

may yield different decompositions, both in terms of the number and the properties of resulting IMFs. This problem is mainly caused due to the mode-mixing, whereby a single IMF contains multiple oscillatory modes and/or a single mode resides in multiple IMFs, compromising the physical and practical meaning of IMFs in certain cases [17] [31].

To illustrate the (non-)uniqueness of EMD, a sinusoid X of unit amplitude and frequency was corrupted by two different realisations, $W1$ and $W2$, of a white Gaussian noise signal with the same statistical properties (zero mean and standard deviation of 0.2). The EMD algorithm was subsequently applied to them. The IMFs extracted from both cases are shown in Figure 2.5; in Figure 2.5(a), which shows the decomposition of the first signal (corrupted by $W1$), the original sinusoid corresponds to the fourth IMF c_4, whereas the noise is contained within the IMFs $c_1 - c_3$. Figure 2.5(b) shows the decomposition of a sinusoid corrupted by W2; here, in addition to having different number of IMFs, ($M = 9$), as compared to the first case, ($M = 8$), mode-mixing also occurred across c_4 and c_5, as the signal of interest (sinusoid) is present in both these IMFs .

Though, the issue of mode-mixing can be addressed by performing EMD over a number of independent realizations of WGN (Ensemble EMD [31]), it is computationally very expensive. Other studies in this regard include combining EMD with adaptive learning algorithms based on temporal neural networks to make it robust to its parameter selection (stopping criterion, envelope interpolation) and against the mode-mixing and the non-uniqueness problems [59]. In [17] [60], the problem of mode-mixing is addressed, in the context of fusion applications using the complex extensions of EMD.

2.7 Complex Extensions of EMD

This section focuses on the extensions of EMD capable of handling bivariate or complex data. These extensions are a prerequisite to cater for a large class of real world complex signals. Applying EMD separately on two channels of a complex signal is suboptimal, as it does not consider correlations among channels; complex extensions of EMD, on the other hand, process complex signals directly, and take into account interchannel correlations.

The main challenge in the complex extensions of EMD is to estimate the local mean of a complex signal as it is hard to define local extrema of a complex signal directly. Among existing complex extensions of EMD, complex EMD (CEMD) [20] makes use of the analyticity of the signal to apply standard EMD [7] component-wise, whereas rotation invariant EMD (RI-EMD) [21] and bivariate EMD (BEMD) [22] estimate the local mean based on the envelopes obtained by taking projections of the input signal in different directions.

2.7.1 Complex EMD

For bivariate signals, complex EMD (CEMD) [20] uses the positive and negative frequency components to apply standard EMD to two univariate time series. This is achieved by converting a general non-analytic signal into two analytic signals, each corresponding to either the positive or the negative frequency components of the original signal. The standard EMD is then applied to the real part of the resulting analytic signals to obtain two sets of IMFs. These sets are then combined to form complex-valued IMFs.

More precisely, let $x(k)$ be a complex-valued sequence and $X(e^{\imath w})$ its Discrete Fourier Transform (DFT). By processing signal $x(k)$ with the filter having a transfer function

$$H(e^{\imath w}) = \begin{cases} 1, & 0 < \omega \leq \pi \\ 0, & -\pi < \omega \leq 0 \end{cases} \tag{2.20}$$

the DFT of two analytic signals, denoted by $X_+(e^{\imath w})$ and $X_-(e^{\imath w})$, are generated, which correspond respectively to the positive and the negative frequency parts of $X(e^{\imath w})$. The subsequent application of the Inverse Fourier Transform, denoted by $\mathcal{F}^{-1}(\cdot)$, to $X_+(e^{\imath w})$ and $X_-(e^{\imath w})$ yields time series $x_+(k)$ and $x_-(k)$, defined as

$$x_+(k) = \mathcal{R}\big[\mathcal{F}^{-1}[X_+(e^{\imath w})]\big] \tag{2.21}$$

$$x_-(k) = \mathcal{R}\big[\mathcal{F}^{-1}[X_-(e^{\imath w})]\big] \tag{2.22}$$

where the operator $\mathcal{R}(\cdot)$ extracts the real component of a complex signal. Standard univariate EMD can then be applied to $x_+(k)$ and $x_-(k)$, to give

$$x_+(k) = \sum_{m=1}^{M^+} c_m(k) + r_+(k) \tag{2.23}$$

$$x_-(k) = \sum_{m=-1}^{-M^-} c_m(k) + r_-(k) \tag{2.24}$$

where symbols M^+ and M^- denote, respectively, the number of IMFs for the positive and the negative frequency parts, $c_m(k)$ are the IMFs, and $r_+(k)$ and $r_-(k)$ are residual signals for $x_+(k)$ and $x_-(k)$. The original complex signal $x(k)$ can then be reconstructed in terms of $x_+(k)$ and $x_-(k)$ as

$$x(k) = (x_+(k) + \imath\mathcal{H}[x_+(k)]) + (x_-(k) + \imath\mathcal{H}[x_-(k)])^*, \tag{2.25}$$

where $\mathcal{H}(\cdot)$ is the Hilbert transform operator and the symbol $(\cdot)^*$ denotes the complex conjugation operator.

For the mth complex IMF $y_m(k)$, defined as

$$y_m(k) = \begin{cases} c_m(k) + \imath\mathcal{H}\big[c_m(k)\big], & m = 1, \ldots, M^+, \\ \big(c_m(k) + \imath\mathcal{H}\big[c_m(k)\big]\big)^*, & m = -M^-, \ldots, -1 \end{cases} \tag{2.26}$$

the original complex valued signal $x(k)$ can also be written as

$$x(k) = \sum_{m=-M^-, m\neq 0}^{m=M^+} y_m(k) + r(k), \tag{2.27}$$

where $r(k)$ represents the trend in the data, and is represented in terms of the residuals of x_n^+ and x_n^- as

$$r(k) = \big(r_+(k) + r_-(k)\big) + \imath\mathcal{H}\big(r_+(k) - r_-(k)\big), \tag{2.28}$$

The so defined CEMD retains the generic structure of standard EMD; however, as the number of IMFs for $x_+(k)$ and $x_-(k)$ can in general be different, it is difficult to

interpret the physical meaning of the extracted IMFs. Moreover, this approach is also not suitable for extension to higher dimensions.

2.7.2 Rotation-Invariant EMD

The main difficulty with the CEMD arises because it does not operate directly in $\mathbb{C}$. The Rotation-Invariant EMD (RI-EMD) algorithm [21] operates directly in $\mathbb{C}$, and defines the extrema of a complex signal as points where the angle of the first derivative of the signal becomes zero. For a complex signal, $z(t) = x(t) + \imath y(t)$, it can be shown that this criterion is equivalent to $y'(t) = 0$, that is, the extrema of the imaginary part. Mathematically, for a complex signal $z(t) = x(t) + \imath y(t)$, the extrema locations are at

$$\begin{aligned} \angle z'(t) = 0 &\Rightarrow \angle\{x'(t) + \imath y'(t)\} \\ \tan^{-1}\frac{y'(t)}{x'(t)} = 0 &\Rightarrow y'(t) = 0. \end{aligned} \tag{2.29}$$

As it is assumed that a local maximum is followed by a minimum, these sets can be interchanged. The spline interpolation is then performed on both components separately to obtain complex-valued envelopes, which are averaged to obtain the local mean. This method yields a single set of complex-valued IMFs, and the ambiguity at the zero frequency within the CEMD is avoided due to the direct operation in $\mathbb{C}$. However, since this method uses the extrema of only the imaginary component of a bivariate signal to calculate the local mean, its accuracy is compromised.

The RI-EMD gives a set of complex IMFs in which the common frequency modes are properly aligned. The complex IMFs thus obtained have meaningful physical relevance; this is demonstrated on the a set of wind[5] speed and direction measurements, which have been made complex by convenience of representation. Figure 2.6(a) shows the polar plot of the original wind signal, whereas Figure 2.6(b) shows the contribution of the sixth and seventh IMF ($c_6 + c_7$). It is clear that the complex IMFs have physical meaning as they can reveal the dynamics of the original signal at different scales.

[5]Publicly available from http://mesonet.agron.iastate.edu/request/awos/1min.php

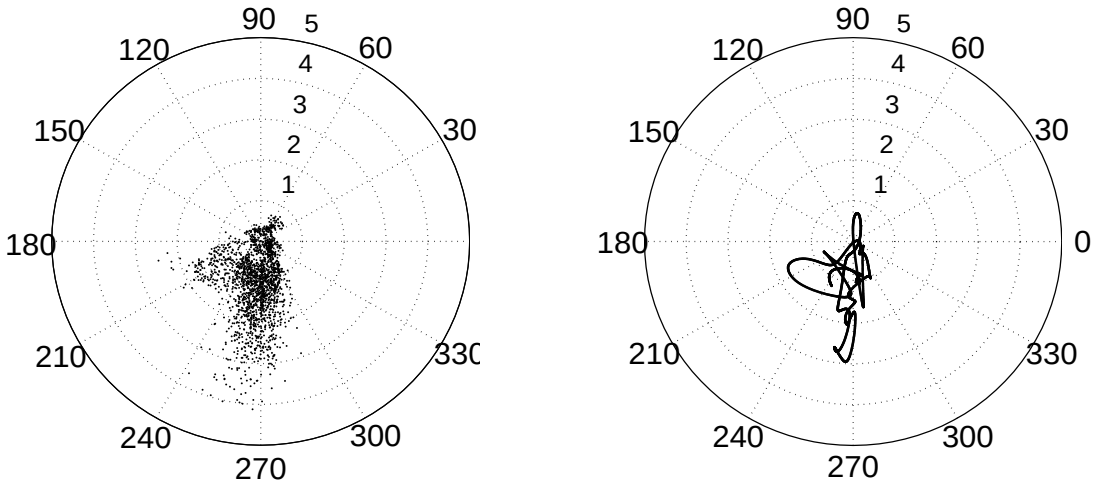

(a) Polar plot of the input wind signal

(b) Sum of sixth and seventh complex IMF

Figure 2.6: A complex wind signal analysed by the Rotation-Invariant EMD algorithm.

2.7.3 Bivariate EMD

The bivariate EMD algorithm [22] calculates the local mean envelopes based on the extrema of both (real and imaginary) components of a complex signal, yielding more accurate estimates than RI-EMD.

It proceeds by projecting an input bivariate signal in V different directions, with each direction vector defined based on equidistant points along the unit circle. Next, the corresponding envelopes for each direction are obtained by interpolating the extrema of projected signals via component-wise spline interpolation; these envelopes are then averaged to obtain the local mean. The larger the number of directions employed in BEMD, i.e. larger the value of V, the more accurate the estimate of the envelope. Assuming four directions, the center of envelopes at a point in space is given by either of the following methods:

1. The barycenter of the four points.

2. The intersection of two straight lines that pass though the middle of the horizontal and vertical tangents.

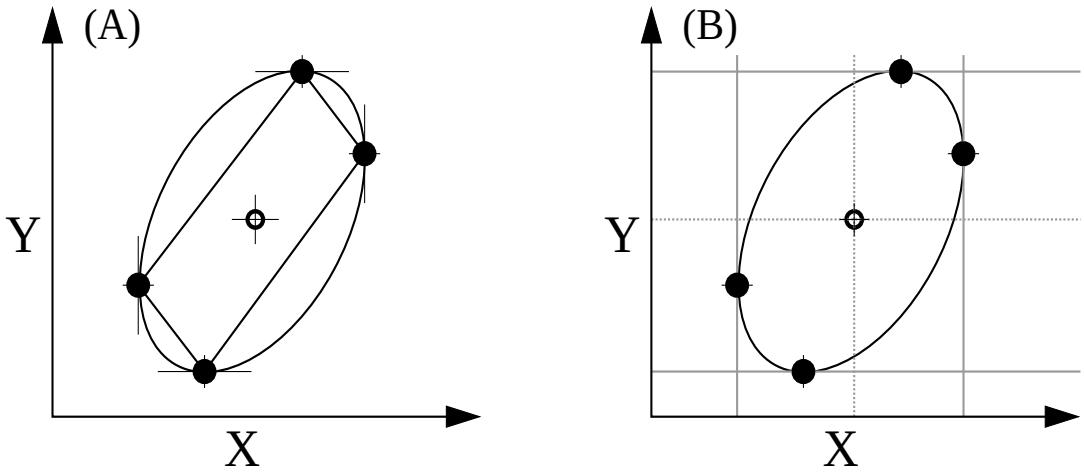

Figure 2.7: Illustration of local mean estimation in BEMD using (left) Barycenter of the four points, (right) Straight lines passing through the center of the tangents [22].

Figure 2.7 shows how the local mean of a bivariate signal can be calculated by the above two methods; the left figure illustrates the mean estimation by taking barycenter of four points, whereas, the figure on right shows the mean calculation via straight lines passing through the middle of the tangents. Figure 2.8 shows the decomposition obtained by applying BEMD to a complex real world wind signal[6]. It can be noticed that, similarly to RI-EMD, the method generates an equal number of IMFs for the real and imaginary parts and can therefore be given a physical meaning. Moreover, the residual signal r clearly captures the overall 'trend' of the real and imaginary components.

The BEMD algorithm extends the intuitive notion of 'oscillations' in standard EMD to its two dimensional counterpart–the rotations, thus yielding bivariate or complex intrinsic mode functions. The details of the sifting operation in BEMD is summarised in Algorithm 2; the rest of the method is similar to standard EMD, that is, if $d(t)$ meets the stoppage criterion for bivariate IMF, then the process is reapplied to $z(t) - d(t)$, otherwise, it is applied to $d(t)$. The stopping criterion used with the BEMD algorithm in this thesis is similar to the one employed for the standard EMD algorithm as given in section 2.4.2, with the same parameter values ($[\theta_1 = 0.05,\ \theta_2 = 0.5,\ \alpha = 0.05]$ and $S = 1$). The only difference is that the conditions for the stopping criteria are imposed on V multiple

[6]The complex wind signal has the north-south velocity as its real component and the east-west velocity as its imaginary component. The data was captured at 50 Hz.

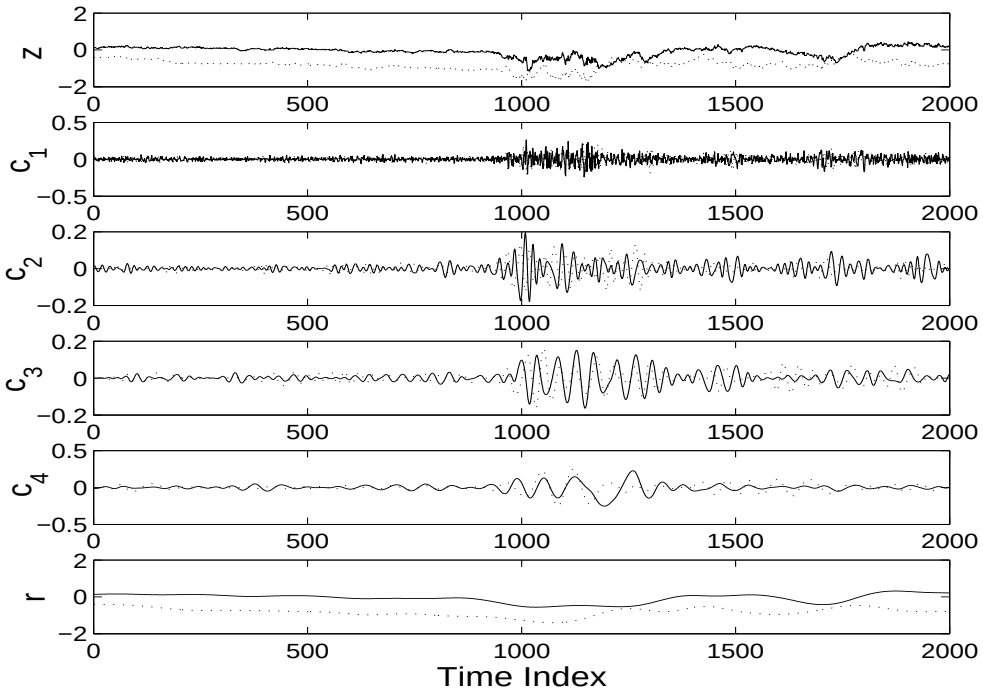

Figure 2.8: Wind data (denoted by z in the first row) decomposed by BEMD (IMFs denoted by $c_1 - c_4$ and 'trend' denoted by r in the lower subplots). Real and imaginary components are given by solid and dashed lines respectively.

projections each and the sifting process is stopped when all the projections fulfill these conditions.

Notice from RI-EMD and BEMD algorithms that the critical point in the complex extensions of EMD is to find the local mean of an input signal which, in turn, depends on the locations of its extrema. Since extrema of a complex signal can not be defined due to the property of complex fields [61], RI-EMD and BEMD employ projections of the input signal along multiple directions to estimate the mean value. While RI-EMD is a generic extension of standard EMD, it only uses projections in two directions to find the extrema, whereas bivariate EMD can take projections in any number of directions, in turn, yielding more accurate estimate of the local mean as compared to RI-EMD.

This issue is illustrated further in Figure 2.9 which graphically shows the process of finding the local mean of a complex signal using RI-EMD (Figure 2.9(a)) and BEMD

Algorithm 2 The sifting process in bivariate EMD

1: Obtain V signal projections, $\{p_{\theta_v}(t)\}_{v=1}^{V}$, by projecting the complex signal $z(t)$ by means of a unit complex number $e^{-\imath\theta_v}$, in the direction of θ_v, as

$$p_{\theta_v}(t) = \mathcal{R}\big(e^{-\imath\theta_v} z(t)\big),\ v = 1, \ldots, V \tag{2.30}$$

where $\mathcal{R}(\cdot)$ denotes the real part of a complex number, and $\theta_v = 2v\pi/V$;

2: Find the locations $\{t_j^v\}_{v=1}^{V}$ corresponding to the maxima of $\{p_{\theta_v}(t)\}_{v=1}^{V}$;

3: Interpolate (using spline interpolation) between the maxima points $[t_j^v,\ z(t_j^v)]$, to obtain the envelope curves $\{e_{\theta_v}\}_{v=1}^{V}$;

4: Calculate the mean, $m(t)$, of all the envelope curves;

5: Subtract $m(t)$ from the input signal $z(t)$ to yield an "oscillatory" component, that is, $d(t) = z(t) - m(t)$.

(Figure 2.9(b)), respectively. In both cases, envelopes were calculated in multiple directions, and then averaged to obtain the local mean. However, as expected, the estimates of BEMD were found to be more accurate than RI-EMD. This is evident in Figure 2.9(a), where the estimate of local mean using RI-EMD at around point 50 on X-axis is inaccurate due to limited number of projections $V = 2$, whereas, BEMD precisely calculated the mean value at that point since it used the larger number of projections $V = 4$.

2.8 Addressing the Problem of Uniqueness via BEMD

It was highlighted earlier that despite the potential of EMD in nonstationary signal analysis, it suffers from the problem of non-uniqueness due to its empirical nature and sensitivity to variations of its parameters (envelope estimation and stopping criteria) [17]. This problem was illustrated in section 2.6.1 via simulation on a sinusoid corrupted by different realizations of WGN, which yielded different sets of IMFs, as illustrated in Figure 2.5.

Given that both RI-EMD and BEMD process a bivariate signal directly in the complex plane, their potential with regards to data fusion was explored in [17], and it was

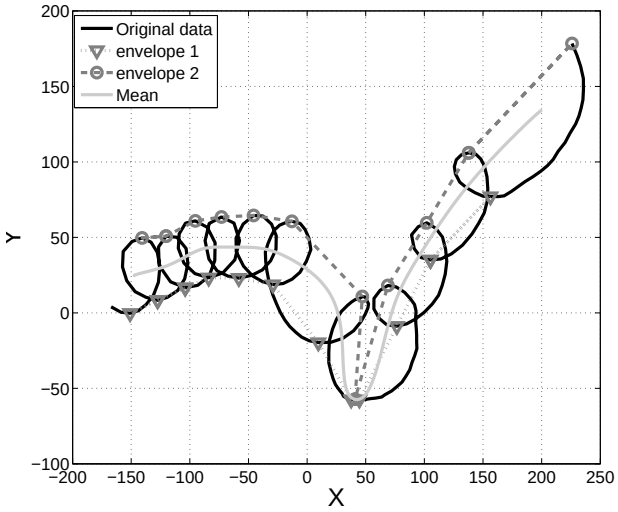

(a) Local mean estimation using RI−EMD

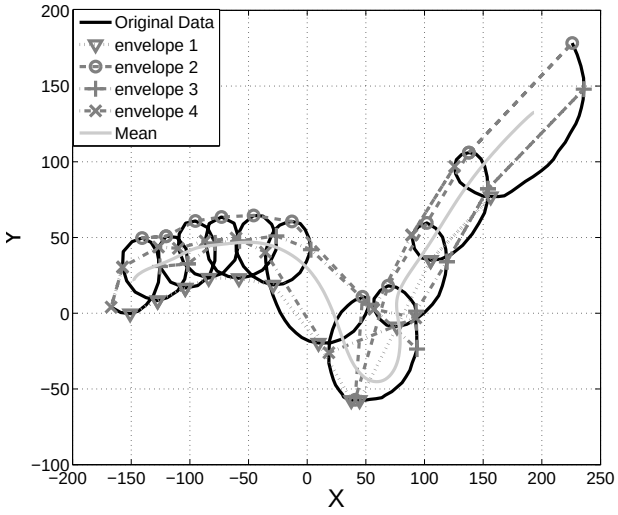

(b) Local mean estimation using BEMD (N=4)

Figure 2.9: Local mean of a bivariate signal calculated using the RI-EMD algorithm (a) and BEMD ($V = 4$) (b). Notice the inaccuracy in local mean estimation at around point 50 on X-axis, in (a), due to limited number of projections used in RI-EMD; BEMD on the other hand captured the signal dynamics more accurately.

found that they could address the uniqueness problem suffered by standard EMD. It was proposed to consider data from multiple sources as a single multivariate entity which, for two sources, allows the use of BEMD.

To demonstrate the ability of RI-EMD and BEMD in this regard, BEMD was applied to a complex signal $U + \imath V$, for which the real and the imaginary part, U and

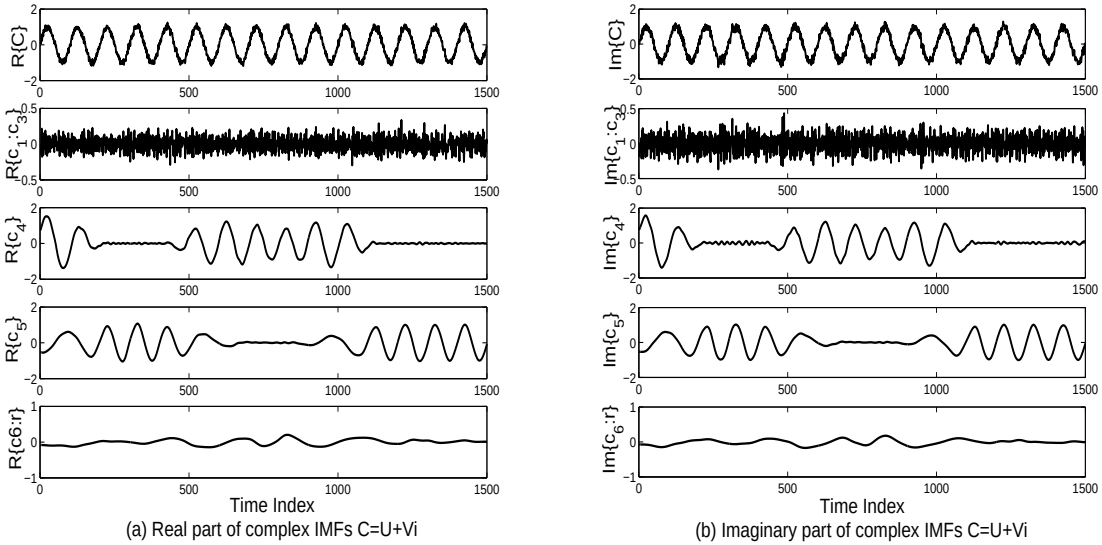

Figure 2.10: Uniqueness of BEMD: Decomposition of a complex signal, for which real and imaginary parts correspond to sinusoids with two different realizations of WGN, obtained by BEMD. Note that the mode-mixing occurs exactly at same points in both real and imaginary parts of complex IMFs.

V, are the same signals as those used in section 2.6.1 to study the non-uniqueness of standard EMD-based decomposition. Figure 2.10 shows the decomposition achieved by BEMD; Note that, as compared to Figure 2.5, the mode-mixing now occurs at exactly the same points in both channels. As a result, mode-mixing does not pose a problem and, therefore, the complex IMFs can be used in data-scale fusion applications. Due to this reason, complex extensions of EMD have also been successfully used to accurately measure the phase synchrony estimates between multichannel observations of EEG signals [19] [62].

2.9 Conclusions

Empirical Mode Decomposition (EMD) has shown considerable strength in the processing of nonlinear and nonstationary real world data. Its real potential lies in its fully adaptive nature, local orthogonality and completeness of its decompositions. However, despite the potential for EMD-based multiscale analysis, the problems of uniqueness and mode-mixing make it difficult to perform robust data-scale fusion.

Extensions of EMD to the complex domain $\mathbb{C}$ enable the modelling of amplitude-

phase relationships within the complex data, and also help with the problems of mode-mixing and the uniqueness of decomposition. However, to process a large class of multivariate signals containing more than two channels, extensions of EMD to process multivariate real world signals must be developed, which is the main aim of this thesis.

Chapter 3

Trivariate Empirical Mode Decomposition

IN this chapter, a trivariate empirical mode decomposition (TEMD) algorithm is presented, which has been designed to extend the EMD algorithm to process trivariate signals. Estimation of the local mean envelope of an input trivariate signal is performed by taking projections along multiple directions in three dimensional (3D) spaces, using the rotation property of quaternions. The proposed algorithm thus extracts rotating components embedded within the signal, and performs accurate time-frequency (TF) analysis, via the Hilbert-Huang transform. Simulations on synthetic and real world trivariate signals support the analysis.

3.1 Rationale: Extracting 3D Rotations

The main idea behind standard EMD method is to extract the local oscillations of the input signal which is intuitively related to the concept of local extrema. However, the notion of oscillations can not be easily extended to signals with more than one component as the concept of extrema is not properly defined for signals residing in higher dimensional spaces [61]; For instance, the complex field $\mathbb{C}$ is not ordered, and hence, operators such as $<$ and $>$ are not defined in $\mathbb{C}$. Therefore, the approach adopted in recent complex

extensions of EMD, including the rotation-invariant EMD (RI-EMD) and bivariate EMD (BEMD), aim to extract 2D rotational components, instead of oscillatory components, within the input bivariate signal [21] [22].

In the proposed trivariate extension of EMD (TEMD), the idea of rotations has been extended to three dimensions resulting in the notion of extracting 3D rotations in the case of trivariate signals. The main rationale behind the proposed TEMD algorithm, therefore, is to consider an input trivariate signal as consisting of faster 3D rotations imposed on slower 3D rotations. This concept is graphically illustrated in Figure 3.1 which shows a trivariate signal (top), its constituent slower 3D rotating component (middle), and higher 3D rotating component (bottom). Similarly to standard EMD, and also intuitively, the local mean of the input signal is considered as a slower rotating component, whereas the resulting residual, obtained by subtracting the mean from the original signal, is considered as a faster rotating component.

3.2 Local Mean Estimation in Trivariate Signals

The local mean estimation for univariate signals, in standard EMD algorithm, is not hard to achieve given that the upper (lower) envelope of a signal can be easily defined via spline interpolation of maxima (minima). For multivariate signals, however, it is a challenging task since the concept of extrema is not clearly defined in multidimensional spaces [61]. To alleviate this problem, recently proposed bivariate extensions of EMD [21] [22] employ the concept of taking multiple signal projections in 2D space to define multiple signal envelopes and, in turn, the local mean (see Section 2.7.3 for further details.).

To calculate the local mean of a trivariate signal, it is natural to consider taking signal projections in multiple directions in 3D spaces. Hence, effectively, a trivariate signal, for which the local extrema cannot be identified, is approximated via multiple univariate projections with each corresponding to a particular direction in 3D space. The extrema of these (univariate) projections can be easily defined and interpolated to yield multiple envelopes of the input trivariate signal which form a 3D tube tightly enclosing the signal.

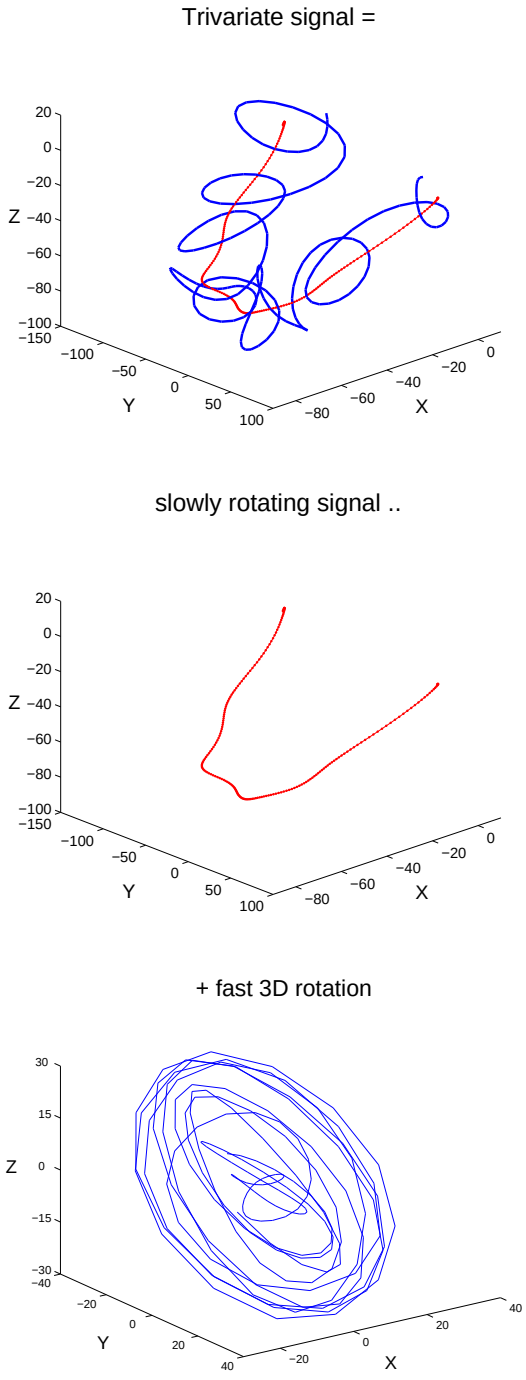

Figure 3.1: Principle of the trivariate extension of EMD: A composite trivariate signal (top) can be decomposed into slower rotation (middle), defined by its local mean, and faster rotations (lower), obtained from subtracting local mean from the input signal.

The local mean can then be considered as the center of this so-called 3D tube, and is calculated by taking the barycenter of these multiple envelopes.

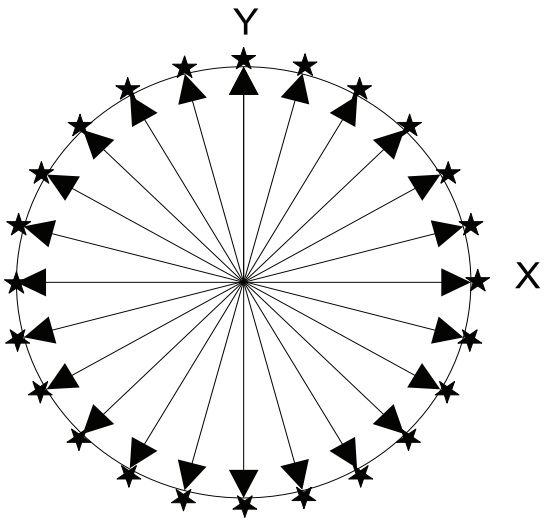

Figure 3.2: Set of direction vectors in 2D space used for calculating the local mean in BEMD, with $V = 24$ directions.

Since the local mean estimation is a crucial step in EMD and its proposed trivariate extension, its accuracy is vital for proper decomposition of signal into constituent 'local' scales. In the proposed method for mean estimation in trivariate signals, it is evident that its accuracy depends heavily on the estimation of enclosing 3D tube via multiple envelopes: the greater the number of envelopes used to form the tube, greater the accuracy of estimated local mean. One can also make an argument that since each envelope corresponds to a particular direction in 3D space, enlarging the set of envelopes means that we are effectively capturing the dynamics of the signal in more directions and, hence, in much wider area in 3D space resulting in accurate estimates of local mean. However, taking a larger set of envelopes comes at a high computational cost, and given the already intense computational requirements of EMD method, the number of envelopes must be carefully chosen in practice.

The density of envelopes is not the only issue effecting the accuracy of local mean; the choice of the set of direction vectors in 3D space is also very important in this regard and will be discussed in the next section.

3.3 Choosing the Set of Direction Vectors for Local Mean Estimation

The choice of the set of direction vectors to estimate signal envelopes is an important step to accurately determine the local mean of a trivariate signal. This is due to the fact that the chosen set of direction vectors determines how much 'weight' the proposed method gives to each direction in space, while calculating the local mean of a signal. Assuming no a priori information about the signal dynamics, the TEMD method should aim for a uniform set of vectors in 3D space.

Among the existing bivariate extension of EMD, RI-EMD uses only two direction vectors in a 2D plane, which correspond to the extrema of an imaginary part of a complex signal [21]; BEMD, on the other hand, uses a uniform set of direction vectors in 2D space taken along the polar coordinate system [22]. An example of a set of $V = 24$ sample vectors generated for the bivariate EMD are shown in Figure 3.2; it can be seen that the polar coordinate system inherently generates a uniform set of direction vectors in 2D space.

In the proposed extension for trivariate signals, the set of direction vectors corresponding to the spherical coordinate system is proposed to be used for local mean estimation. The spherical coordinate system is chosen since the input trivariate signal resides in 3D space and, hence, the direction vectors must also be distributed in the same (3D) space; the choice of spherical coordinate system, in this regard, can be seen as an extension of polar coordinate system used in BEMD, to 3D space.

For convenience of presentation, the direction vectors can be conveniently represented by points on the surface of a unit sphere: each point on the surface corresponds to the terminal point of a direction vector, drawn from the center of the sphere. One such point and its associated direction vector is shown Figure 3.3(a).

Assuming that envelope curves, e_θ^ϕ, are defined for any value of angles $0 < \theta \leq \pi$ and $0 < \phi \leq \pi$ in 3D space, then the envelope mean corresponding to the projections along points on a spherical coordinate system can be written as

$$m(t) = \frac{1}{\pi^2} \int_{\theta=0}^{\pi} \int_{\phi=0}^{\pi} e_{\theta}^{\phi} \, d\theta d\phi, \tag{3.1}$$

$$\approx \frac{1}{IJ} \sum_{i=1}^{I} \sum_{j=1}^{J} e_{\theta_i}^{\phi_j} \tag{3.2}$$

where I and J represent the number of directions chosen along azimuth (ϕ) and co-latitude (θ) respectively.

However, while projections of the input signal on points (direction vectors) along the spherical coordinate system, using equation (3.2), provide a reasonable estimate of local mean; it can be noticed from Figure 3.3(b) that there is greater concentration of points close to the North and South pole of the sphere, and therefore, the points close to the poles are given more weight in the calculation of the local mean signal. As a result, the method would not be strictly invariant to 3D rotations, although it spans the whole 3D space for a large number of points and hence provides a satisfactory solution.

To improve the algorithm in terms of invariance to 3D rotations, one solution is to make the average over the point set at least asymptotically uniform using an appropriate weighting. This asymptotic uniform weighting is very important as it would ensure that the dependency of the decomposition on the choice of axes can be made arbitrarily small. Computing the mean of the envelope curves is a numerical approximation of the uniform integral over all possible directions, and is thus related to the techniques of quasi Monte Carlo numerical integration [63]. In such techniques, the emphasis is on having the 'best point set', which can be evaluated using tools such as 'dispersion' or 'discrepancy'. However, having the 'best point set' is only necessary to compute the integral efficiently for finite point sets. Asymptotically, when the number of points tends to infinity, all point sets that converge to the same density will lead to convergence to the same integral.

Therefore, given a point set along a spherical coordinate system, a weighting scheme can be employed to make the average, given in equation (3.2), asymptotically uniform so that it converges to the correct integral. In that case, asymptotically rotation invariant average of envelopes can be taken on the surface of the sphere S using

$$m(t) = \frac{1}{4\pi}\iint_S e_\theta^\phi \, d\Omega \tag{3.3}$$

$$= \frac{1}{2\pi}\int_{\theta=0}^{\pi}\int_{\phi=0}^{\pi} e_\theta^\phi |\sin 2\theta| \, d\theta d\phi, \tag{3.4}$$

where $d\Omega = |2\sin 2\theta d\phi d\theta|$[1] corresponds to the differential solid angle on sphere S. The mean can then be approximated using the following summation

$$m(t) \approx \frac{\pi}{2IJ}\sum_{i=1}^{I}\sum_{j=1}^{J} e_{\theta_i}^{\phi_j} |\sin 2\theta_i| \tag{3.5}$$

The weighting factor $|\sin 2\theta_i|$ compensates for the higher density of the point set by giving smaller weights to envelopes near poles; this scheme, however, is not stable for smaller values of I and J.

3.4 The Trivariate EMD Algorithm

In trivariate EMD (TEMD) algorithm, the input signal is represented as a pure quaternion signal for convenience of representation and the computational gains which it offers as compared to $\mathbb{R}^2$. Moreover, the rotation property of quaternions is used to generate projections along multiple directions in 3D space to estimate the local mean.

As discussed earlier, a major challenge in extending standard EMD to trivariate signals is to find an accurate method for calculating the local mean, since the concept of extrema cannot always be rigorously defined for multivariate signals. For this cause, in TEMD algorithm, signal projections in multiple directions in 3D spaces are obtained, whose extrema are then interpolated using component-wise spline interpolation to yield pure quaternion-valued envelope curves. The use of component-wise spline interpolation

[1] For $\theta \in [0, \frac{\pi}{2}], 2\theta$ is the colatitude, hence the differential solid angle corresponding to (θ, ϕ) is $d\Omega = 2\sin 2\theta d\phi d\theta$; for $\theta \in [\frac{\pi}{2}, \pi], 2\theta,\ 2\pi - 2\theta$ is the colatitude, hence the differential solid angle is $d\Omega = -2\sin 2\theta d\phi d\theta$. This formula is not the standard one because the angle θ in this thesis is not the standard colatitude or latitude.

[2] See Appendix A for further details about the quaternion algebra and benefits of using the quaternion representation as compared to $\mathbb{R}^4$.

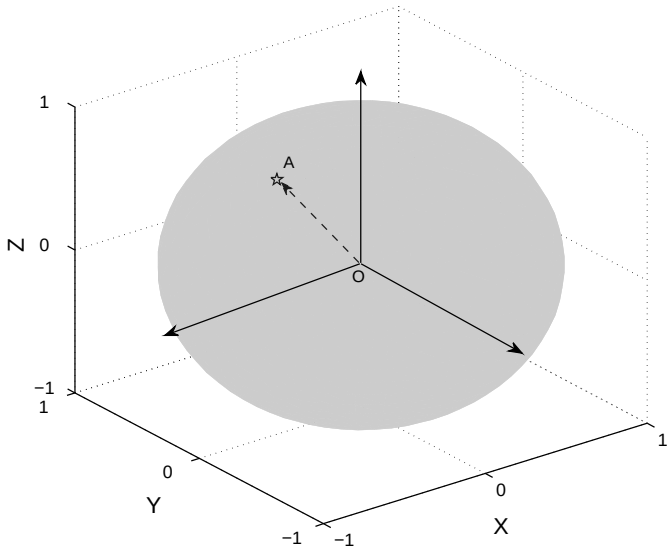

(a) A direction vector in 3D space

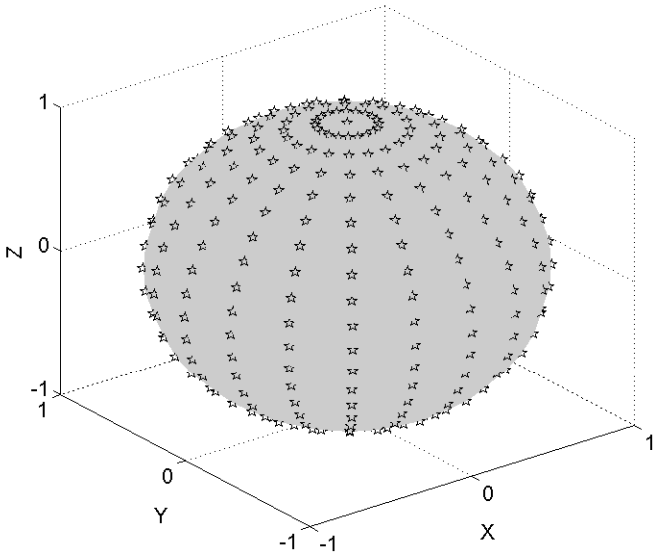

(b) Set of direction vectors in 3D space used in TEMD

Figure 3.3: Proposed set of direction vectors in 3D space for local mean estimation in TEMD: (a) The direction vector OA in 3D space, which has unit norm, can also be represented by a point on the surface of a unit sphere. (b) Set of direction vectors used for calculating the local mean in TEMD, with $V = 64$ directions. .

for pure quaternion signals represents an extension of the concept of 'complex splines', employed in RI-EMD and bivariate EMD. The resulting 'quaternion-valued envelopes' are then averaged to obtain an estimate of the local mean of a trivariate signal.

To obtain signal projections along different directions, multiple direction vectors are chosen in 3D space which can be represented by points on the surface of a unit sphere (Figure 3.3(a)). In TEMD, these direction vectors are taken along equidistant points on multiple longitudinal lines on the sphere, obtaining so-called 'equi-longitudinal lines'. The projections of an input signal along points (direction vectors) on an equi-longitudinal line can then be obtained by rotating the input signal along a rotation axis in the xy plane and mapping it along the z-axis.

Multiple points (direction vectors) on a single longitudinal line, corresponding to rotation axis q, along which signal projections can be taken, are shown in Figure 3.4(b). Every rotation in three dimensions can be treated as a rotation about an axis by a given angle. Thus, a unit quaternion, which gives an efficient and convenient mathematical notation for rotation using an angle-axis representation, is a natural choice for performing 3D rotations.

To take projections along direction vectors spanning the whole 3D space, multiple rotation axes along the xy plane are employed. By rotating the input signal along these axes, signal projections along directions corresponding to multiple equi-longitudinal lines on the surface of a sphere are taken, as shown in Figure 3.5. Since rotation axes are 3D vectors, they can also be represented by a set of unit quaternions $\mathbf{q}$ in the xy plane, under an angle ϕ to the x-axis as shown in Figure 3.4(a). Rotation axes, represented by a vector of quaternions $\mathbf{q}$, can therefore be expressed as

$$\mathbf{q} = 0 + cos(\phi)\imath + sin(\phi)\jmath + 0\kappa. \tag{3.6}$$

Since a trivariate signal can also be represented as a pure quaternion $x(t)$, its projections along multiple direction vectors on a sphere can be calculated by rotating it $\big($by using equation (A.7)$\big)$ about a set of vectors $\mathbf{q}$, by an angle 2θ, and then taking its projection along the z-axis (κ), using

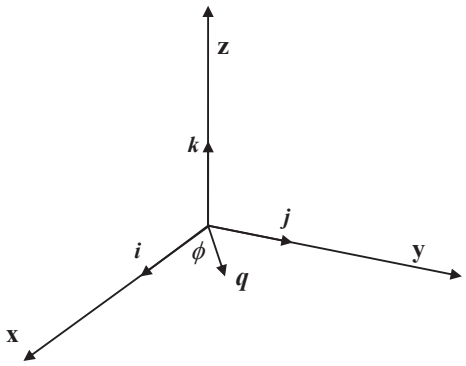

(a) Choice of a set of rotation axes q for obtaining multiple signal projections

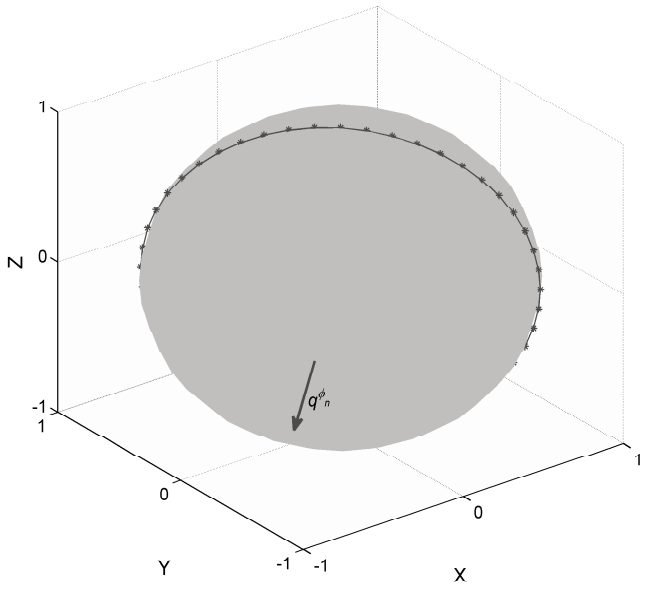

(b) Direction vectors on a longitudinal line

Figure 3.4: Generating multiple direction vectors on a 3D sphere. (a) Choices of rotation axes to obtain projections along multiple directions in 3D space. For projections along longitudinal lines on a sphere, multiple axes represented by a set of vectors q are chosen in the xy plane, with angle ϕ taken with respect to +x-axis. (b) Multiple direction vectors represented by points on a longitude line. Projections of the input signal are taken by rotation about the vector q^{ϕ}. To encompass the whole 3D space, direction vectors on multiple longitudinal lines should be considered.

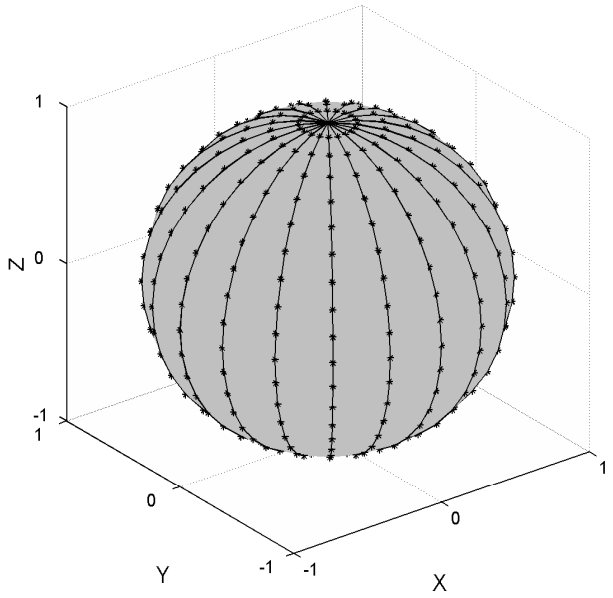

Figure 3.5: Points on multiple longitudinal lines on a sphere, representing directions along which projections of the input signal can be taken by rotating the input signal along rotation axes represented by a set of unit quaternions q

.

$$p_\theta^\phi = e^{\mathbf{q}\theta} x(t) (e^{\mathbf{q}\theta})^* \cdot \kappa \tag{3.7}$$

where symbol $(\cdot)$ denotes the dot product. To calculate the envelopes in multiple directions, angles ϕ and θ can be selected to have respectively J and I values between 0 to π. The range of π is necessary since both q and $-q$ give projections in the same direction and also because the application of a unit quaternion q represents rotation by an angle 2θ (See Appendix A for details).

While projections of the input signal on points (direction vectors) along equi-longitudinal lines on a sphere provide a reasonable solution, it can be noticed from Figure 3.5 that there is greater concentration of points close to the North and South pole of the sphere, and therefore, the points close to the poles are given more 'weight' in the calculation of the local mean signal. As a result, the method would not be strictly in-

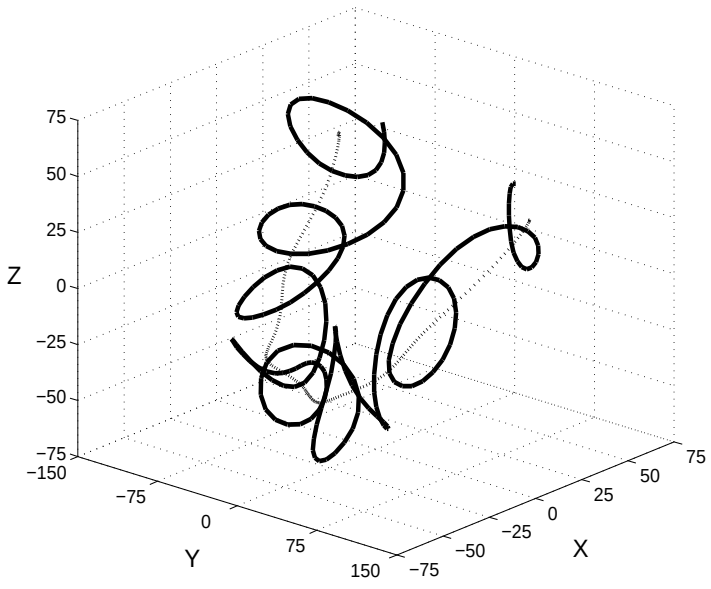

Figure 3.6: Local mean (dotted line) calculated for a trivariate signal (solid line) using equation (3.2)

.

variant to 3D rotations for a relatively small number of directions. However, for a large number of directions, the whole 3D space is spanned and the proposed method effectively becomes invariant to 3D rotations. Alternatively, one can adopt the weighting scheme given in equation (3.5). The extension of EMD for pure quaternion signals is summarized in Algorithm 3.

The stopping criterion used with the TEMD algorithm is similar to the one employed for the standard EMD algorithm as given in section 2.4.2, with the same parameter values ($[\theta_1 = 0.05,\ \theta_2 = 0.5,\ \alpha = 0.05]$ and $S = 1$). The only difference is that the conditions for the stopping criteria are imposed on $V = IJ$ number of multiple projections each and the sifting process is stopped when the stopping conditions are fulfilled for all those projections [3]. Figure 3.6 shows the results of employing the mean envelope, given in equation (3.2), for calculation of the local mean of a trivariate signal, using $I = 6$ and $J = 6$. Notice that the local mean correctly tracks the dynamics of the signal.

[3] A detailed illustration of the stopping criterion used for general multivariate extensions of EMD will be given in Section 4.4

Algorithm 3 Trivariate extension of EMD

1: Calculate projections, denoted by $p_{\theta_i}^{\phi_j}(t)$, of a trivariate quaternion signal $x(t)$ using equation (3.7), where $\theta_i = \frac{i\pi}{I}$ for $i = 1, \ldots, I$, and $\phi_j = \frac{j\pi}{J}$ for $j = 1, \ldots, J$;

2: Find the time instants $\{(t_i^j)_l\}$ corresponding to the maxima of $p_{\theta_i}^{\phi_j}(t)$, for all values of i and j;

3: Interpolate $[(t_i^j)_l, x((t_i^j)_l)]$ to obtain quaternion envelope curves $e_{\theta_i}^{\phi_j}$, for all i and j;

4: Compute the mean $m(t)$ of all the envelope curves by using equation (3.2);

5: Extract 'detail' $d(t)$ using $d(t) = x(t) - m(t)$. If $d(t)$ fulfills the stoppage criterion for a quaternion-valued IMF, then the above procedure is applied to $x(t) - d(t)$, otherwise it is applied to $d(t)$.

The original EMD method aims to extract the oscillatory components embedded in the data, called IMFs. The bivariate intrinsic mode functions, obtained from bivariate extensions of EMD, extend the notion of oscillation in two dimensions to extract 2D rotational modes. Similarly, the proposed method is designed to obtain rotational components in 3D spaces, if present, within the trivariate signal. The mean envelope, which defines the overall trend in the signal, is considered as a slowly rotating signal and is subtracted from the input signal until the 'detail' (fast rotating component) is extracted. While defining trivariate extensions of EMD in terms of rotations may seem restrictive in terms of the class of signals it can process, the proposed trivariate extension, like univariate and bivariate EMD, is fully capable of decomposing signals which may not be composed of rotations, e.g. white noise.

3.5 Simulation Results

This section presents the results of applying the TEMD algorithm to both synthetic data and real world trivariate orientation data respectively. The number of direction vectors used in the simulations were $V = I * J = 64$ ($I = 8$ and $J = 8$). The values of the parameters of the stopping criterion were $[\theta_1 = 0.05,\ \theta_2 = 0.5,\ \alpha = 0.05]$ and $S = 1$.

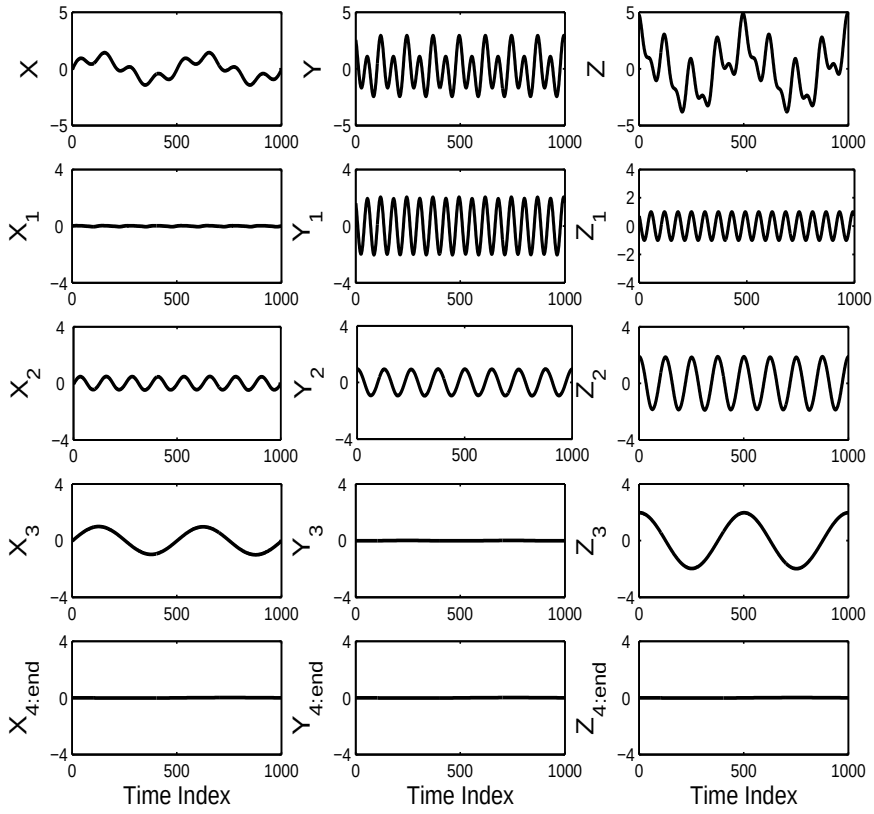

Figure 3.7: Decomposition of a synthetic quaternion signal, with multiple frequency modes, via the proposed trivariate EMD algorithm. Each quaternion-valued IMF carries a single frequency mode, thereby facilitating the alignment of common modes within different components of a trivariate signal.

3.5.1 Mode-Alignment in Synthetic Signals

The analysis of quaternion-valued IMFs on carefully designed trivariate synthetic signal is now presented to demonstrate their ability to align 'common scales' present within the data. Complex extensions of EMD, exhibiting similar mode aligning property have recently found application in data fusion [17]. The alignment of oscillatory modes of the input trivariate signal represented by pure quaternion IMFs allows to combine information of same nature from different IMFs, and hence, is expected to facilitate the fusion of information from up to three sources.

To illustrate the mode-alignment property of the proposed TEMD method, pure

quaternion signal was constructed from a set of three sinusoidal signals shown in the top row of Figure 3.7 (denoted by X, Y and Z). One sinusoid (8 Hz) was made common to all the components (X, Y, and Z), whereas the remaining two sinusoidal components were used so that the resulting signal had a common frequency mode in both Y and Z (16 Hz), and X and Z (2 Hz). The trivariate EMD algorithm was then applied to the resulting quaternion signal yielding multiple quaternion-valued IMFs, as shown in Figure 3.7. Observe that the sinusoid common to all the components of the input is the second IMF, whereas the remaining two frequency modes are present in IMFs one and three. Such mode-alignment cannot be achieved by using the real-valued EMD component-wise, as it generally does not yield the same number of IMFs per component.

3.5.2 TEMD of Trivariate Orientation Data (Tai-Chi sequence)

The decomposition of a real world trivariate signal is performed next using TEMD, and the results are shown in Figure 3.8. The signal represents a 3D orientation data generated by hand movements in a Tai Chi sequence, with a synthetically added mode for illustration purpose. The data was captured using an inertial 3D sensor from Xsens motion technology company.

As shown in Figure 3.8, different 3D rotating modes of the input trivariate signal are extracted by TEMD, whereby the lower index IMFs contain higher frequency 3D rotations and the higher index IMFs represent lower frequency rotating modes, as shown in Figure 3.8(left). The residual signal does not contain any 3D rotating components. Time plots of the individual components of input trivariate signal and their respective decomposition (IMFs) are also shown in Figure 3.8(right). The decomposition of individual components exhibits the mode-alignment property, whereby common frequency modes in different input components are aligned in a single IMF.

The significance of the mode-alignment observed in TEMD and EMD, applied channel-wise, may be evaluated by examining the normalised cross-correlation measure between IMFs in both cases. The larger the value of the correlation measure, the more significant is the mode-alignment and vice versa; such correlation measure $\Upsilon(m, m')$ can

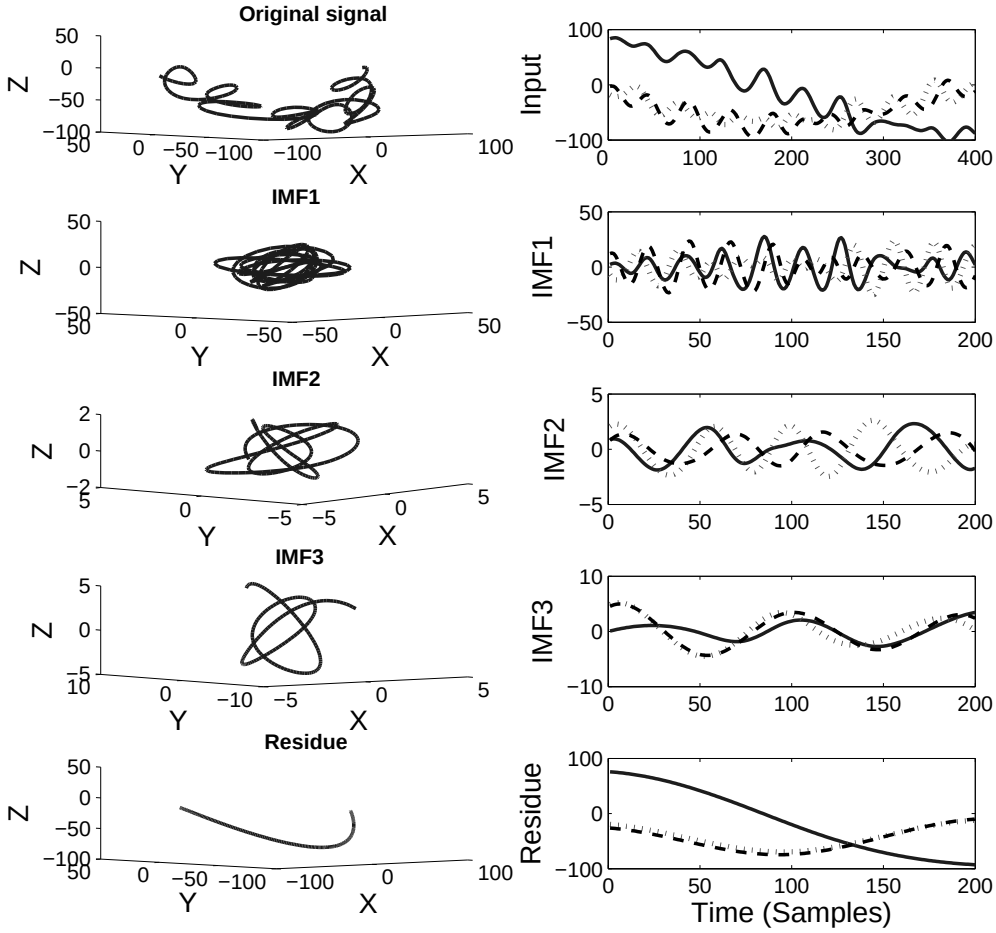

Figure 3.8: A trivariate signal and its decomposition obtained using the proposed method. (left) 3D plots of the input trivariate signal followed by the IMFs. (right) Time plots of the three components of the trivariate signal and their decomposition (X: dotted line, Y: solid line, Z: dashed line).

be given by

$$\Upsilon(m,m') = \left| \frac{1}{N} \sum_{j=1}^{N} \frac{\Upsilon^j(m,m')}{\sqrt{\Upsilon^j(m,m)\Upsilon^j(m',m')}} \right| \tag{3.8}$$

and

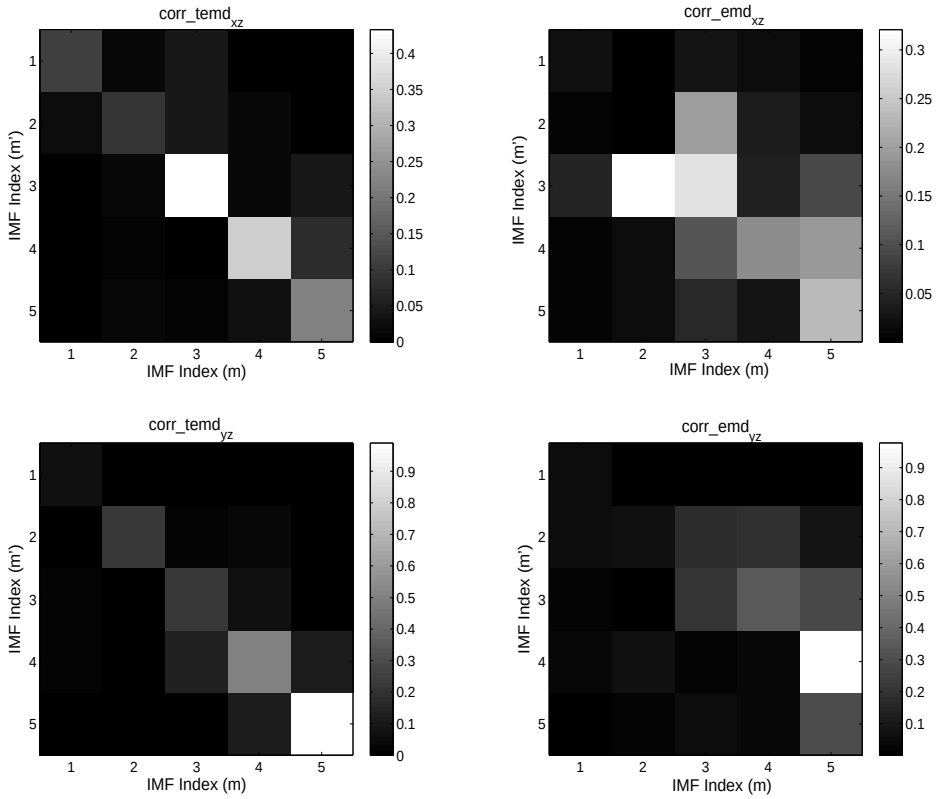

Figure 3.9: The schematic of the normalized IMF cross-correlation, given in equation (3.8), from multiple channels obtained via TEMD (left column) and EMD channel-wise (right column). The distribution of higher values of the cross-correlation measure along the diagonal line in the case of TEMD (left column) indicates the mode-alignment between IMFs from multiple channels. The IMF indices grow from left to right and from top to the bottom.

$$\Upsilon^j(m,m') = \frac{1}{K}\sum_{k=1}^{K}(c_m^j(k) - \mu_{c_m^j})(c_{m'}^j(k) - \mu_{c_{m'}^j}) \tag{3.9}$$

where $c_m^j(k)$ is the mth IMF of jth ensemble and $\mu_{c_m^j}$ denotes its mean value. An ensemble average over $N = 100$ noise realizations was taken to make the measure in equation (3.8), robust to noise.

A quantitative evaluation of this cross-correlation measure is plotted in Figure 3.9 for the IMFs obtained from TEMD (left column) and EMD channel-wise (right column), for the input signal given in Figure 3.8. It is evident that due to the mode-alignment in IMFs from TEMD, the values of the correlation measure are comparatively greater for

the same-indexed IMFs ($m = m'$) for any two given channels, as highlighted by higher correlation values at the diagonal of the subfigures[4] on the left column of the Figure 3.9. On the other hand, applying EMD separately on channels X, Y, and Z yielded miss-aligned IMFs, as evident from 'random' distribution of the correlation values in the right hand side of the Figure 3.9.

3.5.3 Time-Frequency Analysis of Trivariate Wind Signal

In this set of simulations, an application of TEMD in time-frequency (TF) analysis of a trivariate wind[5] signal was conducted. TF analysis of wind can provide important information in order to identify critical episodes of wind behaviour, including gusts and turbulence. Traditional Fourier-based spectral methods are bound to fail in those cases due to the nonstationarity of the wind signal. The East, North, and Upward velocity, shown in Figure 3.10(a), are represented as X, Y and Z components of the pure quaternion signal $x(t)$, that is

$$x(t) = 0 + X\imath + Y\jmath + Z\kappa. \tag{3.10}$$

Figure 3.10(b) shows the trend in the wind dynamics visualized through the mean envelope of trivariate wind signal. Figure 3.10(a) also shows segments of the wind signal with different dynamics, denoted respectively by 'A', 'B', and 'C'. A wind regime with high dynamic ('A') exhibits larger changes in wind speed in relatively small time intervals, and should contain high frequency components in the corresponding Hilbert-Huang spectrum, while medium ('B') and lower dynamic ('C') regimes are expected to contain predominantly lower frequency components.

This is illustrated in Figure 3.11, which shows the Hilbert-Huang spectra of the wind signal from Figure 3.10. The spectrum of the North wind speed component (see Figure 3.11(b)), belonging to the low dynamics wind regime, was mostly dominated by

[4]Since the input signal is trivariate, the correlation measure is shown for a couple of pairs of variates: XZ and YZ.

[5]Thanks to Gill Instruments Ltd. who have provided WindMaster, a 3D ultrasonic anemometer, used for wind readings.

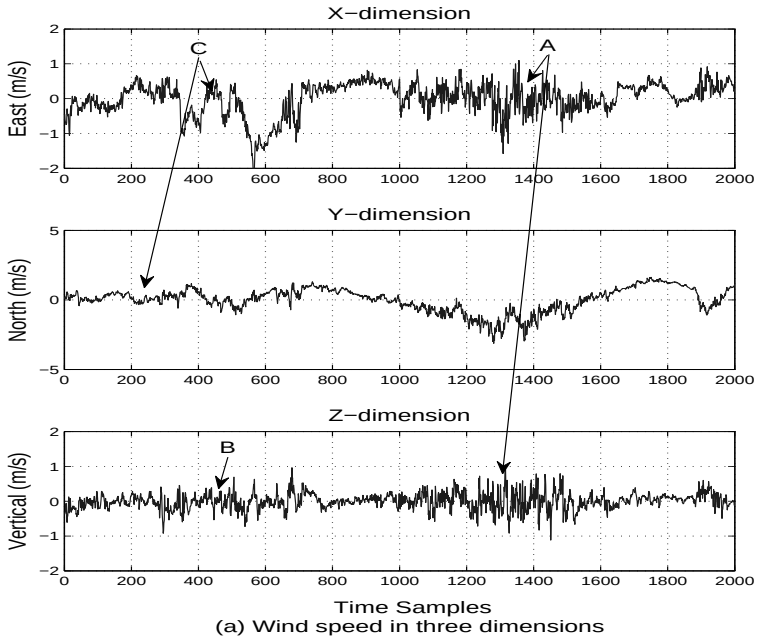

(a) Wind speed in three dimensions

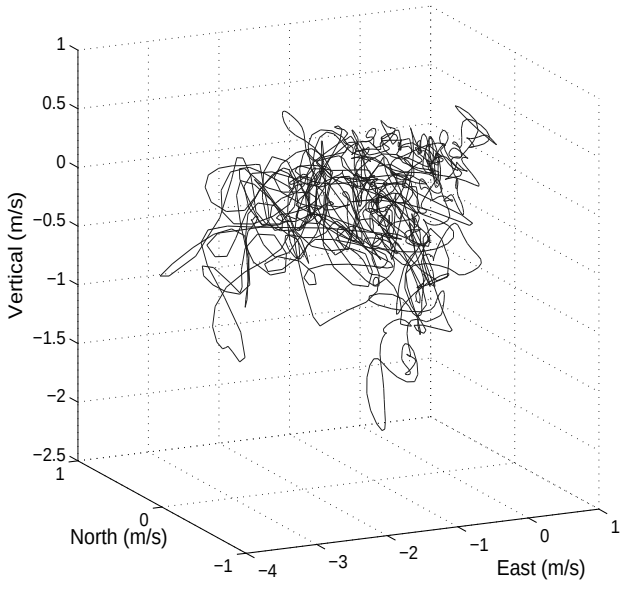

(b) Mean envelope of trivariate wind signal

Figure 3.10: A trivariate wind signal represented as a pure quaternion. (a) Wind speed in the east-west (X), north-south (Y) and the vertical (Z) direction. Wind regime with high dynamics is denoted by 'A'. The regimes with mild and low dynamics are denoted by symbols 'B' and 'C'. (b) The 3D local mean of the wind signal from (a), obtained by applying the mean-envelope detection method, given in Algorithm 3.

low frequency components. Wind regimes denoted by 'C' had mostly lower frequency components in the corresponding frequency spectrum, for instance, around sample 500 in

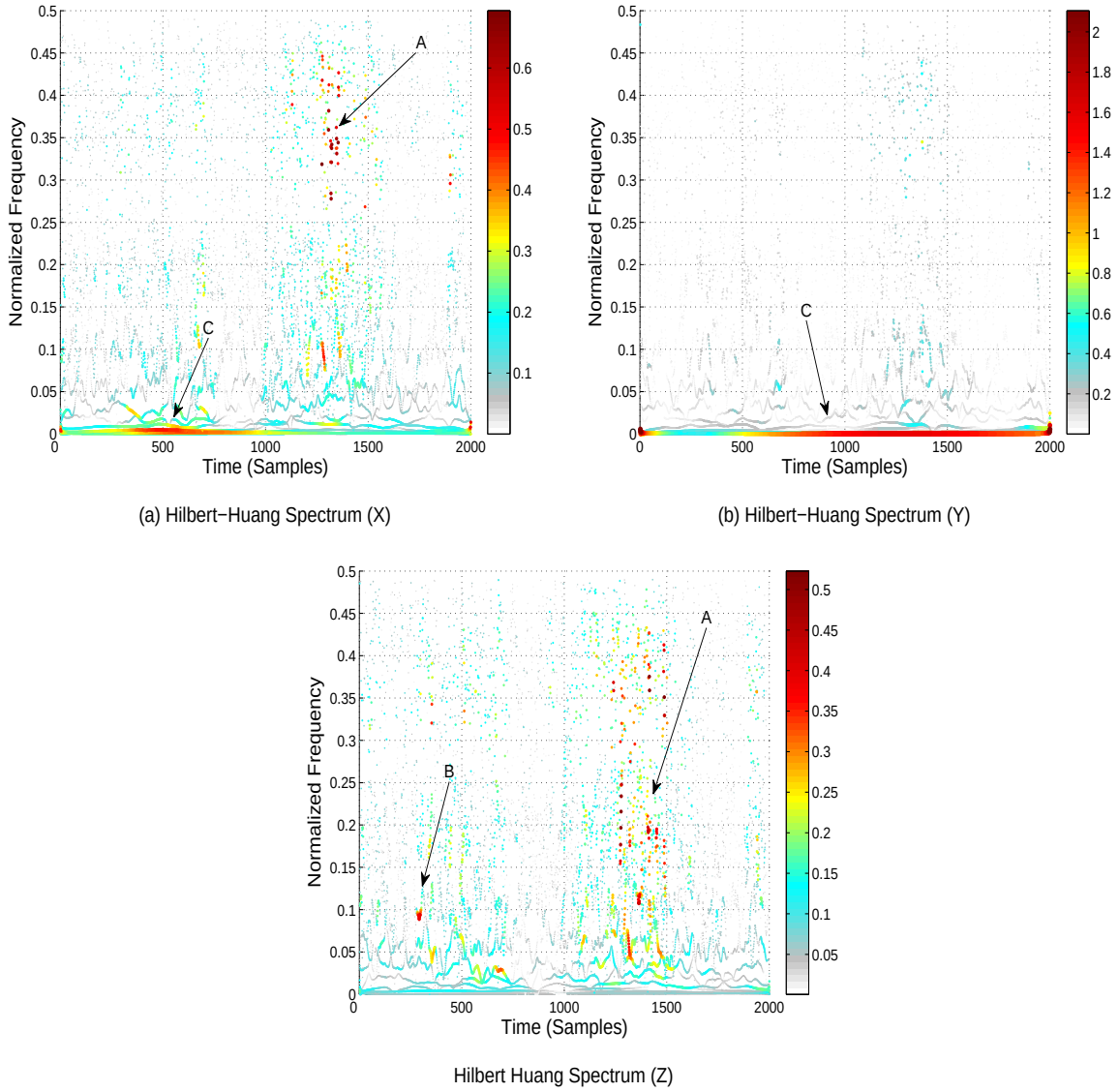

Figure 3.11: Hilbert-Huang spectra of IMFs of wind signal components in (a) east-west direction (b) north-south direction and (c) vertical direction.

Figure 3.11(a). In contrast, for wind regimes with high dynamics, the spectrum had more pronounced magnitudes at higher frequencies. The high variations in the wind speed in the Upward and the East components, observed at samples 1200-1400, can be clearly observed in the corresponding spectra in Figure 3.11(a) and Figure 3.11(c), showing the power is spread over a wide range of frequencies, exhibiting several bursts at high frequency.

3.6 Qualitative Analysis of Quaternion IMFs from TEMD

this would be the hypothesis that the data has been generated by a stationary Gaussian linear stochastic process (equivalently, an autoregressive moving average or ARMA process)

For real world processes, signal modality characterization, that is the degree of linearity/nonlinearity[6] and determinism/stochasticity is of great interest. Moreover, in the absence of nonlinear behaviour in a signal, it is unnecessary to use nonlinear methods. Since EMD is a powerful signal decomposition tool and has been applied in conjunction with adaptive filtering [64], it is crucial to establish whether the modality of the original signal is altered by EMD. To this end, Chen *et al.* have provided a qualitative assessment of the IMFs of the standard EMD [65]. However, as multivariate extensions of EMD are only emerging, the nature of multivariate IMFs also needs to be explored.

To this end, a qualitative analysis of the quaternion-valued IMFs within TEMD algorithm is presented; more precisely, some intricate properties of the quaternion (pure) IMFs, such as its (non-)linearity and determinism, are investigated to establish whether these IMFs preserve the nature of the original signal in phase space. It is important, for instance, in the data fusion methods for the modelling of the relevance of input variables [66]. This is achieved by using the delay vector variance (DVV) method, within the surrogate data framework, which examines the signal predictability in phase space to assess the determinism and nonlinearity within the signal[7]. This analysis is vital since an insight into the role of IMFs from TEMD is a prerequisite to applying the algorithm to real world nonlinear and nonstationary signals.

3.6.1 How Informative are Quaternion IMFs?

To provide qualitative assessment of the quaternion-valued IMFs generated from TEMD, following on [65], the DVV method is employed. The DVV scatter plots are generated for

[6]Linear signal here refers to the one that has been generated by a stationary Gaussian linear process or equivalently, by an autoregressive moving average or ARMA process[94].

[7]Appendix B gives more detail on DVV method and the surrogate data framework.

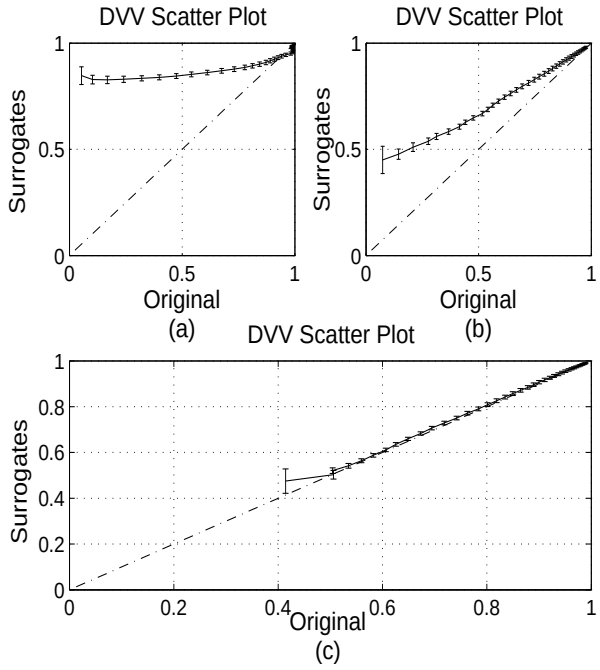

Figure 3.12: Component-wise DVV scatter plots for pure quaternion signal $Q(t)$ (a) Henon map $X(t)$; (b) real world wind signal $Y(t)$; (c) linear AR(2) signal $Z(t)$.

two cases: the sum of first and second quaternion IMFs, and the sum of all the remaining IMFs. The root mean squared (rms) value is calculated over the difference between the local variance of the original signal and that of individual IMFs. This metric is then used to quantify the degree of similarity between the DVV scatter plots of the original signal and that of the IMFs, and is given by

$$\epsilon = \sqrt{\frac{1}{N} \sum_{\text{valid } r_d} (\sigma^{*2}_{ori}(r_d) - \sigma^{*2}_{imf}(r_d))^2}, \tag{3.11}$$

where $\sigma^{*2}_{ori}(r_d)$ denotes target variance, at span r_d, for the original signal, and $\sigma^{*2}_{imf}(r_d)$ denotes the variance value for an individual IMF, and N is the number of valid variance (r_d) values. The greater the value of the above metric for any two given signals, the greater the difference in their fundamental properties in phase space.

To perform both the qualitative and quantitative analysis of IMFs from trivariate EMD, for illustration, a pure quaternion signal was generated, consisting of three signals

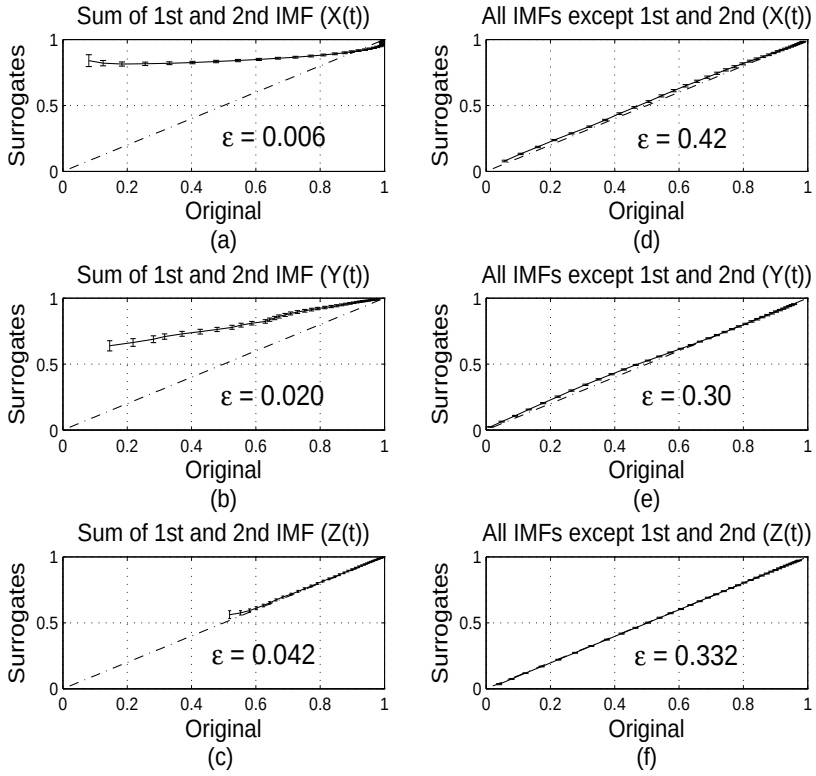

Figure 3.13: DVV scatter plots and the corresponding values of similarity measure (3.11) for the three components X, Y, and Z (a,b, and c) the sum of the 1st and 2nd IMFs generated from TEMD algorithm; (d,e, and f) the sum of remaining (all except IMF1 and IMF2) IMFs.

of different nature, that is

$$Q = 0 + X\imath + Y\jmath + Z\kappa \tag{3.12}$$

Signal $X(t)$ was a realization of Henon map, a chaotic nonlinear signal, given by

$$\begin{aligned} x_n &= 1 - ax_{n-\beta}^2 + y_{n-\beta} \\ y_n &= bx_{n-\beta} \end{aligned} \tag{3.13}$$

where β was set to unity, and parameters a and b were respectively set to 1.4 and 0.3. The x-component of the Henon map was used in simulations.

Signal $Y(t)$ was chosen as a vertical speed component of the real world wind signal,

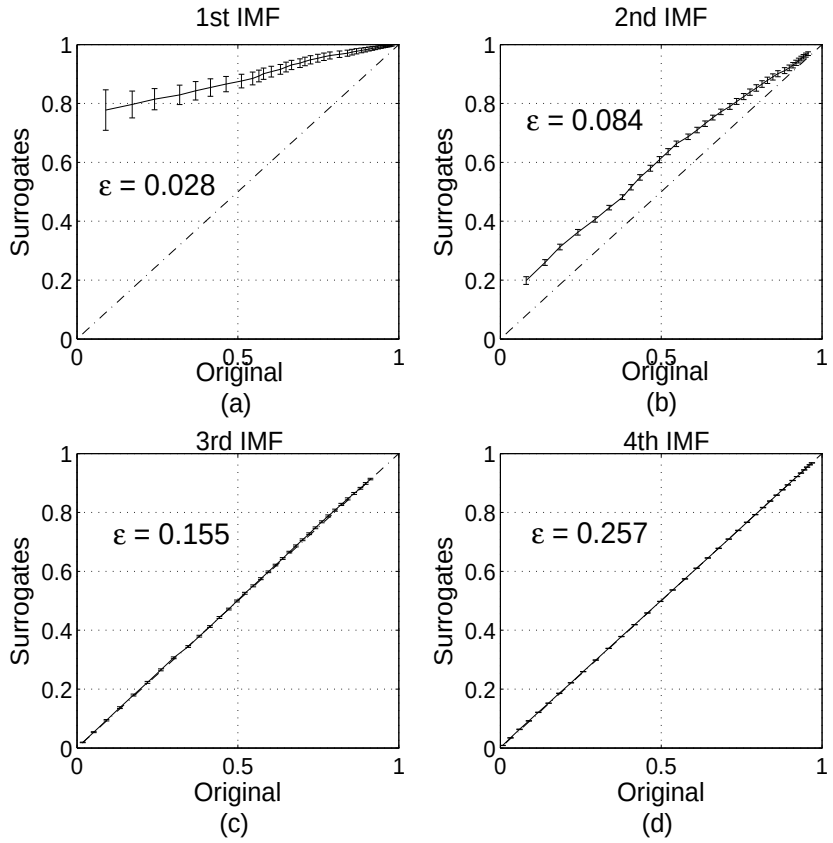

Figure 3.14: DVV scatter plots of 1st IMF (a); 2nd IMF (b); 3rd IMF (c); and 4th IMF (d) of $X(t)$, generated by TEMD.

while $Z(t)$ was a benchmark linear AR(2) signal, given by

$$z(k) = 0.8z(k-1) + 0.1z(k-2) + w(k) \tag{3.14}$$

where $w(k)$ is white Gaussian noise (WGN) signal of zero mean and unit variance.

Figure 3.12 shows the DVV scatter plots of the three components of $Q(t)$. Observe that for Henon map $X(t)$, the scatter plot deviates away from the bisector line, indicating its nonlinear behaviour. For the linear AR(2) signal $Z(t)$, the plot coincides with the bisector line, indicating its linear nature, whereas $Y(t)$ was either nonlinear or/and nonstationary.

In the modality analysis of quaternion IMFs, TEMD algorithm was used to process

the quaternion signal given in equation (3.12); the DVV method was then applied to all the three components of resulting quaternion IMFs, and the corresponding scatter plots were analysed. The metric in equation (3.11) was used to quantify the degree of similarity between the scatter plots of IMFs and those of the original signal shown in Figure 3.12. Figure 3.13 shows the DVV scatter plots of the components of the sum of 1st and 2nd IMFs of a quaternion signal $Q(t)$ (Figure 3.13(a), 3.13(b), and 3.13(c)), and scatter plots of the remaining IMFs (Figure 3.13(d), 3.13(e), and 3.13(f)), together with their corresponding values of similarity metric. Notice that the sum of first two IMFs preserve the original nature for all three components of the input signal $Q(t)$, which is also manifested by the corresponding low values of similarity metric; while the sum of the rest of the IMFs have relatively large values of the similarity metric, showing that the original signal modality is not contained in lower IMFs. In order to further explore the contribution of individual IMFs, the DVV scatter plots of the X-component of $Q(t)$ for the first four IMFs are separately plotted in Figure 3.14. Again, the values of similarity metric show that the first two IMFs preserve the signal modality, while the remaining IMFs are largely linear and predictable (deterministic).

3.7 Conclusions

An extension of empirical mode decomposition (EMD) in order to make it suitable for the processing of trivariate signals has been proposed. The trivariate signal is represented as a pure quaternion and the rotation property of unit quaternions is employed to obtain multiple projections of the input signal along "equi-longitudinal" lines on a sphere, thus offering a compact and convenient mathematical representation. The method extracts the 3D rotating components of the input trivariate signal, and also generates common oscillatory modes, facilitating the fusion of information from multiple sources. Simulations on real world trivariate data have also illustrated the potential of TEMD in time-frequency (TF) analysis.

Chapter 4

Multivariate Empirical Mode Decomposition

RECENT advances in the sensor and engineering technologies have brought to light a new class of multivariate signals containing multiple channels [61]. Currently, these signals are mostly processed channel-wise [14] [67] [23], but their simultaneous analysis is a prerequisite for a better understanding of the underlying signal generating mechanism. Given that the empirical mode decomposition (EMD) has the potential to become a standard for the decomposition and time-frequency (TF) analysis of nonlinear and nonstationary signals, its extensions to multivariate signals are, therefore, imperative for accurate analysis of such processes.

In complex domain, the mode-alignment property of bivariate EMD (BEMD) has already proven to facilitate its applications in data fusion [17] and phase synchrony measurement [19], by circumventing the mode-mixing problem experienced with standard EMD. Multivariate extensions of EMD are also expected to achieve mode-alignment for multivariate data, which corresponds to finding a set of common modes across different channels of a multivariate signal, thus ensuring that the IMFs are matched both in their number and scale properties. Using such extensions will also allow us to develop robust frameworks for data fusion, for data sets containing any number of input channels.

Recently, the mode-alignment in standard EMD-based decomposition has also been

attempted by clustering the IMFs corresponding to their spectral similarity [68] [69] [70]. However, such methods result in complex cluster 'dendograms' which are specifically hard to interpret for multivariate signals with large number of channels. Multivariate extensions of EMD, on the other hand, are expected to provide a simpler and more elegant solution by automatically generating similar modes, in the same-indexed IMFs, from multiple channels.

To this end, a new algorithm, namely multivariate empirical mode decomposition (MEMD), has been presented in this chapter for extending EMD to process a signal containing any number of data channels. The rationale of the proposed method is first presented followed by the discussion on the choice of a suitable set of direction vectors in multidimensional space for calculation of the local mean signal. Next, the MEMD algorithm is formally presented along with the discussion on possible stopping criteria for MEMD sifting algorithm. Finally, the potential of the proposed algorithm to find common oscillatory modes within multivariate data is demonstrated by simulations performed on both synthetic and real world signals.

4.1 Rationale: Extracting Rotations in $\mathbb{R}^n$

The rationale behind the proposed multivariate extension of EMD (MEMD) is that it aims to extract local rotational components from within the input signal; while BEMD and TEMD look for 2D and 3D rotational components, MEMD separates rotational components in $\mathbb{R}^n$.

The key issue in EMD algorithm is the computation of the local mean of the original signal, a step which depends critically on finding the local extrema. However, as already mentioned, for multivariate signals, this is not straightforward; for instance, the complex and quaternion fields are not ordered [61]. This problem is alleviated by using multiple real-valued projections of the signal; the extrema of such projected signals are then interpolated component-wise to yield multidimensional envelopes of the signal. The envelopes obtained this way are then averaged to give an estimate of the local mean. More

specifically, if $e_{\{\theta_1,\theta_2,\cdots,\theta_{n-1}\}}$ denotes the envelope in the direction represented by a vector $\theta = \{\theta_1, \theta_2, \cdots, \theta_{n-1}\}$ in $\mathbb{R}^n$, then the local mean can be estimated by using

$$m(t) = \frac{1}{2\pi^{n-1}} \int_{\theta_1=0}^{\pi} \int_{\theta_2=0}^{\pi} \cdots \int_{\theta_{n-1}=0}^{2\pi} e_{\{\theta_1,\theta_2,\cdots,\theta_{n-1}\}}\, d\theta_1 d\theta_2 \cdots d\theta_{n-1}, \tag{4.1}$$

$$\approx \frac{1}{V_1 V_2 \ldots V_{n-1}} \sum_{v_1=1}^{V_1} \sum_{v_2=1}^{V_2} \cdots \sum_{v_{n-1}=1}^{V_{n-1}} e_{\{\theta_{v_1},\theta_{v_2},\cdots,\theta_{v_{n-1}}\}} \tag{4.2}$$

By comparing the above equation with equation (3.2) for trivariate signal mean, it is evident that the local mean estimate in MEMD is an extension of TEMD mean in $\mathbb{R}^n$. The choice of a suitable set of direction vectors $\theta_{\mathbf{v}} = \{\theta_{v_1}, \theta_{v_2}, \ldots \theta_{v_{n-1}}\}$ in $\mathbb{R}^n$, however, is a crucial and a more challenging step in MEMD algorithm and is discussed next.

4.2 Choosing the Set of Direction Vectors for Multivariate Signals

The choice of a suitable set of direction vectors for estimating local mean is important as it is proposed to generate multiple envelopes by taking signal projections in $\mathbb{R}^n$; these envelopes are then averaged to obtain the local mean. This idea of mapping an input multivariate signal into multiple real-valued projected signals, to generate multidimensional envelopes, can be seen as a generalisation of the concept employed in existing bivariate [22] and trivariate [71] extensions of EMD.

Since the calculation of the local mean for multivariate signals can be considered as an approximation of the integral of all the envelopes along multiple directions in $\mathbb{R}^n$, as shown in equation (4.2), the accuracy of this approximation is dependent on the uniformity of the chosen set of direction vectors. This is especially relevant if one only has a finite number of direction vectors. Therefore, the issue of choosing a suitable set of direction vectors for taking signal projections in $\mathbb{R}^n$ needs special attention.

In order to represent direction vectors in n-dimensional (nD) space, for convenience

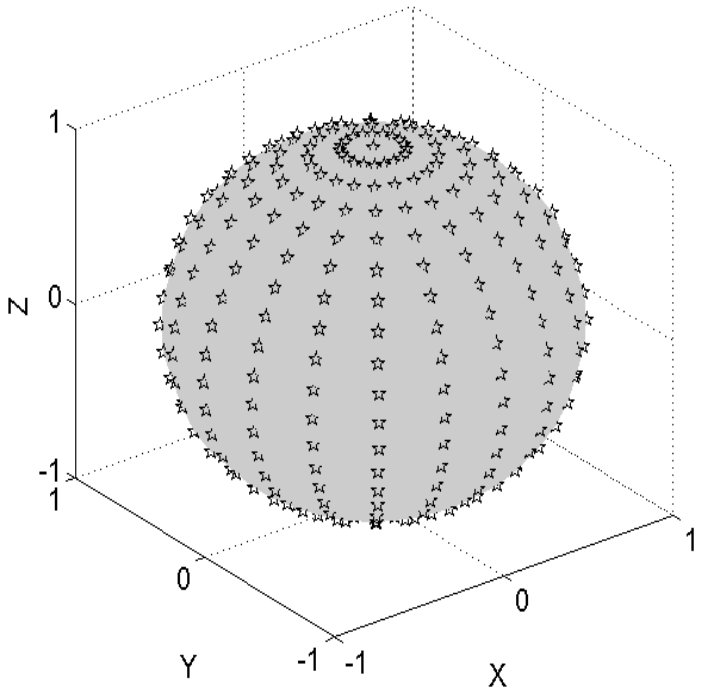

Figure 4.1: Set of direction vectors in 3D space obtained from equation (4.4), for $n = 2$. Note the nonuniform density of points at the poles.

of presentation, sample points on the surface of corresponding unit $(n-1)$-spheres are considered[1]. The corresponding direction vector can then be seen as the one originating from center of the $(n-1)$-sphere to that point on its surface; refer to Figure 3.3 for its graphical representation in the case of a sphere (2-sphere). It is important to mention that the direction vectors are chosen in $\mathbb{R}^n$ since the input multivariate signal resides in that space. We adopt the terminology that an n-sphere resides in an $(n+1)$-dimensional Euclidean coordinate system ($\mathbb{R}^{n+1}$), therefore, the problem of finding a suitable set of direction vectors $\mathbb{R}^n$ can be treated as that of finding a uniform sampling scheme on an $(n-1)$-sphere.

[1] An n-sphere, or equivalently a hypersphere, can be considered as an extension of the ordinary sphere to an arbitrary dimension and is represented mathematically in equation (4.3), given in the next section.

4.2.1 Uniform Angular Sampling on n-sphere

A simple and practically convenient choice for a set of direction vectors is to employ uniform angular sampling of a unit $(n-1)$-sphere in hyperspherical coordinate system ($\mathbb{R}^n$). The resulting set of direction vectors covers the whole $(n-1)$-sphere, as shown in Figure 4.1 for a particular example of a 2-sphere. For the generation of a point set on an $(n-1)$-sphere, consider an $(n-1)$-sphere with center point $c_j = \{c_1, c_2, \ldots, c_n\}$ and radius R, given by

$$R = \sum_{j=1}^{n} (x_j - c_j)^2. \tag{4.3}$$

A coordinate system in an nD Euclidean space ($\mathbb{R}^n$) can then be defined to serve as a point set (and the corresponding set of direction vectors) on an $(n-1)$-sphere. Let $\{\theta_1,\ \theta_2, ...,\ \theta_{(n-1)}\}$ be the $(n-1)$ angular coordinates of a point in $\mathbb{R}^n$, then an nD coordinate system, having $\{x_i\}_{i=1}^{n}$ as the n coordinates on a unit $(n-1)$-sphere, is given by:

$$\begin{aligned}
x_1 &= cos(\theta_1) \\
x_2 &= sin(\theta_1) \times cos(\theta_2) \\
x_3 &= sin(\theta_1) \times sin(\theta_2) \times cos(\theta_3) \\
&\vdots \\
x_{n-1} &= sin(\theta_1) \times \cdots \times sin(\theta_{n-2}) \times cos(\theta_{n-1}) \\
x_n &= sin(\theta_1) \times \cdots \times sin(\theta_{n-2}) \times sin(\theta_{n-1}).
\end{aligned} \tag{4.4}$$

where θ_{n-1} ranges over $[0,\ 2\pi]$ radians and the other angles range over radians $[0,\ \pi]$.

Note that the set of direction vectors in BEMD and TEMD are also based on the point set given in equation (4.4), for special cases of $n = 1$ and $n = 2$ respectively. However, while the given point set corresponding to this uniform angular coordinate scheme is very convenient to generate, it does not provide a uniform sampling distribution for $n > 1$. Therefore, while the point set used in BEMD ($n = 1$) is inherently uniform, the one used

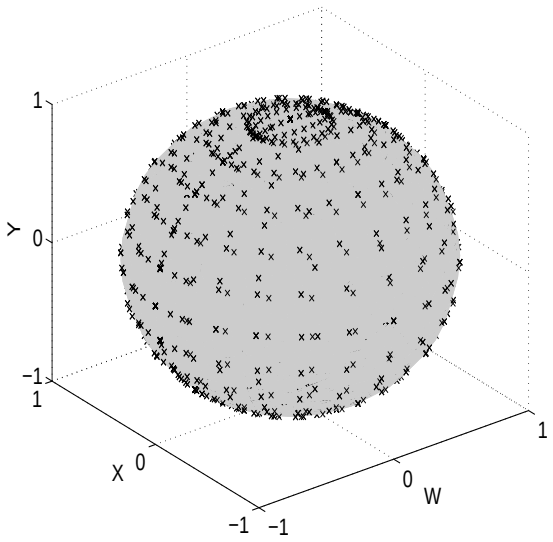

(a) Sampling a hypershpere (3−sphere) using uniform angular sampling method (WXY axes shown)

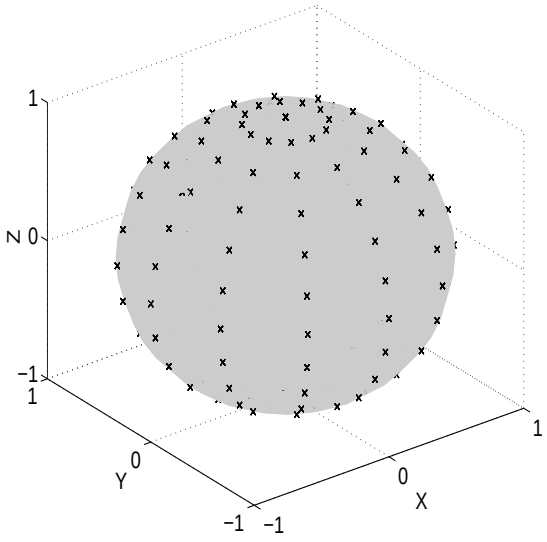

(b) Sampling a hypershpere (3−sphere) using uniform angular sampling method (XYZ axes shown)

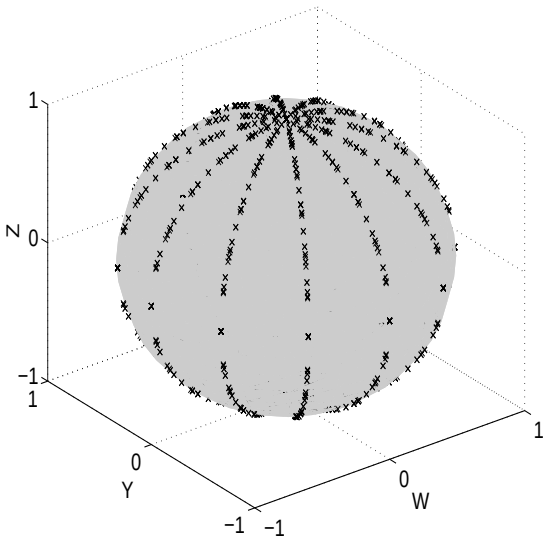

(c) Sampling a hypershpere (3−sphere) using uniform angular sampling method (WYZ axes shown)

Figure 4.2: Direction vectors for taking projections of a quaternion signal on a unit four dimensional sphere (3-sphere) generated by using a uniform angular sampling method, for n=4, given in equation (4.4). For visualization purposes, the point set is plotted on three unit spheres (2-spheres), defined respectively by WXY, XYZ, and WYZ axes.

in TEMD ($n = 2$) is non uniform. This is illustrated in Figure 4.1 where a higher density of the points is observed when approaching the poles of a 2-sphere ($\mathbb{R}^3$).

Apparently, this non uniformity of sample points in multidimensional space in-

creases for larger values of n. To demonstrate this further, Figure 4.2 shows the direction vectors on a 3-sphere[2] generated by uniform angular sampling using equation (4.4). A visual comparison of this point set with that on a 2-sphere, as shown in Figure 4.1, confirms that for higher dimensional problems, the performance of uniform angular coordinate system gets worse. Therefore, while uniform angular sampling serves the purpose well in the case of $\mathbb{R}^2$ (BEMD) and $\mathbb{R}^3$ (TEMD), it may not be optimal for extending EMD to higher dimensions, $n > 3$.

4.2.2 Sampling based on Vertices of Polyhedron

A better solution in the case of 2-sphere, in terms of the uniformity of point set, would be to base the choice of projections on the faces or vertices of regular polyhedron inscribed in a 2-sphere. The chosen polyhedron can be a: tetrahedron (4 faces, 4 vertices), hexahedron (6 faces, 8 vertices), octahedron (8 faces, 6 vertices), icosahedron (20 faces, 12 vertices), and dodecahedron (12 faces, 20 vertices). Hence, the choice of direction vectors is limited to 20 for this case, and therefore, rotation invariance can not be achieved using this set of directions.

Another option could be to consider the imperfect regular polyhedra like the ones found in the fullerenes molecules, the most well-known being the C_{60} or bucky ball. Its dual structure is a familiar soccer ball design which consists of 32 regular polyhedra (20 hexagons and 12 pentagons), giving only 60 possible choices of projections; research is still going on to find larger stable fullerenes. The limited choice of direction vectors offered by these polyhedra, therefore, is again a limiting factor. The point set on a 2-sphere corresponding to a bucky ball structure is shown in Figure 4.3.

To increase the number of possible projected directions on a sphere using these polyhedra, a triangulation method [72] could be another option: For instance, for an icosahedron (20 faces, 12 vertices) inscribed within a sphere, the triangulation process can be initiated by connecting the midpoints of the sides of each triangular face of an icosahedron, giving four new triangles for each face. The midpoints of each new triangles

[2]Note that while ideally, the point set should be plotted on a 3-sphere, for visualization purposes, direction vectors on three 2-spheres (WXY, XYZ, and WYZ) have been shown.

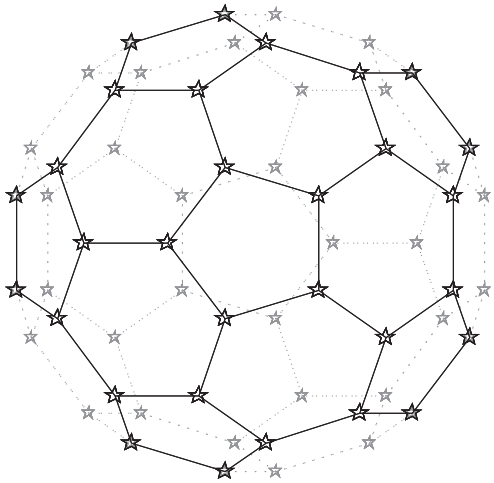

Figure 4.3: Set of direction vectors in $\mathbb{R}^3$ corresponding to a bucky ball structure.

are then radially projected outwards to the surface of the sphere, giving added points on the sphere. This process can be repeated until the desired density of points on the sphere is achieved. However, the number of points added between two iterations of triangulation process is very large, thus, limiting the number of directions that can be taken on a sphere. Moreover, these points are not uniformly distributed since the new triangles, obtained by joining the midpoints of the sides of icosahedron's faces, generally do not all have the same area, and thus their middle points are not equidistant from each other. A similar type of method can be used with other polyhedra, such as hexahedron (cube) inscribed in a sphere, but it also yields somewhat distorted grid on a sphere [73].

4.2.3 Sampling based on Low-Discrepancy Point Set

In numerical analysis, a class of techniques known as the quasi-Monte Carlo method is normally adopted which uses the low-discrepancy sequences for the computation of integrals. These low-discrepancy sequences are related to the mathematical concept of discrepancy which can be seen as a quantitative measure for irregularity or nonuniformity of a distri-

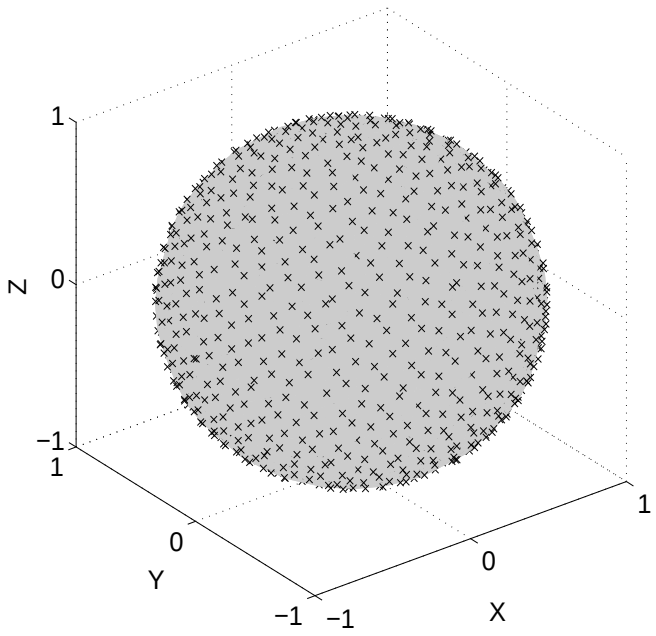

Figure 4.4: Set of direction vectors in 3D space obtained from low-discrepancy Hammersley sequence.

bution[3]. The low-discrepancy sequences are, therefore, more uniformly distributed and provide an accurate estimate of integrals in the case of a finite point set.

Since the computation of local mean via envelope curves is a numerical approximation of the uniform integral over all possible directions in $\mathbb{R}^n$, as evident from equation (4.2), it can also be achieved via quasi-Monte Carlo integration techniques. Using this technique, the low-discrepancy sequences are used to generate uniform point set on $(n-1)$-sphere for generating signal envelopes along direction vectors which are evenly distributed in $\mathbb{R}^n$, ensuring more efficient and accurate implementation of the integral given in equation (4.2) for a given finite point set.

A convenient method for generating multidimensional low-discrepancy sequences involves the family of Hammersley sequences, which are proven to show considerable improvement, in terms of error bounds, over other standard methods [63]. It has also been shown [74] [75] that the set of direction vectors on 2-sphere, generated by the Hammersley

[3]See Appendix C for more details on the discrepancy measure.

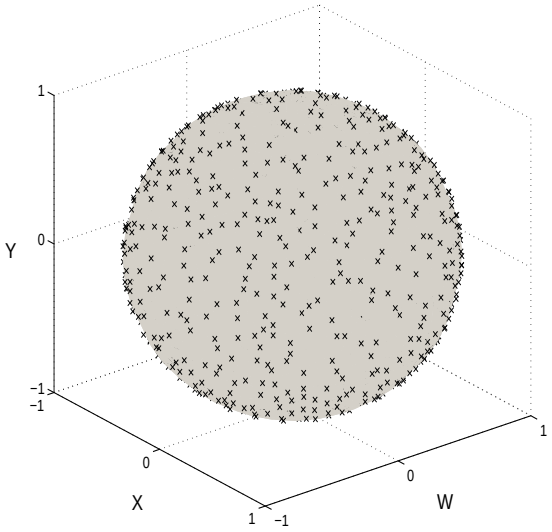

(a) Sampling a hypersphere (3−sphere) using low discrepancy sequence (WXY axes shown)

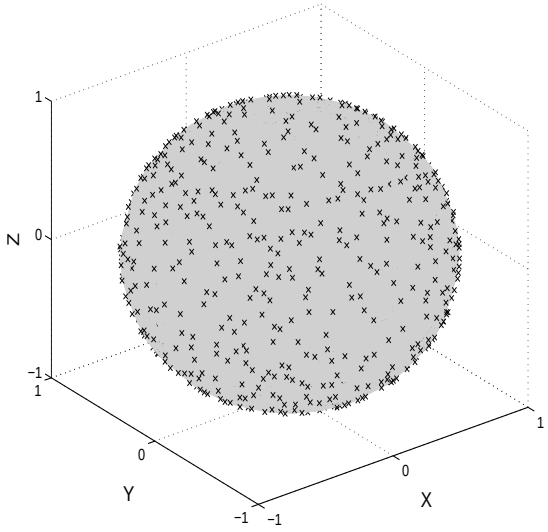

(b) Sampling a hypersphere (3−sphere) using low discrepancy sequence (XYZ axes shown)

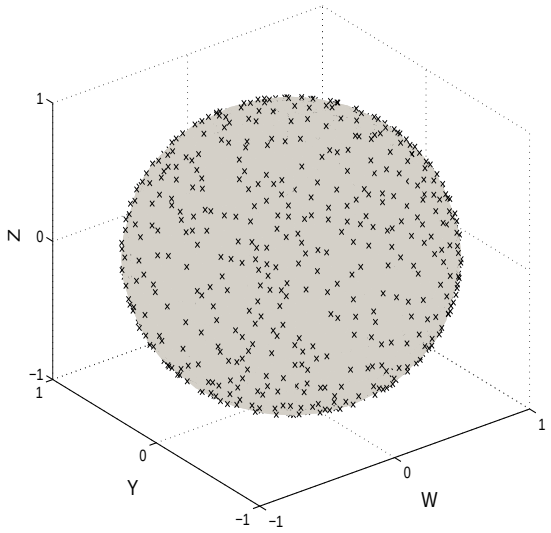

(c) Sampling a hypersphere (3−sphere) using low discrepancy sequence (WYZ axes shown)

Figure 4.5: Direction vectors for taking projections of a quaternion signal on a unit four dimensional sphere (3-sphere) generated by using the Hammersley sequence. For visualization purposes, the point set is plotted on three unit spheres (2-spheres), defined respectively by WXY, XYZ, and WYZ axes.

sequence, yields lower discrepancy estimate as compared to other sampling methods, and hence, is comparatively more uniformly distributed on a sphere. Details about generating the Hammersley sequences, and their corresponding projections on $(n-1)$-sphere ($\mathbb{R}^n$) can be found in the Appendix C.

It is worth mentioning here that the quasi-Monte Carlo methods using low-discrepancy sequences provide improved error bounds as compared to the standard Monte Carlo methods which are based on pseudorandom sequences. Also, developing multivariate extensions of EMD via standard Monte Carlo methods would result in probabilistic error bounds: any two applications of the algorithm with similar input signal and parameters may yield different decompositions. Hence, in the proposed multivariate extension of EMD, the point set for generating direction vectors is generated using the low-discrepancy Hammersley sequence.

To illustrate the benefits of the proposed scheme, Figure 4.4 and Figure 4.5 show, respectively, the point set on the surface of a sphere (2-sphere) and hypersphere (3-sphere), generated by the low-discrepancy Hammersley sequence. Observe that, as desired, the points generated by the low-discrepancy method are more uniformly distributed as compared to the point set generated by uniform angular sampling method, which are shown in Figure 4.1 and Figure 4.2. In Figure 4.5, the point set should have been plotted on a 3-sphere, however, for visualization purposes, representations of direction vectors are shown separately on three 2-spheres.

4.3 Multivariate EMD Algorithm

Given that a suitable set of direction vectors on $(n-1)$-sphere has been generated using the low-discrepancy Hammersley sequence, projections of the input signal are calculated along this set. The extrema of such projected signals are then interpolated component-wise to yield multidimensional envelopes of a multivariate signal. The multiple envelope curves, each corresponding to a particular direction vector, are then averaged to obtain multivariate signal mean.

More specifically, consider a sequence of n-dimensional vectors $\mathbf{s}(t) = \{s_1(t), s_2(t), \ldots, s_n(t)\}$, representing a multivariate signal with n components, and $\mathbf{x}_{\theta_v} = \{x_1^v, x_2^v, \ldots, x_n^v\}$ denoting a set of $v = 1, 2, \ldots, V$ direction vectors along the directions given by angles $\theta_{\mathbf{v}} = \{\theta_{v_1}, \theta_{v_2}, \ldots \theta_{v_{n-1}}\}$ in $\mathbb{R}^n$. Then, the proposed multivariate extension

of EMD suitable for operating on general nonlinear and nonstationary multivariate time series is summarised in Algorithm 4.

Once the first IMF is extracted, it is subtracted from the input signal and the same process (Algorithm 4) is applied to the resulting signal yielding the second IMF and so on; the process is repeated until all the IMFs are extracted and only a residual is left; in the multivariate case, the residual corresponds to a signal whose projections do not contain enough extrema to form a meaningful multivariate envelope.

Algorithm 4 Multivariate EMD

1: Choose a suitable point set for sampling an $(n-1)$-sphere;

2: Calculate a projection, denoted by $p_{\theta_v}(t)$, of the input signal $\mathbf{s}(t)$ along the direction vector $\mathbf{x}_{\theta_v}$, for all v (the whole set of direction vectors), giving $p_{\theta_v}(t)\}_{v=1}^{V}$ as the set of projections;

3: Find the time instants $\{t_{\theta_v}^i\}_{v=1}^{V}$ corresponding to the maxima of the set of projected signals $p_{\theta_v}(t)\}_{v=1}^{V}$;

4: Interpolate $[t_{\theta_v}^i, \mathbf{s}(t_{\theta_v}^i)]$ to obtain multivariate envelope curves $\mathbf{e}_{\theta_v}(t)\}_{v=1}^{V}$;

5: For a set of V direction vectors, the mean $\mathbf{m}(t)$ of the envelope curves is calculated as:

$$\mathbf{m}(t) = \frac{1}{V}\sum_{v=1}^{V}\mathbf{e}_{\theta_v}(t) \tag{4.5}$$

6: Extract 'detail' $\mathbf{d}(t)$ using $\mathbf{d}(t) = \mathbf{s}(t) - \mathbf{m}(t)$. If $d(t)$ fulfills the stoppage criterion for a multivariate IMF, apply the above procedure to $\mathbf{s}(t) - \mathbf{d}(t)$, otherwise apply it to $\mathbf{d}(t)$.

4.4 Stopping Criterion for Multivariate IMFs

The sifting process for a multivariate IMF can be stopped when all the projected signals fulfill any of the stoppage criteria adopted in standard EMD. One popular stopping criterion used in EMD stops the sifting when the number of extrema and the zero crossings

differ at most by one for S consecutive iterations of the sifting algorithm [46]. However, caution must be exercised while using this criterion for multivariate cases as it has been found to be computationally very expensive for long signals.

Another criterion introduces an evaluation function based on the envelope amplitude, which is given by

$$\mathbf{a}(t) = \frac{1}{V}\sum_{v=1}^{V} |\mathbf{e}_{\theta_v}(t) - \mathbf{m}(t)| \tag{4.6}$$

The sifting process is continued until the value of the evaluation function, defined as $f(t) = \left|\frac{\mathbf{m}(t)}{\mathbf{a}(t)}\right|$, where $\mathbf{m}(t)$ is the local mean signal, is less than or equal to predefined thresholds $[\theta_1 theta_2 \alpha]$ [50].

Similarly to the BEMD and TEMD algorithm, both the above criteria are used in combination to give a robust stopping criterion for MEMD: the conditions of both the above stopping criteria are imposed on V number of multiple projections each. The sifting process is stopped when the stopping conditions are fulfilled for all those projections.

4.5 Simulation Results

Simulations[4] were conducted on both synthetic signal and a real world multivariate inertial body motion recording. For all signals, the low-discrepancy Hammersley sequence was used to generate a set of $V = 512$ direction vectors for taking signal projections, and the stopping criteria given in equation (4.6) was used. The values of the parameters of the stopping criterion used in the subsequent simulations were $[\theta_1 = 0.05,\ \theta_2 = 0.5,\ \alpha = 0.05]$ and $S = 1$.

4.5.1 Common Mode-Alignment using Multivariate IMFs

Similarly to bivariate [22] and trivariate [18] extensions of EMD, MEMD algorithm has the ability to align 'common scales' in multivariate data: similar oscillatory scales are aligned in the same-indexed IMFs from multiple channels. Such mode-alignment helps to

[4]The simulations were performed in Matlab using the MEMD toolbox provided at: http://www.commsp.ee.ic.ac.uk/∼mandic/research/emd.htm.

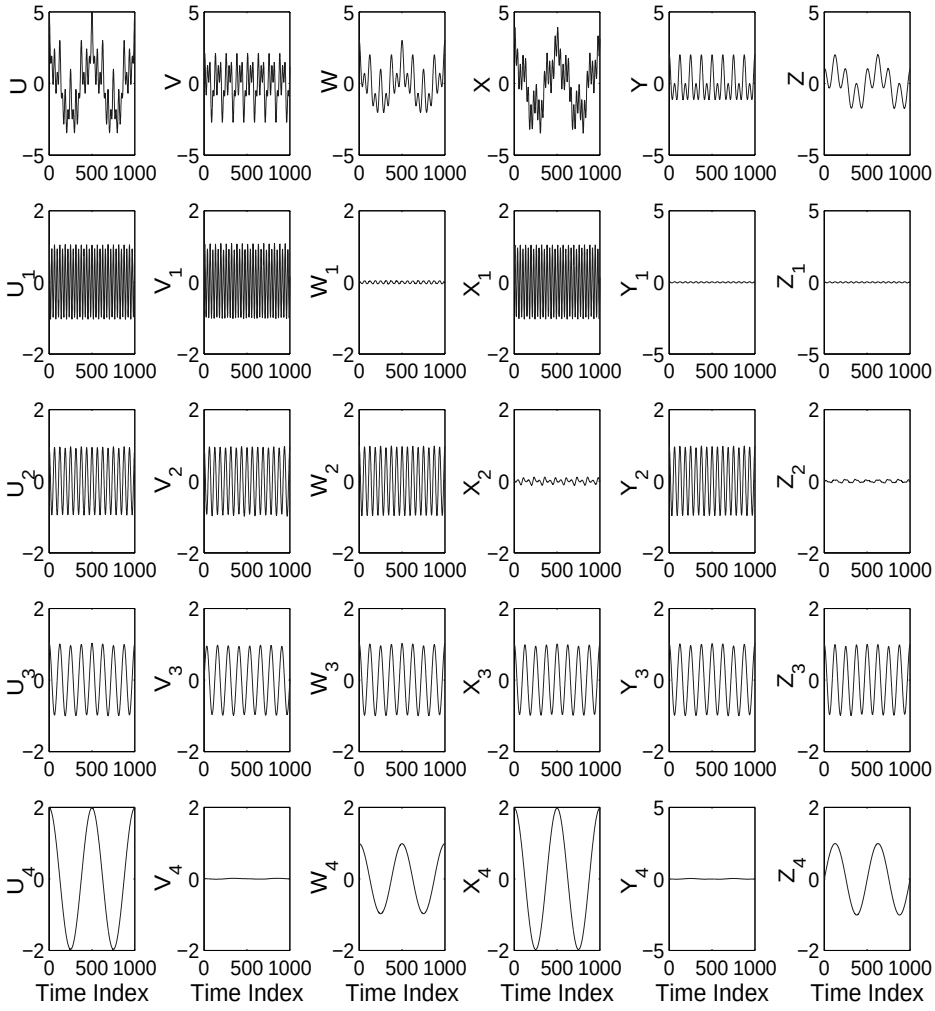

Figure 4.6: Decomposition of a synthetic multivariate signal (U, V, W, X, Y, Z) exhibiting multiple frequency modes, via the proposed multivariate EMD algorithm. Each IMF carries a single frequency mode, illustrating the alignment of common scales within different components of a multivariate signal.

identify similar scales in different data sources, and hence, can be used for data fusion purposes [66].

To illustrate the mode-alignment property of the proposed method, a synthetic hexavariate time series was analysed; each component (variate), shown in the top row of Figure 4.6 (denoted by U, V, W, X, Y and Z), was constructed from a set of four

sinusoids. One sinusoid was made common to all components, whereas the remaining three sinusoidal components were combined so that the resulting signal had a common frequency mode in each $UVWY$, UVX, and $UWXZ$ components. The MEMD algorithm was then applied to the resulting hexavariate signal yielding multiple IMFs, as shown in Figure 4.6. Observe that the sinusoid common to all components of the input signal is the third IMF, whereas the remaining three frequency modes were also accurately extracted in the respective IMFs. Such mode-alignment cannot be achieved by the standard EMD applied component-wise, as it generally does not yield the same number of IMFs per component.

4.5.2 MEMD of Hexavariate Orientation data (TaiChi)

To illustrate the ability of MEMD algorithm to extract common modes within multivariate real world signals, the body motion data recorded in a Tai Chi sequence is next considered. The data was captured using two inertial 3D sensors attached to the left hand and the left ankle; these were combined to form a single hexavariate signal. The common rotational modes were found within multiple hexavariate IMFs, and the components corresponding to the hand and the ankle are plotted separately as 3D plots in Figure 4.7. Observe that each such IMF represents a unique rotational mode embedded within the original trivariate signal. Unlike the TEMD method applied separately on each trivariate signal, the MEMD method guarantees the extraction of common rotational modes, as the direct analysis of a hexavariate signal results in matched IMFs (both in number and frequency scale).

4.5.3 Real World EEG Signal Processing via MEMD

In order to demonstrate the advantages of MEMD in multichannel signal processing and its ability to align common frequency modes in same-index IMFs, it was applied to a real world electroencephalography (EEG) signal with an aim to separate the brain electrical activity from unwanted artefacts such as the electrooculogram (EOG) and electromyogram

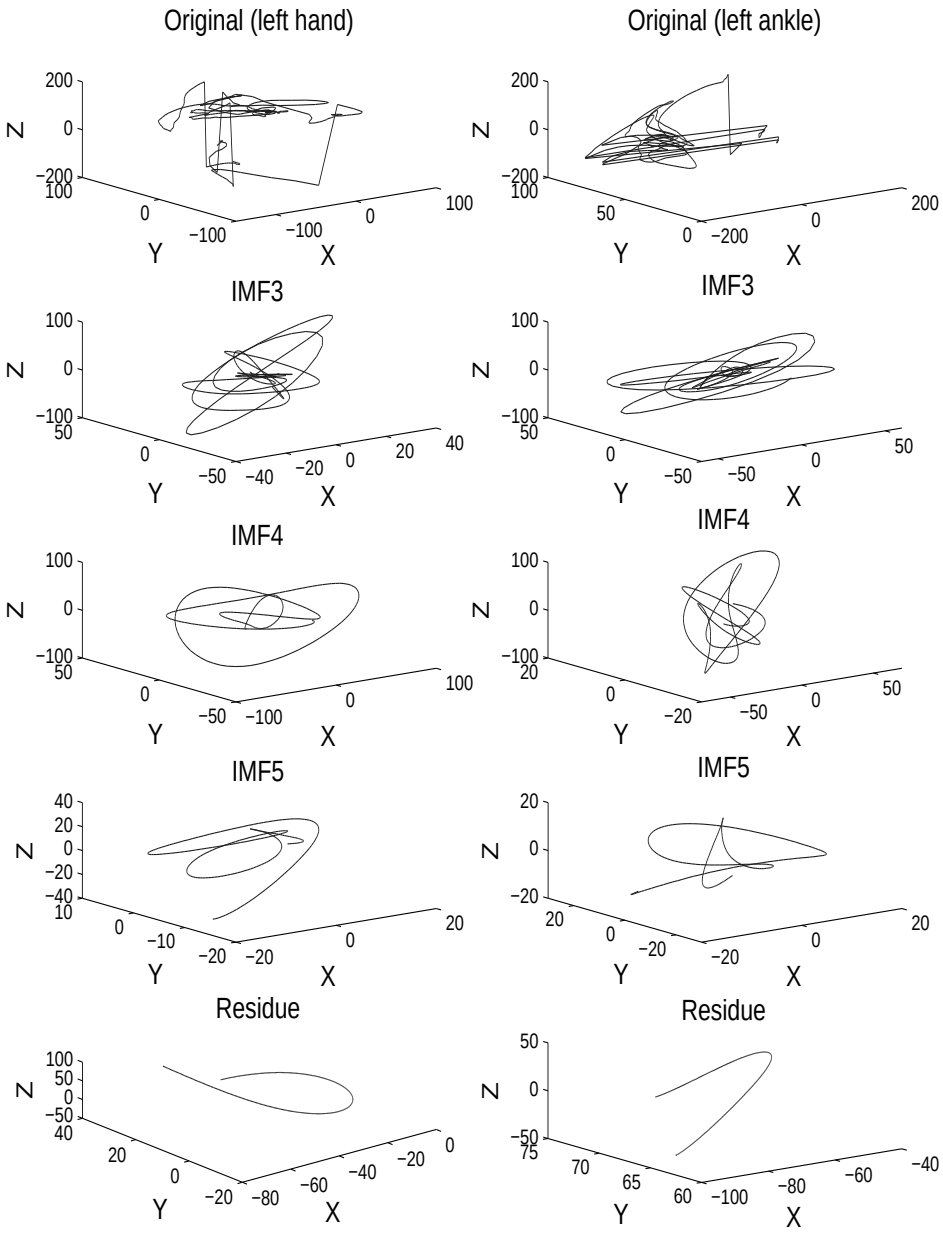

Figure 4.7: A real world hexavariate orientation signal and its decomposition using multivariate EMD algorithm. Trivariate orientation signals corresponding to the left hand movement, and the left ankle movement, are shown in the top row, with selected IMFs below depicting the common rotational modes.

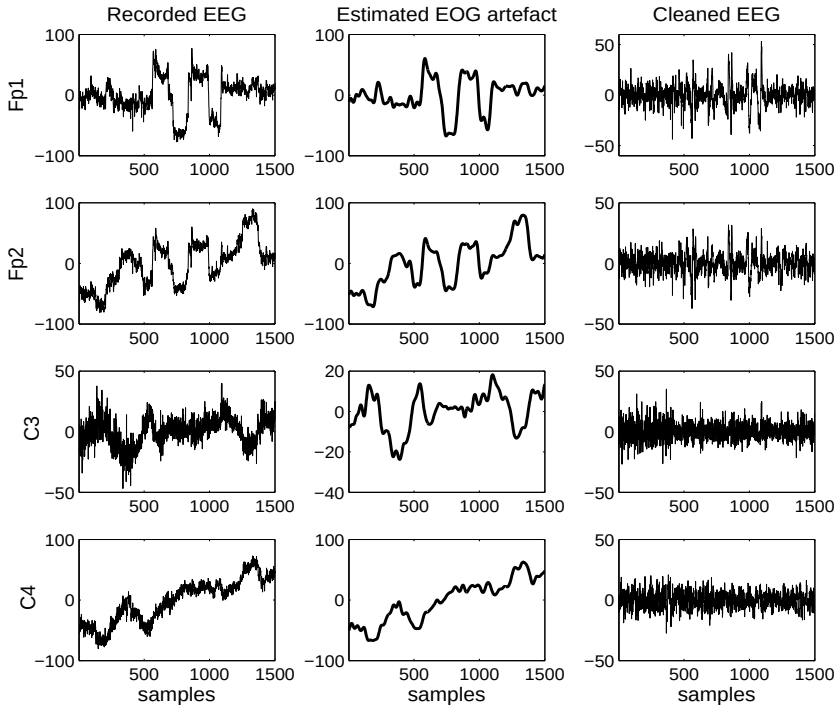

Figure 4.8: Artefact removal from four EEG channels ($Fp1$, $Fp2$, $C3$ and $C4$) using the MEMD algorithm. The estimated eye muscle activity (artefact) has been shown in the middle column, whereas the conditioned EEG signal is presented in the right hand column.

(EMG)[5]. Data used in these simulations were collected from 4 EEG channels ($Fp1$, $Fp2$, $C3$, $C4$), and subjects were asked to move their eyes during the data collection, resulting in the ocular interference in the recorded EEG signal. The four channels were then processed by MEMD.

Owing to the property of MEMD to align IMF frequency sub-bands from different channels, the decomposed EEG data was aligned in such a way that the high frequency neurophysiological signals were contained in the lower-index IMFs, while low frequency electrophysiological signals (EMG and EOG) were present in the higher-index IMFs. A simple threshold on the IMF index was then used to separate non-EEG related interference from the underlying brain activity. The EOG and clean EEG signal estimated this way are

[5]The goal here is to show the potential of MEMD in multivariate signal processing and not to propose any new method for denoising surface EEG data. For advance EMD-based denoising methods, refer to [54] [76].

shown in the middle and right hand column of Figure 4.8, with the original contaminated EEG signals shown in the left hand column. It is important to note that such separation is difficult to achieve by applying univariate EMD to all the channels separately, as this would result in spectrally uncorrelated components. For this purpose, a complex clustering technique was used in the frequency domain in order to identify spatially correlated modes from univariate EMD decompositions [70]. However, as EMD was applied channel-wise, high frequency components were still present in the estimated EOG signal.

4.6 MEMD Studies and Applications

Since its inception, MEMD algorithm has gained popularity in the signal processing community and has been a focus of numerous studies and being employed in several real world applications. The main reason for its popularity is its ability to process multiple channels simultaneously and, in the process, 'aligning' the common frequency modes across the same-indexed IMFs.

Due to the above properties, MEMD has been successfully used for the analysis of electroencephalogram (EEG) signals with an aim to distinguish between ictal and seizure-free intracranial EEG recordings [77]. In [78], an MEMD-based time-varying phase synchrony measure is defined to quantify multivariate synchronization within a network of oscillators; simulations showed that the proposed measure was found to be effective in the case of both chaotic oscillators and real EEG data. Moreover, in [10], the mutual information and multi-information measures are used in connection with MEMD to examine the interdependence between multiple channels of a data set, at multiple temporal scales. In [79], owing to its filterbank property, MEMD has been used to generate multiple aligned scales as a replacement to the coarse graining process in traditional multiscale entropy analysis.

Recently, MEMD has also been combined with adaptive learning based on temporal neural networks to make it robust against the problems associated with the algorithm parameters [80]. The resulting so-called multivariate empirical mode decomposition

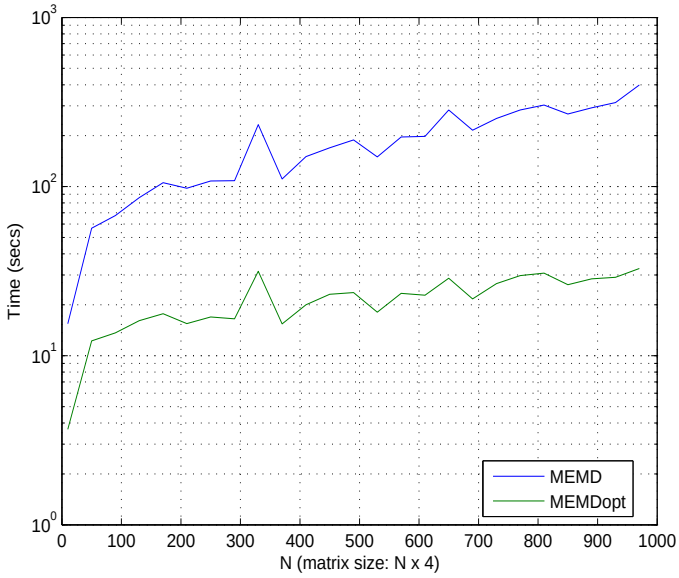

Figure 4.9: Computational requirements of the MEMD algorithm: Time requirements of the MEMD algorithm to process a quadrivariate WGN signal as a function of the input size. Green and blue lines give time requirements of a vectorised and non-vectorised MEMD implementation on Matlab respectively.

multi-channel least mean square (MEMD-MLMS) algorithm has been shown to bypass the problems of mode-mixing and uniqueness experienced in existing univariate EMD algorithm. Finally, an auditory oddball based brain computer interface (BCI) system using MEMD has been designed, which selects the desired features of the input EEG signals yielding improved results [81].

A study of the filter bank property of MEMD on white Gaussian noise (WGN) has been presented in [82]. The resulting dyadic filter bank structure of MEMD on WGN has then been utilised to good effect via a noise-assisted MEMD (N-A MEMD) algorithm, which aims to reduce mode-mixing within multivariate IMFs; the details of the filter bank property of MEMD and its benefits will be illustrated in the next chapter.

EMD-based algorithms, including MEMD, require large computational resources to run. This is one of their disadvantages since it inhibits them to be used for real-time (online) applications. The time requirement to run MEMD algorithm as a function of its input size is shown in Figure 4.9. It gives a comparison of the computational requirements of two different versions of MEMD algorithm in Matlab to process a quadrivariate WGN

signal of zero mean and unit variance. One implementation, shown by the green line in Figure 4.9, preallocates large arrays and uses vectorised code suited to Matlab whereas the other uses non-vectorised code (blue line). The vectorised MEMD implementation is much faster than the non-vectorised one but still takes few minutes to process a large input matrix.

Recently, a computationally light extension of EMD for multivariate signals has been proposed [83] [84], in which the oscillation extremum are derived from a single real-valued function instead of using multiple envelopes of the input signal. Due to this reason, this method is less suitable for signals with large number of input channels, but it is computationally less expensive than MEMD. A comparison between the computational requirements of different MEMD-based algorithms is also given in [83] [84].

4.7 Conclusions

An extension of empirical mode decomposition (EMD) has been proposed to cater for a general class of multivariate signals. The critical step of local mean estimation is performed by taking projections of the multivariate signal along multiple directions in $\mathbb{R}^n$. These directions are generated via low-discrepancy Hammersley point set, giving uniformly distributed direction vectors on $(n-1)$-sphere, and, thus, making the resulting method accurate and computationally efficient. It has been shown that the proposed method has the ability to extract common rotational modes across the signal components, making it suitable for the fusion of information from multiple sources. Simulations on synthetic and real world multivariate data have been presented.

Chapter 5

Multivariate Empirical Mode Decomposition-based Dyadic Filter banks

IN this chapter, a study showing the analysis of multivariate empirical mode decomposition (MEMD) algorithm has been presented for white Gaussian noise (WGN) input. It has been reported that similarly to EMD, MEMD also essentially acts as a quasi-dyadic filter bank on each channel of the multivariate WGN input signal. However, unlike EMD, MEMD better aligns the corresponding intrinsic mode functions (IMFs) from different channels across the same frequency range which is crucial for its real world applications.

5.1 Introduction

Filter banks are a collection of band-pass filters designed to isolate different frequency bands in the input signal. The analysis of standard EMD for the case of input white Gaussian noise (WGN) and fractional Gaussian noise (fGn) has revealed that IMFs tend to mimic a dyadic filter bank structure, similar to that observed in the case of wavelet decompositions [26] [52]. This is shown in Figure 5.1, where the estimated IMF power spectra are plotted for the input WGN. It can be noticed that the behaviour of first IMF

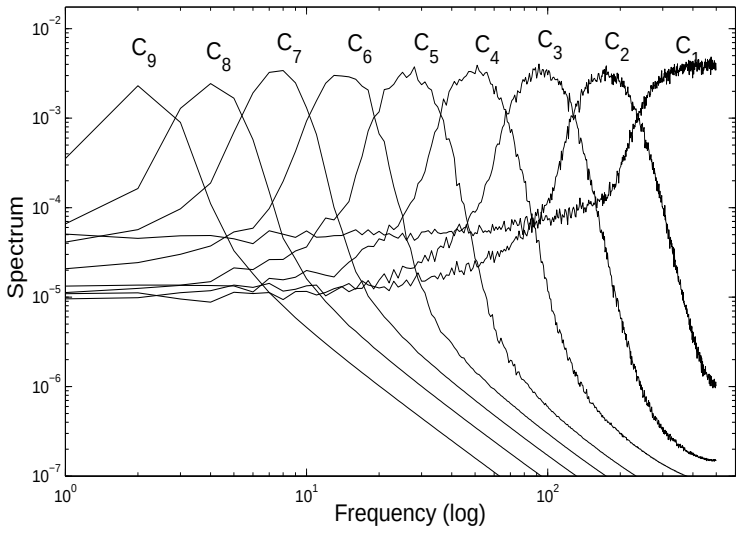

Figure 5.1: Power spectra of first nine IMFs $(c_1,\ c_2, \ldots, c_9)$**, obtained by applying EMD to white Gaussian noise, is plotted as a function of the logarithm of the frequency. The quasi-dyadic filter bank structure observed by IMF spectra is quite evident.**

is different from other modes: it essentially acts as a high pass filter, whereas, higher indexed IMFs act similarly to a band-pass filters, with their spectra appearing nearly the same, with some shifts along the frequency axis. These results are quite reminiscent of the findings made in the case of wavelet-based decompositions for WGN [4] [38].

The multivariate empirical mode decomposition (MEMD) algorithm is the first generic extension of standard EMD for multivariate data which has been shown to perform well in deterministic settings involving synthetic sinusoidal signals [18]. However, for its real world applications, it is also important to investigate how it behaves in the presence of multichannel fGn and WGN, and is the main aim of this chapter. To this end, a study of MEMD equivalent filter banks for WGN is presented. This is followed by the investigation of the scaling and self-similar properties observed by MEMD-based filter banks.

5.2 MEMD Analysis of Broadband Noise

In this section, the chracterization of MEMD algorithm is carried out based on its response to input multivariate broadband noise. For this purpose, a comprehensive set of

simulations were performed by applying MEMD algorithm to a generalised broadband fractional Gaussian noise (fGn), and the spectra of the corresponding intrinsic mode functions (IMFs) were studied.

5.2.1 Fractional Gaussian Noise

A fractional Gaussian noise (fGn) can be seen as an incremental process of a fractional Brownian motion (fBm); fBm is a continuous time Gaussian process depending entirely on its second order properties and a so-called Hurst parameter $0 < H < 1$. It is a generalization of the ordinary Brownian motion for $H = 0.5$ whose derivative is white noise. Hence, fGn can be considered as a generalization of white noise. More specifically, $\{x_H(k),\ k = \cdots -1, 0, 1 \ldots\}$ is a fGn of index H (with $0 < H < 1$) if and only if it is a zero-mean Gaussian stationary process with autocorrelation sequence, which is given by

$$r_H(k) = \frac{\sigma^2}{2}\big(|k-1|^{2H} - 2|k|^{2H} + |k+1|^{2H}\big). \tag{5.1}$$

It is well understood that the sequence $x_H(k)$ for $H = 0.5$ corresponds to white noise, whereas, it exhibits negative correlations for $0 < H < 0.5$ and positive correlations for $0.5 < H < 1$. By taking the Fourier transform of equation (5.1), the power spectral density (PSD) of fGn is obtained, which can be written as

$$S_H(f) = K\sigma^2|e^{i2\pi f} - 1|^2 \sum_{k=-\infty}^{\infty} \frac{1}{|f+k|^{2H+1}}. \tag{5.2}$$

with $f \leq 0.5$. In the limiting case of $f \to 0$, and $H \neq 0.5$, the PSD can be written as $S_H(f) \approx K\sigma^2|f|^{1-2H}$, showing that fGn can be used as a model of power law spectra at low frequencies. In addition, for $0 < H < 0.5$ (short-range correlations), we have $S_H(0) = 0$, and the spectrum is effectively high-pass, while for $0.5 < H < 1$ (long-range correlations), we have $S_H(0) = \infty$. In both cases, the power law form of the spectrum is approximately held and, in log-log coordinates, we have a quasi-linear relation which is given by

$$\log S_H(f) = (1-2H)\log f + C. \tag{5.3}$$

5.2.2 MEMD-based Filter Banks for Multivariate WGN

In this section, it is investigated whether the dyadic filter bank structure is preserved by MEMD for multichannel WGN. It is worth emphasizing that the idea of a filter bank for multivariate inputs, in a strict sense, is still ambiguous since the concept of frequency is not clearly defined for multivariate signals. However, even if the frequency response of individual channels of a multivariate signal are considered, the dyadic filter bank structure imposes an additional constraint on the frequency output of each multivariate IMF– *overlapping of the filter bands associated with the corresponding (same-index) IMFs from multiple channels*. This is vital for the IMFs obtained from MEMD to be physically meaningful, as any mismatch in frequency contents of the corresponding multichannel IMFs would render their correlation or subsequent fusion applications meaningless.

To perform the spectral analysis of MEMD, extensive simulations were carried out on multiple realizations of 8 channel WGN process, which can be considered as a special case of fGn, for $H = 0.5$. In simulations, $N = 500$ WGN realizations were used, each of length $K = 1000$, which were then ensemble averaged to yield an averaged power spectra. The stopping criterion used for MEMD is given in [46], with the value of $S = 5$. While the number of IMFs varied for different input realizations, it never got less than 9 IMFs and, thus, first 9 IMFs have been considered in the following analysis.

In the first case, the frequency response and the corresponding quasi-dyadic filter bank property of MEMD are illustrated by applying MEMD on a single realization of an 8 channel WGN; the power spectra of its resulting first 9 IMFs are plotted in the top of Figure 5.2. Next, the same 8 noise channels were separately processed via standard EMD and the estimated power spectra of its IMFs are shown in the lower half of Figure 5.2. It can be seen that the overlapping of frequency bands of same-index IMFs, associated with different channels, is more prominent in the case of MEMD as compared to standard EMD. This alignment of IMF-based frequency bands for a single noise realization, in the case of MEMD, results in the stabilization of the shape of individual spectra and allows for the estimation of these spectra using fewer noise realizations.

Next, the average spectra of IMFs obtained from $N = 500$ realizations of WGN are

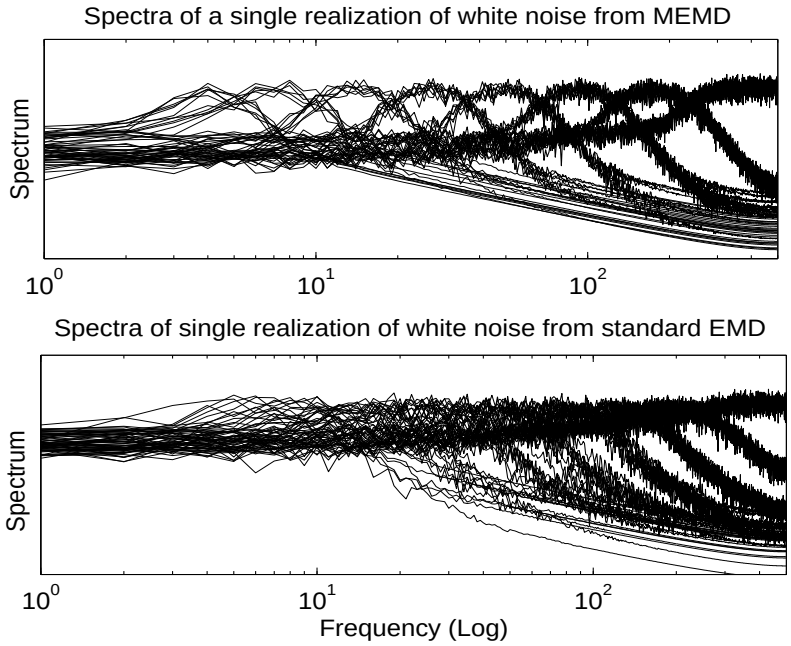

Figure 5.2: Spectra of IMFs $(c_1, c_2, \ldots, c_9)$ obtained for a single realization of an 8-channel white Gaussian noise via MEMD (top) and the standard EMD (bottom). Overlapping of the frequency bands corresponding to the same-index IMFs is more prominent in the case of MEMD-based filters.

plotted in Figure 5.3, both for standard EMD (lower half) and multivariate EMD (top row). It is evident from Figure 5.3 that for a given number of noise realizations N, standard EMD failed to properly align the band-pass filters associated with the corresponding IMFs from different noise channels. Although this alignment is expected to become better with an increase in the number of noise realizations, MEMD-based spectra achieved much better results with same number of ensembles.

A quantitative evaluation of the mode-alignment observed in the case of MEMD-based filter banks is shown in Figure 5.4, where the normalised cross-correlation measure between IMFs obtained from MEMD and standard EMD, applied on bivariate WGN, are plotted. In simulation, $N = 500$ bivariate WGN realizations were used, each of length $K = 1000$. The cross-correlation measure $\Upsilon(m, m')$ can be given by

$$\Upsilon(m, m') = \left| \frac{1}{N} \sum_{j=1}^{N} \frac{\Upsilon^j(m, m')}{\sqrt{\Upsilon^j(m, m)\Upsilon^j(m', m')}} \right| \tag{5.4}$$

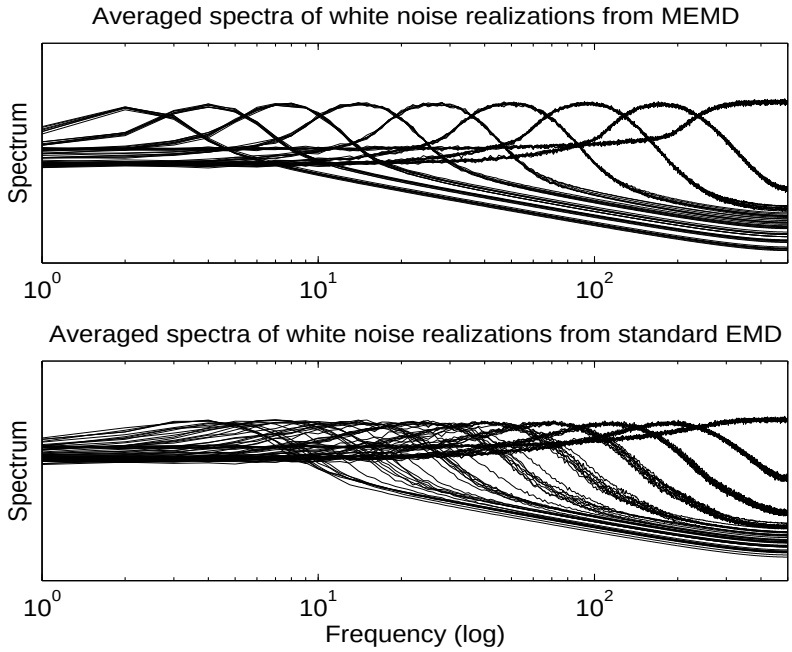

Figure 5.3: Averaged spectra of IMFs obtained for $N = 500$ realizations of 8-channel white Gaussian noise via MEMD (top) and the standard EMD (bottom). Overlapping of the frequency bands corresponding to the same-index IMFs is improved in both cases after averaging, but MEMD bands show much better alignment.

where

$$\Upsilon^j(m, m') = \frac{1}{K} \sum_{k=1}^{K} c_m^j(k) c_{m'}^j(k) \tag{5.5}$$

where $c_m^j(k)$ is the mth IMF of jth noise ensemble.

It can be observed that due to significant overlapping of the spectra of corresponding (same-indexed) IMFs, from multiple channels, obtained from MEMD, the cross-correlation measure given in equation 5.4 has comparatively larger values along the diagonal ($m = m'$), in Figure 5.4(left). In EMD-based decomposition, however, higher values of cross-correlation estimates are even observed for ($m \neq m'$), yielding miss-aligned IMFs, as shown in the right hand side of Figure 5.4.

Since the number of zero crossings in an IMF is directly related to the number of oscillations, a rough indicator of the frequency content within the signal, it is possible to

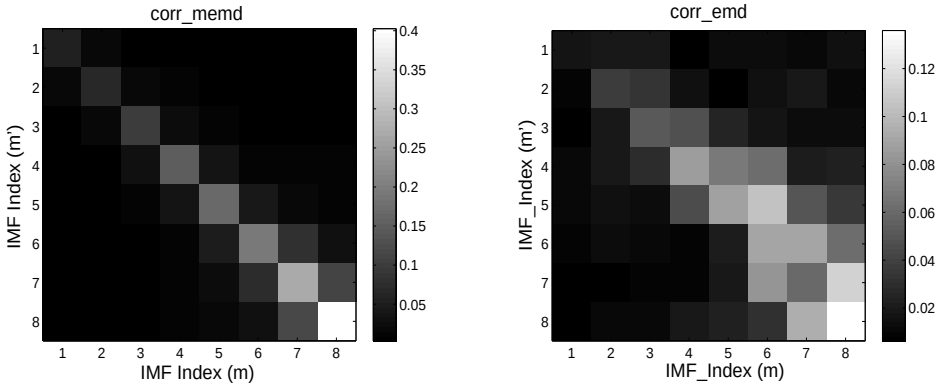

Figure 5.4: The schematic of the normalized IMF cross-correlation, given in equation (5.4), from multiple channels obtained via MEMD (left) and EMD channel-wise (right). The distribution of higher values of the cross-correlation measure along the diagonal line in the case of MEMD (left column) indicates the mode-alignment between IMFs from multiple channels. The IMF indices grow from left to right and from top to the bottom.

analyse the nature of MEMD as a quasi-dyadic filter bank with respect to the IMF index. For standard EMD, it was shown in [26] and [52] that the IMFs followed the structure of a quasi-dyadic filter with the linear (slope close to -1) relationship between the logarithm of number of zero crossings and the IMF index.

Figure 5.5(top) shows that the same analysis for IMFs obtained via MEMD revealed similar results to those obtained for standard EMD, with the slope of approximately -0.92 for all the 8 channels, indicating a quasi-dyadic filter bank nature of MEMD for white noise.

Another important property of quasi-dyadic filter bank structure, obtained from standard EMD, is the self-similarity of its constituent band-pass filters [26]. To illustrate that the IMFs of individual channels obtained from MEMD also exhibit this self-similar behaviour, let $S_m(f)$ denote the frequency response of the mth IMF. Then due to the similarity between different IMF based band-pass filters, the frequency response of m'th IMF can be described by

$$S_{m'}(f) = S_m(\gamma^{m'-m} f) \tag{5.6}$$

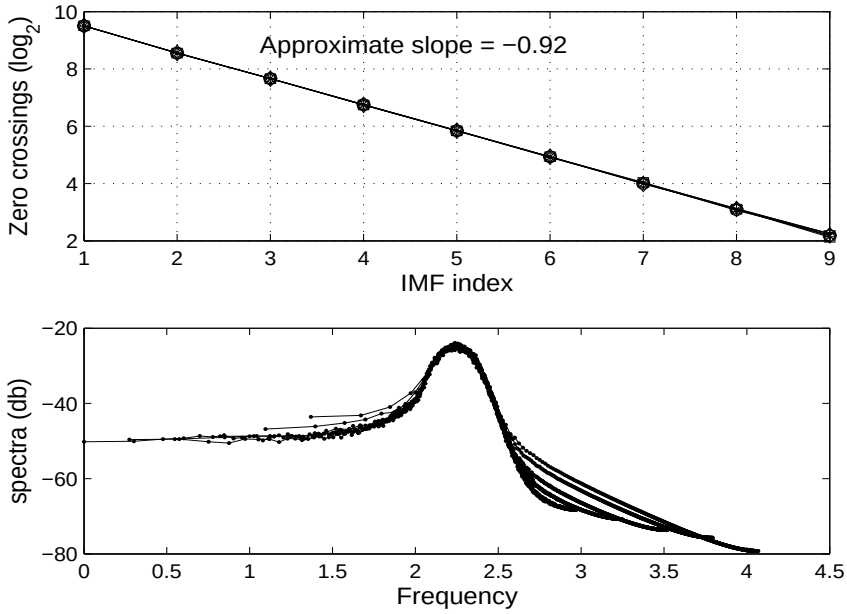

Figure 5.5: MEMD as a quasi-dyadic filter bank. Top: Average number of zero crossings plotted vs the IMF index for all 8 channels. The slope of -0.92 indicates similarity to a dyadic filter (with slope -1). Bottom: Fourier spectra of IMFs from MEMD with $(c_3, \ldots, c_9)$ shifted to the right hand side, overlapping the spectrum associated with c_2.

where $m' > m \geq 2$. Parameter γ can be calculated from the slope of the straight line between the number of zero crossings and the IMF index; for a fully dyadic filter bank, its value is 2. Using the normalized equation (5.6), spectra of all IMFs ($m' > 2$) obtained from MEMD collapsed to a single curve as shown in Figure 5.5(bottom).

This shows that the IMFs obtained by MEMD follow the quasi-dyadic filter bank structure similar to the IMFs from standard EMD, facilitating its applications based on vector sensors and in data fusion.

5.2.3 MEMD-based Mode-Alignment for Multivariate fGn

Next, simulations were carried out on multiple realizations of 8 channel fGn process generated for different values of the Hurst exponent, $H = 0.1, 0, 2, \ldots, 0.9$. All other settings were similar to those used in MEMD-based WGN filters.

The resulting IMF spectra are plotted in Figure 5.6 for different values of H; it is

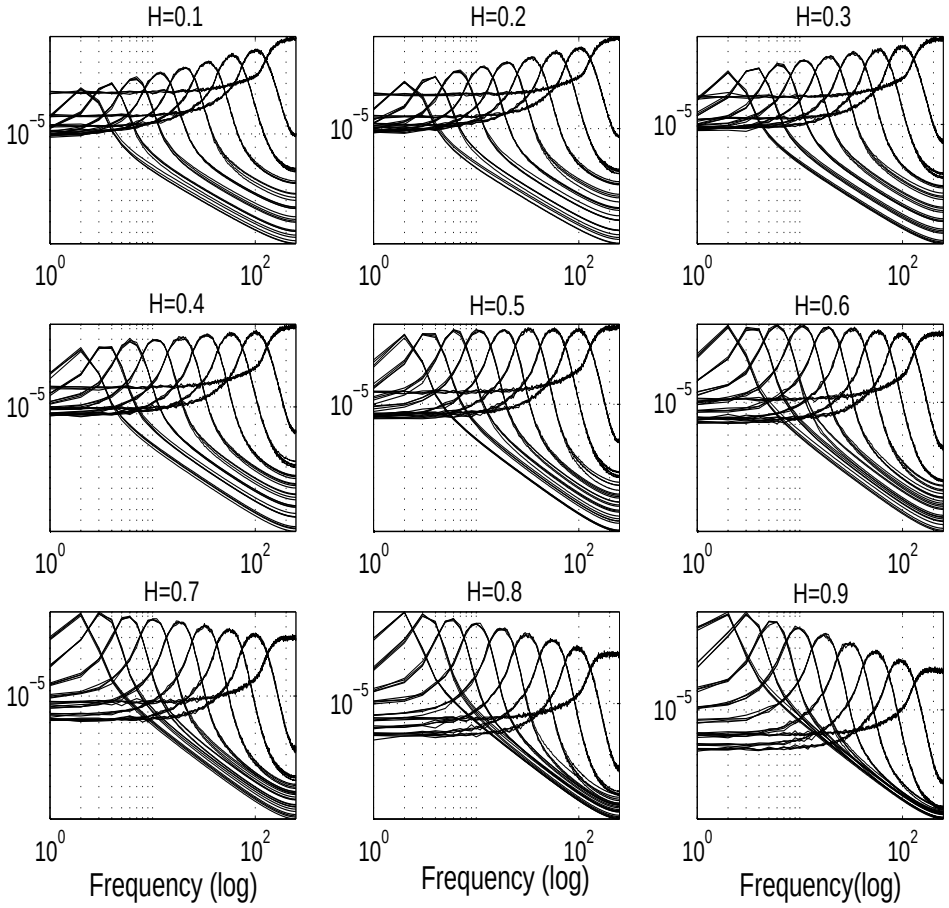

Figure 5.6: Power spectra of multivariate IMFs in the case of fractional Gaussian noise (fGn). The estimated power spectrum densities are plotted against the logarithm of the frequency, for the first 9 IMFs, for different values of the Hurst exponent $H = 0.1, 0, 2, \ldots, 0.9$. Overlapping of the frequency bands corresponding to the same-index IMFs is clearly visible in all cases rendering MEMD an improved mode-alignment property.

evident that the mode-alignment property of the multivariate IMFs which was observed in the case of WGN is also held for fGn. Moreover, it can be noted that as H varies from 0 to 1, the spectrum of the last IMF c_9 changes from band-pass to increasingly low-pass, in accordance with the increasing predominance of low frequencies.

5.3 Conclusions

It has been shown that the multivariate empirical mode decomposition (MEMD) algorithm follows a filter bank structure (channel-wise) for multivariate white Gaussian noise (WGN) inputs. MEMD-based filters have also been shown to align similar modes present across multiple channels in same-index IMFs, both for WGN and fGn inputs, which is hard to achieve by applying standard EMD channel-wise.

Chapter 6

Noise-Assisted Multivariate Empirical Mode Decomposition

BASED on the dyadic filter bank property of MEMD for multivariate white Gaussian noise (WGN), a noise-assisted multivariate empirical mode decomposition algorithm is presented. The method aims to provide a better decomposition as compared to the standard EMD algorithm by reducing its inherent mode-mixing problem; the performance of the proposed method is also compared with the well established ensemble empirical mode decomposition (EEMD) algorithm.

6.1 A Review of Noise-Aided EMD Algorithms

In this section, a quick review of the recent algorithms have been reported which make use of the dyadic filter bank property observed by EMD, for WGN, in order to solve some inherent problems in standard EMD algorithm.

One such notable problem of EMD is the decomposition of a class of signals which lack necessary number of extrema, e.g. dirac pulse (delta function), since its operation depends heavily on the existence of extrema. In the extreme case of dirac pulse (containing a single extremum), Flandrin *et al.* proposed adding multiple realizations of noise to such a signal first, as a pre-whitening step, and then applying EMD to the resulting

ensemble [39] [53]; the mean of the ensemble was then taken as the final output. Clearly, in this case, the addition of noise to the dirac pulse can greatly facilitate the EMD process due to the added extrema.

In the same spirit, Gledhill used an ensemble of original input signal and noise to check the robustness of EMD algorithm against noise [55]. Though, he never employed the idea of taking ensemble mean as the final output, he did define the composite Hilbert spectrum based on the ensemble mean of the noise added analysis. However, due to the non-negativity of the spectrum, the added noise could not cancel out and he, therefore, had to limit the noise level to infinitesimal values to make their contribution negligible.

Another area where noise-aided analysis has been greatly beneficial in EMD is to reduce its inherent mode-mixing problem. Mode-mixing is characterized by having multiple modes in a single IMF or a single mode or scale distributed across more than one IMFs. It clearly compromises the physical significance of EMD-based decomposition and limits its use in several real world applications [25] [23]. Mode-mixing is mainly caused due to significant overlapping of the frequency responses of multiple IMFs; this problem was addressed by Wu *et al.* by making use of the dyadic filter bank structure of EMD for WGN [26] [52] [53]. In their proposed algorithm, known as ensemble EMD (EEMD) [31], multiple realizations of WGN are combined with the original signal to form an ensemble, over which EMD algorithm is run. The mean of the ensemble is then taken as the final output. Multiple realizations of WGN are considered to average out the effects of white noise. However, despite the averaging, the reconstructed signal still includes the residual noise and different realizations of signal plus noise yield different number of IMFs.

Recently, a couple of advancements in the EEMD algorithm have been proposed; one such algorithm adds a particular noise at each decomposition stage and computes a unique residual to obtain an IMF [56]. Another, named complementary ensemble empirical mode decomposition (CEEMD), removes the residual of added white noise in EEMD via pairs of complementary ensemble IMFs obtained from positive and negative added noise to the signal [85]. In this chapter, however, EEMD algorithm has been considered for analysis and comparison with the method proposed in this chapter because of its popularity in the

signal processing community.

6.2 Ensemble Empirical Mode Decomposition

The ensemble empirical mode decomposition (EEMD) algorithm is a noise-aided EMD analysis, which was originally designed to overcome the frequently occurring mode-mixing problem in standard EMD. Before describing the details of EEMD algorithm, the mode-mixing problem is first explored in the next section.

6.2.1 Mode-Mixing in EMD

Mode-mixing is mainly characterized by a situation where a single IMF either carries signals of widely disparate scales, or a single mode or scale resides in more than one IMF components. It is mainly caused by signal intermittency and results in the overlapping of IMF spectra and aliasing in the time-frequency (TF) domain. The mode-mixing seriously compromises the physical meaning of IMFs by wrongly suggesting that there might be different physical processes represented in a single IMF or a single process. It was first detected by Huang *et al.* in [31] where the modeled data was a mixture of intermittent high frequency oscillations modulated on a low frequency tone; A similar example is presented here for illustration:

The synthetic data and its sifting process are shown in the top row of Figure 6.1; the signal consists of a low frequency tone, with another high frequency and low amplitude tone riding on its selected crests (around time index 4000, 6000, and 8000). Due to the maxima (minima) introduced by the high frequency intermittent wave, the estimates of upper and the lower envelopes are inaccurate and the resulting local mean signal (thick dotted line in the top panel of Figure 6.1) does not reflect the true dynamics of the signal. Consequently, the estimate of the first IMF is a combination of both the low frequency tone and high frequency intermittent waves, resulting in the mode-mixing problem. This is shown in the lower panel of Figure 6.1, which gives the decomposition of the synthetic signal via standard EMD.

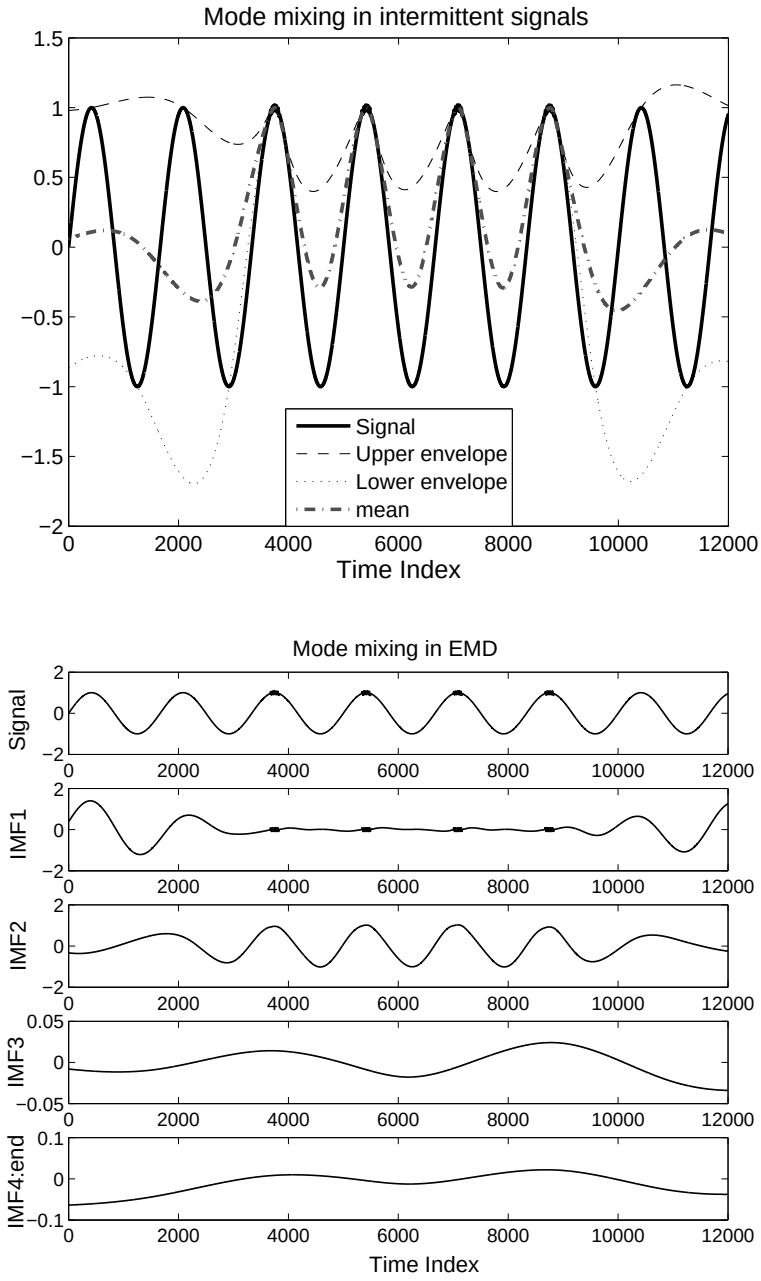

Figure 6.1: Mode-mixing in standard EMD: (top) Sifting process illustrating the mode-mixing phenomenon in a synthetic signal. The presence of the intermittent high frequency tone at the crests, at around time index 4000, 6000, and 8000, results in inaccurate local mean estimation due to discrepancy in the calculation of upper and lower envelopes. (bottom) Decomposition of the signal via standard EMD; mode-mixing is evident, since the first IMF contains both the low frequency tone and the intermittent high frequency riding wave.

To overcome this problem, Huang *et al.* proposed an intermittence test which aimed to identify oscillations with significantly higher frequencies in the input, as compared to an a priori chosen reference frequency value [86]. Another method based on the similar principle pre-treated the original data using wavelet transform to avoid the mode mixture in the subsequent empirical mode decomposition [87]. While these methods performed well for certain synthetic signals, choosing a priori value of reference frequency (period) was always going to be impractical for real world signals; consequently, these methods were not widely adopted.

6.2.2 Ensemble EMD Algorithm

The Ensemble EMD (EEMD) algorithm makes use of the dyadic filter bank property of EMD on white Gaussian noise (WGN) by populating the whole time-frequency (TF) space. This is achieved by adding multiple realizations of WGN to the input signal to form an ensemble, over which EMD is run. The mean of the corresponding IMFs is then taken as the final output of EEMD. More specifically, if $x(t)$ denotes the input signal, and $w_n(t)$ the nth realization of WGN, then the ensemble of signal and WGN can be expressed as

$$\{s_n(t)\}_{n=1}^{N} = x(t) + \{w_n(t)\}_{n=1}^{N} \tag{6.1}$$

for $1 \leq n \leq N$, where N is the total number of ensembles used in the process. The EEMD algorithm is described in Algorithm 5.

Algorithm 5 Ensemble Empirical Mode Decomposition

1: Generate $s_n(t) = x(t) + w_n(t)$ for $n = 1, \ldots, N$; $w_n(t)$ $(n = 1, \ldots, N)$ are N different realizations of WGN;

2: Fully decompose $s_n(t)$ $(n = 1, \ldots, N)$ by applying standard EMD to each realisation $s_n(t)$ separately, obtaining M IMFs for $s_n(t)$, denoted by $\{c_m^n(t)\}_{m=1}^{M}$;

3: Average the corresponding IMFs from the whole ensemble to obtain the averaged IMFs; for instance, mth IMF can be obtained by using $\bar{c}_m(t) = \frac{1}{N}\sum_{n=1}^{N} c_m^n(t)$;

The effect of added WGN series should cancel while taking the mean over a sufficient ensemble in accordance with the following well established rule:

$$\gamma_n = \frac{\eta}{\sqrt{N}} \tag{6.2}$$

where η is the amplitude of the added noise, and γ_n is the standard deviation of the error signal between the final output from EEMD and the original signal $x(t)$.

The relation given by equation (6.2) highlights a significant drawback in EEMD: To completely cancel the effect of added noise from the final output, in other words to ensure full completeness of EEMD method, an infinite number of ensembles must be considered. In practical scenarios, however, a sufficiently large value of N is taken so as to reduce the corresponding error power (standard deviation) between the EEMD output and the original input signal to an acceptable level.

To illustrate the benefits of EEMD in terms of reducing the mode-mixing phenomenon, it was applied to the data set shown in Figure 6.1. The power of the added noise was chosen to be 0.05 as compared to the original data, and $N = 50$ number of ensembles were considered. The decomposition achieved by EEMD is shown in Figure 6.2. It is clear that the low frequency primary component was completely extracted in IMF6, whereas, the high frequency intermittent signal was decomposed in IMF4 and IMF5. The first three IMFs contained the residual noise due to added WGN; its contribution, however, could be reduced by increasing the ensemble size N in accordance with the relation given in equation (6.2).

6.3 Noise-Assisted MEMD

In the last section, it was shown that while ensemble EMD (EEMD) can significantly reduce the mode-mixing phenomena, it compromises the 'completeness' of the reconstructed signal since it adds the realizations of white Gaussian noise (WGN) directly to the input signal, giving rise to the residual noise in the final output. Moreover, the output components obtained from EEMD, after taking the mean of IMFs over all realizations, do not

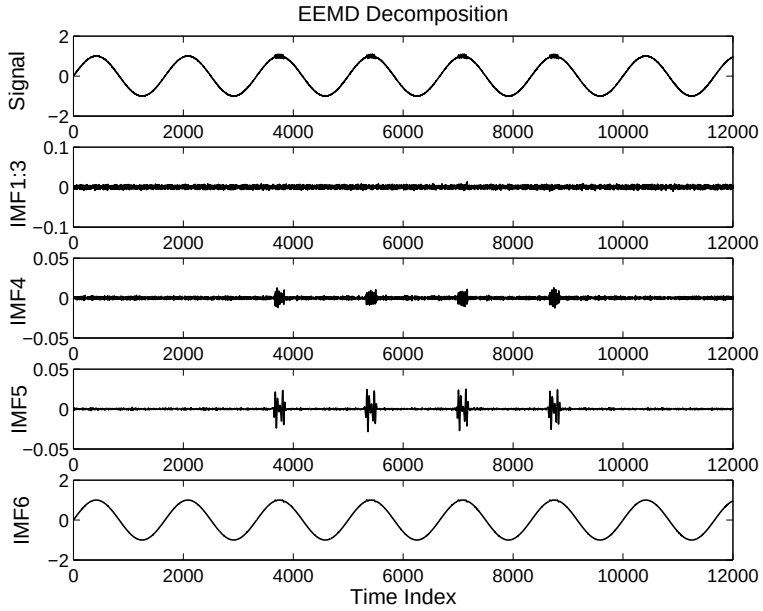

Figure 6.2: Decomposition of the signal in Figure 6.1 via ensemble EMD; it has been shown that the low frequency tone and the intermittent high frequency riding wave have been separated accurately using EEMD.

strictly conform to the definition of an IMF.

To overcome these problems, a more suitable approach would be to somehow separate noise from the input signal while still using the dyadic filter bank property of EMD on WGN. Fortunately, the emergence of multivariate empirical mode decomposition (MEMD) algorithm and the fact that its decomposed components exhibit a dyadic filter bank structure for WGN both provide necessary tools to do so.

Based on the above idea, a noise-assisted MEMD (N-A MEMD) algorithm is presented which adds extra channels containing multivariate independent white Gaussian noise to the original multivariate signal, and then process such a composite signal via MEMD. Adding extra noise channels gives the desired separation between the input signal and the added noise, while still enforcing the dyadic filter bank structure on the input signal. Next, the IMF channels corresponding to white noise are discarded yielding a set of IMFs associated with only the original input signal. The details of the N-A MEMD method are outlined in Algorithm 6.

Since added noise channels occupy a broad range in the frequency spectrum, MEMD

Algorithm 6 Noise-Assisted MEMD

1: Create an uncorrelated Gaussian white noise time series (l-channel) of the same length as that of the input, with $l \geq 1$;

2: Add the noise channels (l-channel) created in step 1 to the input multivariate (n-channel) signal $n \geq 1$, obtaining an $(n + l)$-channel multivariate signal;

3: Process the resulting $(n + l)$-channel multivariate signal $n + l \geq 2$ using MEMD algorithm, to obtain multivariate IMFs;

4: From the resulting $(n + l)$-variate IMFs, discard the l channels corresponding to the noise, giving a set of n-channel IMFs corresponding to the original signal.

aligns its different components (IMFs) in accordance with the quasi-dyadic filter bank structure, with each component carrying a frequency subband of the original signal. In doing so, IMFs corresponding to the original input signal also align themselves according to the structure of a quasi-dyadic filter bank[1]; this, in turn, helps to reduce the mode-mixing problem within the extracted IMFs.

Note that while the basic principle behind N-A MEMD method is similar to that of EEMD: enforcing the quasi-dyadic filter bank structure on the input signal, it operates more effectively by separating the noise from the input signal via MEMD algorithm. Consequently, N-A MEMD overcomes the inherent flaws of EEMD algorithm, including residual noise in the reconstructed signal and the deviation from strict IMF definition. Moreover, unlike EEMD, N-A MEMD algorithm can inherently process multivariate data, as it employs MEMD. A more detailed comparison between the two methods will be presented later in the chapter.

6.3.1 Simulations

To illustrate the benefits of N-A MEMD in terms of reducing mode-mixing in univariate signals and also mode-misalignment in multivariate signals, simulations were performed on

[1]The effect of adding WGN channels on the spectrum of the original signal is illustrated via a synthetic simulation in the next section

synthetic signals consisting of a combination of several tones. In both sets of simulations presented here, two added noise channels, $l = 2$, were chosen and the noise power was taken as 0.05, corresponding to the SNR of 13 db. The number of directions used in the MEMD algorithm[2] were $V = 512$ and the parameters of the stopping criterion used were $[\theta_1 = 0.05,\ \theta_2 = 0.5,\ \alpha = 0.05]$ and $S = 1$.

Mode-Mixing in Univariate Signals

This simulation was conducted to show the ability of N-A MEMD to reduce mode-mixing in univariate signals. For this purpose, a synthetic signal consisting of a combination of three different tones was chosen; two low frequency tones (0.23 Hz and 1.0 Hz) were added together along with a high frequency sinusoid (2 Hz) added between samples 1000 and 1650. The resulting signal and its decomposition obtained from standard EMD are shown in Figure 6.3(a). Mode-mixing is evident since IMF1 contains multiple modes. Moreover, mode-mixing can also be seen in IMF2 and IMF3.

The same signal was next processed using the N-A MEMD method with two extra noise channels ($l = 2$). The IMFs from the resulting trivariate signal are shown in Figure 6.3(b). Observe that the IMFs corresponding to the first channel are now free of mode-mixing, as all the tones are decomposed as separate IMFs (IMF4, IMF5, and IMF6).

To analyse the effects of adding noise channels to the original synthetic signal, the spectra of IMFs obtained from standard EMD and N-A MEMD are plotted in Figure 6.3(c) and Figure 6.3(d), respectively. It can be noticed that in the case of standard EMD, the spectra of IMF1-IMF2 and IMF2-IMF3 overlap with each other, resulting in mode-mixing in the time domain, as evident in Figure 6.3(a). On the other hand, power spectra of IMFs obtained from N-A MEMD are well separated in the frequency domain due to the quasi-dyadic filter bank structure imposed by added WGN channels; the resulting decomposition in the time domain, therefore, does not suffer from the mode-mixing problem (Figure 6.3(b)).

[2]The simulations were performed in Matlab using the MEMD toolbox provided at: http://www.commsp.ee.ic.ac.uk/∼mandic/research/emd.htm.

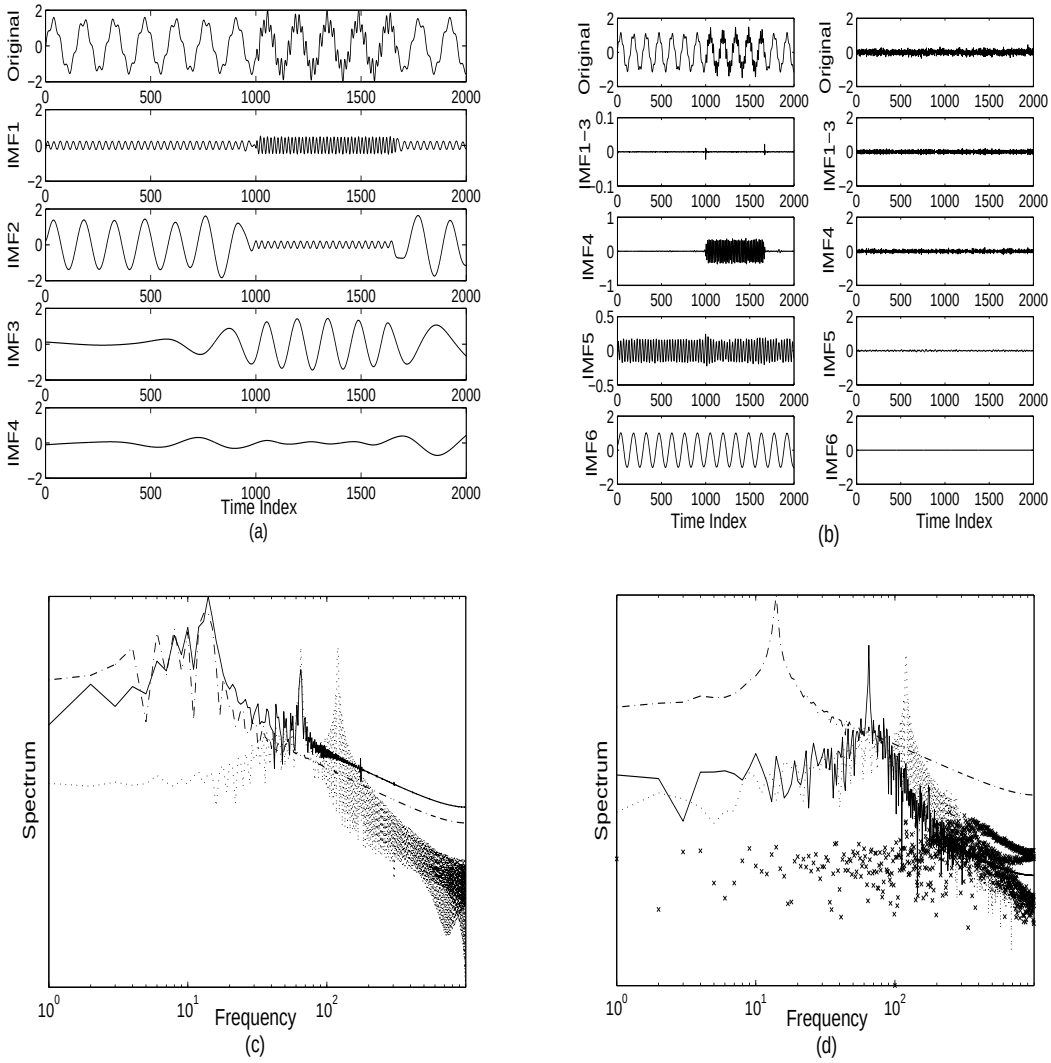

Figure 6.3: N-A MEMD for reducing mode-mixing: (a) IMFs of a synthetic signal obtained by applying standard EMD. (b) IMFs of a synthetic signal obtained by applying the N-A MEMD (left hand column); IMFs of one of the two noise channels (right column). (c) Spectrum of IMFs obtained from standard EMD. Mode-mixing is evident due to overlapping of spectra from IMF1 and IMF2; and IMF2 and IMF3. (d) Spectrum of IMFs obtained from N-A MEMD; due to the added noise channels, the spectrum of the IMFs from the original signal do not overlap, in turn, reducing mode-mixing. (See text for more detail).

Mode-Misalignment in Bivariate Signals

Simulations were also performed on a synthetic bivariate signal to show that the introduction of noise in N-A MEMD method also reduces the so-called 'mode-misalignment' in multivariate extensions of EMD. The bivariate (complex) data used in the simulation

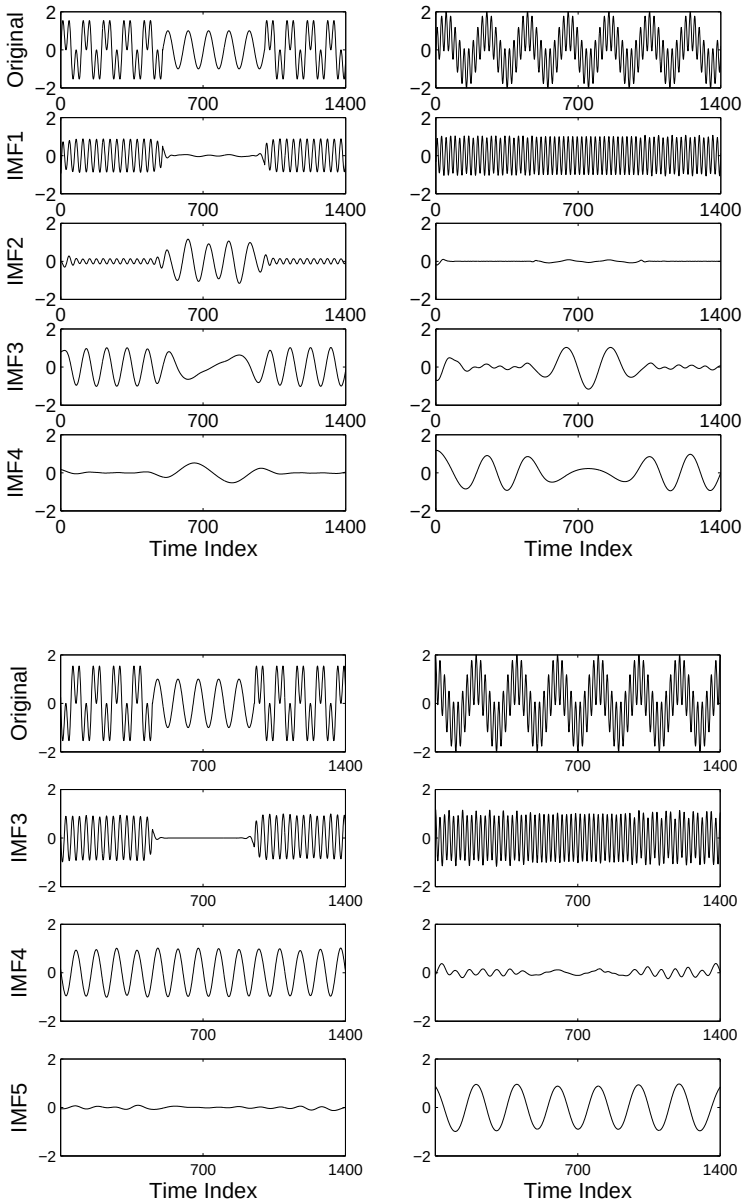

Figure 6.4: N-A MEMD for reducing mode-misalignment in multivariate data: (top) Decomposition of a synthetic bivariate tone signal using the bivariate EMD algorithm. Mode-mixing and mode-misalignment are evident across all but the IMF1. Simulations with different parameters for the stopping criterion yielded similar results. (bottom) Decomposition of a synthetic bivariate tone signal via N-A MEMD for $l = 2$. Both the problems of mode-mixing and mode-misalignment are clearly reduced. Again, the obtained results were generally found robust to changes in the MEMD parameters.

consisted of a real part which was a combination of a tone of 1 KHz and a tone of 3 KHz just added at the beginning and end of the signal, whereas, the imaginary part was a summation of two tones with frequencies of 0.75 KHz and 3 KHz.

Mode-alignment refers to the generation of similar frequency modes across same-index IMFs in multiple channels, and is one of the characteristics of multivariate extensions of EMD [18]. However, in addition to mode-mixing within IMFs of a single channel, mode-mixing also occurs within the same-indexed IMFs across multiple channels (mode-misalignment). This is illustrated in the top half of Figure 6.4, which shows the decomposition of a synthetically generated bivariate tone signal via bivariate extension of EMD [22]. While the highest frequency mode was correctly decomposed as IMF1, both mode-mixing in a single channel and mode-misalignment across multiple channels are evident in the remaining IMFs; a single frequency mode was shared in both IMF2 and IMF3 in the first channel and also in IMF3 and IMF4 in the second channel (mode-mixing). Moreover, different frequency modes can be seen across different channels in IMF3 (mode-misalignment).

The lower half of Figure 6.4 shows the decomposition of the same bivariate signal obtained by the proposed N-A MEMD method, with two extra channels of white noise[3]. It can be seen that both mode-mixing and mode-misalignment are significantly reduced in this case, with each IMF carrying only a single frequency mode, and no instance of different modes across same-index IMFs of different channels. This was expected because the quasi-dyadic structure enforced by the addition of noisy channels in N-A MEMD resulted in the alignment of frequency subbands from different channels of a multivariate signal, in turn, yielding 'aligned' IMFs in terms of their frequency contents.

6.4 N-A MEMD vs EEMD

Unlike EEMD, noise is not added directly to the input signal in N-A MEMD, but instead is kept in separate channels of a multivariate signal and finally processed directly using MEMD. This way, same number of IMFs are guaranteed for each channel and similar

[3]For clarity, WGN channels are not plotted here.

oscillatory modes are extracted in same-indexed IMFs, a feat not possible to achieve using EEMD. Moreover, since N-A MEMD is based on MEMD method, which can inherently process multivariate signals containing any number of channels, N-A MEMD can handle both univariate and multivariate signals, whereas, EEMD is only designed for univariate signals.

In the following subsections, a comparison between the two methods is presented in terms of their completeness, which depends on how much residual noise they allow in the reconstructed signal, and their sensitivity to input noise power.

6.4.1 Residual Noise

Residual noise in EEMD is introduced because noise is added directly to the signal in order to enforce the dyadic filter bank structure. Consequently, the reconstructed signal in EEMD contains a significant residual noise compromising the completeness of EEMD, though, its effects can be reduced by increasing the number of samples N, in accordance with equation (6.2). On the other hand, in N-A MEMD, noise does not directly interfere with the original signal as it is added to separate channels.

To verify the above statements, simulations were performed on a synthetic signal shown in Figure 6.3 using both EEMD and N-A MEMD; $N = 250$ realizations of WGN were used in EEMD and the noise power was taken as 0.05, whereas, for N-A MEMD, $l = 2$ WGN channels were added to the signal with the same noise power as in EEMD. The number of direction vectors used in MEMD were taken as $V = 512$. Figure 6.5 shows the resulting decompositions, in (a) and (b) for EEMD and N-A MEMD respectively, and the absolute values of the error function $e(t) = X(t) - r(t)$, in (c) and (d) for EEMD and N-A MEMD respectively, where $X(t)$ and $r(t)$ denote the input signal and the reconstructed signal. It is clear that the absolute error function corresponding to N-A MEMD has significantly smaller values as compared to that of EEMD because of negligible residual noise in N-A MEMD. The error function in EEMD has larger values due to high levels of residual noise caused by directly adding noise to the input signal X.

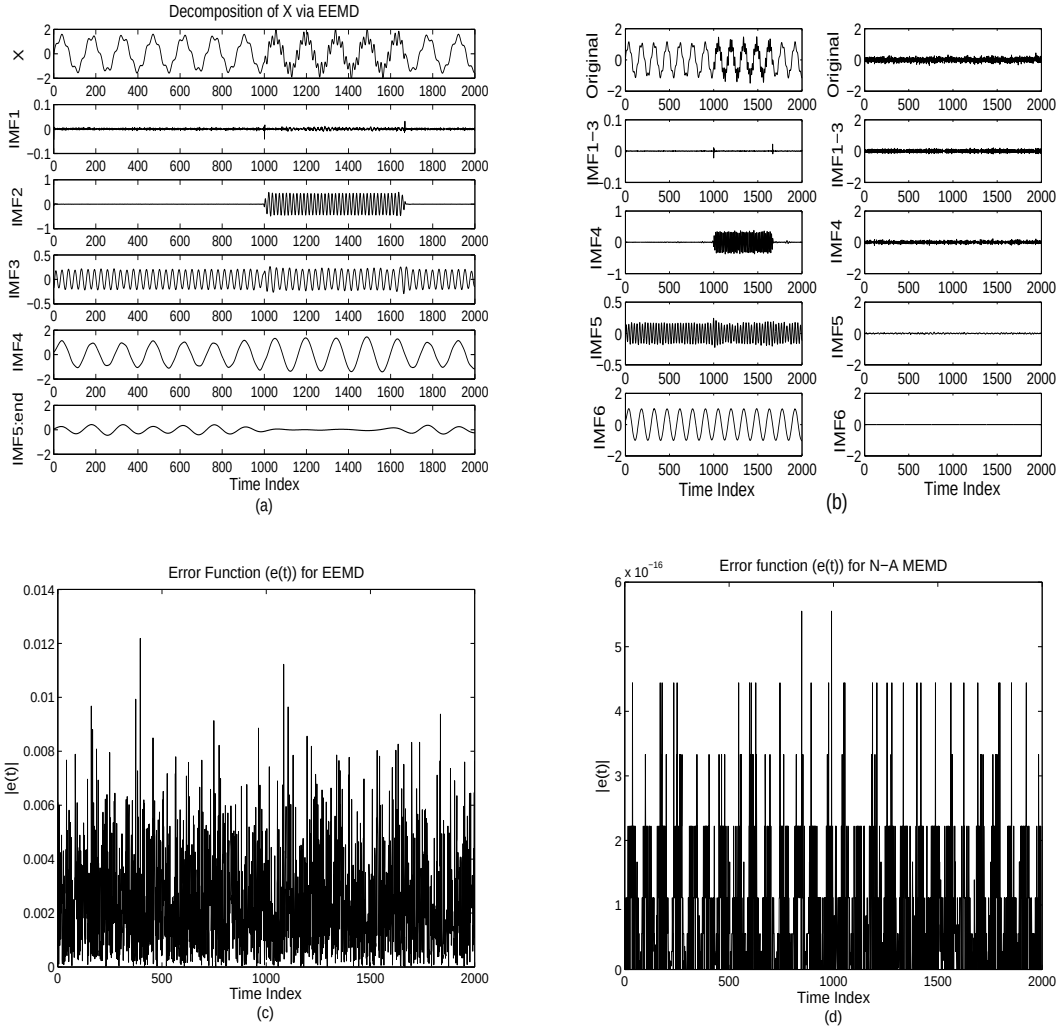

Figure 6.5: Comparison of EEMD vs N-A MEMD in terms of the residual noise in the reconstructed signal. (a) EEMD decomposition of input signal X. (b) N-A MEMD decomposition of input signal X. (c) Absolute value of the error function $e(t)$ between X and the reconstructed signal for EEMD. (d). Absolute value of the error function $e(t)$ between X and the reconstructed signal for N-A MEMD. The absolute error in case of N-A MEMD is significantly lower than EEMD (see the difference in the scales of vertical axes between (c) and (d)).

6.4.2 Sensitivity to Noise Power

The power of added noise relative to the input signal power is an important factor in both EEMD and N-A MEMD since it is crucial to establish filter bank structure. In EEMD, however, this issue is more significant since noise is added directly to the signal and, therefore, increasing its amplitude might raise the residual noise levels in the reconstructed

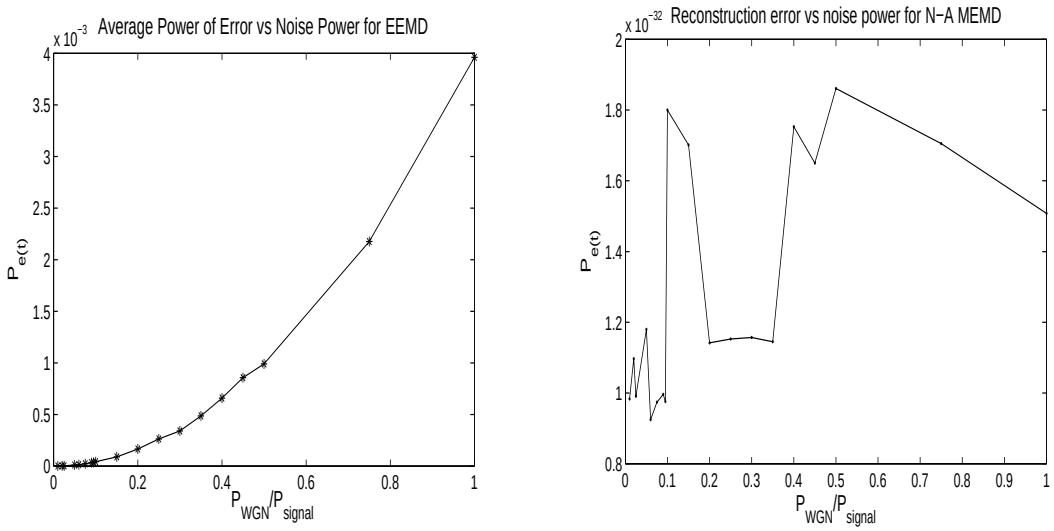

Figure 6.6: Comparison of EEMD vs N-A MEMD in terms of sensitivity to added noise power. (a) Plot of average power of the error signal as a function of noise to signal power in case of EEMD; it is a monotonic increasing function highlighting an increase in residual noise in EEMD with added noise power. (b) The same plot in (a) but corresponding to N-A MEMD. The power of error function is much lower in this case due to less residual noise (see the difference in the scales of vertical axes between the two figures).

signal.

This is shown in Figure 6.6 where the average power of the error signal is plotted as a function of ratio between the noise and the signal power, for the input signal X in Figure 6.3, using EEMD (left) and N-A MEMD (right).

In the case of EEMD, as expected, the power of error signal, which is an indicator of residual noise level, increase with the added noise power. On the other hand, residual noise levels in the reconstructed signal, in the case of N-A MEMD, remain relatively stable with the input noise power, as shown in Figure 6.6(right).

6.5 Discussion

Based on the improvements offered by N-A MEMD, in terms of less residual noise and less sensitivity to added noise power, it is a viable alternative to EEMD for reducing the mode-mixing problem. However, it should be mentioned that the so-called noise-assisted

methods (both EEMD and N-A MEMD) are expected to be most useful, for reducing the mode-mixing problem, only for those signals in which the dyadic filter bank decomposition is relevant. For instance, if the desired signal resides in multiple dyadic subbands, then choosing these noise-assisted methods for decomposition may even 'spread' the desired signal across multiple IMFs, resulting in unwanted mode-mixing. This is due to the fact that adding noise to the signal enforces the dyadic filter bank structure on to the input signal, and in that process, the EEMD and N-A MEMD methods somewhat lose their data-driven ability.

Another important aspect to consider in the case of N-A MEMD is its sensitivity to the number of added noise channels. Though, at most, $l = 2$ noise channels were used in simulations presented in this chapter, there is theoretically no limit to the number of noise channels that can be used in N-A MEMD. However, it is expected that for multivariate signals containing larger number of input channels, the number of input noise channels might have to be increased to enforce the filter bank structure on the data. A formal study on this matter is, however, still needed and might be a good avenue for future research.

To give a rough idea of the dependence of N-A MEMD on the number of noise channels, simulations were performed on the input signal shown in Figure 6.3 by varying the number of noise channels l and calculating the power of the reconstructed error[4]. The results are shown in Figure 6.7 in which the power of the reconstructed error is plotted as a function of the number of WGN channels l. It is clear that the reconstructed error is negligible even for larger values of l ensuring the completeness of N-A MEMD for varying l.

6.6 Conclusions

A noise-assisted MEMD (N-A MEMD) algorithm has been presented as a viable alternative to ensemble EMD (EMD). It uses the filter bank property of MEMD on white Gaussian noise (WGN) by introducing extra channels of multivariate WGN to the input signal.

[4]In the simulations, the noise power in the two channels was kept at 0.05, corresponding to the SNR of 17db, and the number of direction vectors used in MEMD algorithm were taken as $V = 512$.

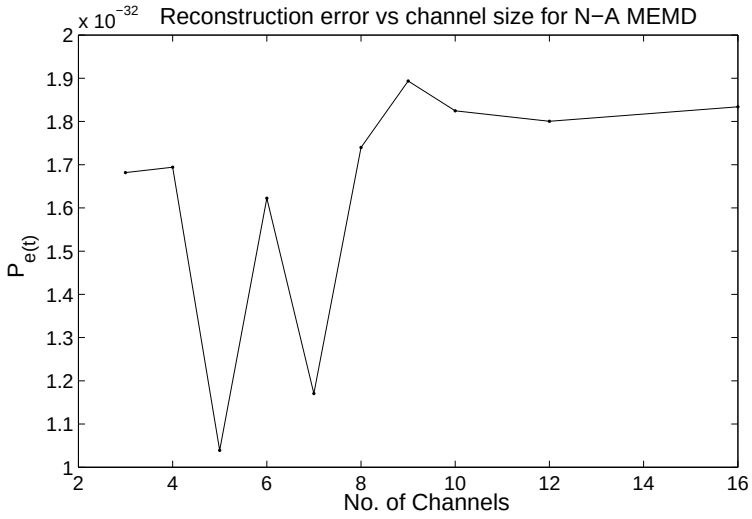

Figure 6.7: Power of the reconstructed signal plotted as a function of number of WGN channels, l, for the input signal in Figure 6.3 using N-A MEMD. See text for further detail.

Consequently, due to the proper alignment of frequency subbands, the effects of mode-mixing and mode-misalignment in multivariate IMFs can be reduced using N-A MEMD. Unlike ensemble EMD (EEMD), where several realizations of white noise are directly added to the signal and then multiple instances of EMD are run, the framework of MEMD allows adding white noise in separate channels. As a result, only a single application of MEMD is sufficient, and due to the separation between the noise and input channels, the residual noise in N-A MEMD is comparatively lower and is found to be less sensitive to noise power than EEMD. Moreover, unlike EEMD, the framework of MEMD allows N-A MEMD to handle a much broad class of multivariate signals.

Chapter 7

Multiscale Image Fusion using MEMD

IN this chapter, multivariate extensions of EMD have been proposed to be used for the multiscale analysis of multichannel data. It has been shown that multivariate extensions of EMD overcome the problem of uniqueness, owing to its property to align common oscillatory modes from multiple channels in the same-indexed IMFs. Consequently, the proposed approach allows the correlation analysis, at local level and at multiple scales, between multiple input channels which can not be achieved by applying univariate EMD channel-wise. This concept is illustrated further via image fusion examples.

7.1 Why Multiscale Analysis for Multichannel Data?

In multichannel data analysis, one often needs to compute correlation between a set of data channels. For linear and stationary data, this can be achieved by simply taking the correlation coefficient over the whole data set. However, most real world multivariate signals are nonstationary and are obtained from nonlinear sources and, hence, 'global' measures such as the correlation coefficient are not adequate to capture the complete relationship between them. For such signals, therefore, a local (time dependent) correlation measure is required. For this cause, Papadimitriou [88] developed a method for obtaining a

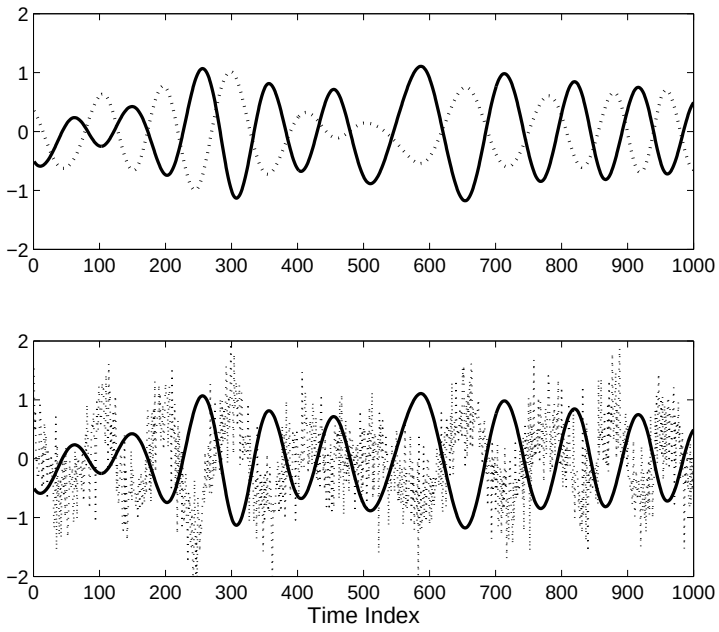

Figure 7.1: Multiscale analysis: The synthetic signals $a(k)$ (solid line) and $b(k)$ (dotted line) (top) and signals $x(k)$ and $y(k)$ (bottom).

local similarity score for nonstationary data by computing the cross correlation coefficient in a local sliding window. The resulting method, though effective in certain scenarios, was not accurate since it did not consider correlation at multiple scales of the data.

To perform multiscale analysis of multichannel (multivariate) data, the input signal is first decomposed into its constituent scales and then an analysis is performed on corresponding (matched) scales, from multiple channels, separately. This is important since real world data mostly consists of a combination of multiple intrinsic time scales, representing different dynamic regimes, and only performing the analysis separately on each scale (dynamic regime) reveals meaningful correlation estimate between the two data sets [17].

To illustrate this point, consider two signals $x(k) = a(k)$ and $y(k) = b(k) + w(k)$ as shown in Figure 7.1, where a and b are highly correlated signals (with correlation coefficient equal to 0.79) with the same mean time scale, and $w(k)$ is the white Gaussian noise of zero mean and unit standard deviation. Even with the presence of noise in y,

intuitively, both x and y should have a reasonable correlation estimate due to the high correlation between a and b. However, the value of the correlation coefficient of x and y was found to be only 0.32. The main reason was that the correlation between the two signals, due to the components a and b, was masked due to the noise component, giving a meaningless correlation estimate. Had x and y been analysed using a multiscale approach, the underlying relationship between a and b could be easily detected, illustrating the importance of decomposing multichannel data into its intrinsic scales before applying the correlation analysis.

7.2 EMD and its Multivariate Extensions for Multiscale Analysis

To decompose data for the purpose of multiscale analysis, empirical mode decomposition (EMD) is an intuitive and natural choice, because its IMFs represent different scales at local level. By recognizing this potential of EMD, Huang et. al. developed a time dependent intrinsic correlation (TDIC) method in order to perform local correlation analysis of data using EMD [89]. This method is similar to the one given in [88] except that it operates at multiple intrinsic scales of the data: the IMFs from standard EMD algorithm. For applications involving multichannel data, however, the use of standard EMD method poses the following problems:

1. Due to the problem of uniqueness, caused by the empirical nature of EMD, a different set of IMFs are obtained for each channel both in terms of their number and properties (refer to section 2.6.1 for details).

2. Mode-mixing in EMD further destroys the alignment of common modes in corresponding IMFs from multiple channels.

The above mentioned issues limit the use of standard EMD in applications such as data fusion, since IMFs from multiple channels are not aligned. Consequently, it is hard to conduct local correlation analysis (comparison) on scale-by-scale basis using standard

EMD. Thus, in order to perform local analysis of multivariate data using EMD at multiple scales, the number of IMFs from all channels must be equal in terms of both their number and properties.

Fortunately, multivariate extensions of EMD fulfill these requirements, and their potential in multiscale analysis of multichannel data is explored in this chapter. It should be mentioned that the complex extensions of EMD have already been employed for fusion applications involving bivariate data [17] [19], but with MEMD and N-A MEMD at disposal, the multiscale signal processing framework based on EMD/BEMD can be extended to signals containing any number of channels. The mode-alignment property observed by MEMD is at the heart of these proposed applications and is briefly discussed next.

7.2.1 Mode-Alignment in Synthetic Sinusoids

For synthetic signals with a combination of sinusoids, it was shown, in section 3.5.2 and section 4.5.1 respectively, that both trivariate EMD (TEMD) and MEMD produced matched or aligned IMFs in terms of their frequency content. Moreover, it was shown in section 2.8 that even if the mode-mixing problem occurred in multivariate extensions, it affected IMFs from multiple channels simultaneously, thus, allowing meaningful comparison at multiple scales. In situations where mode-mixing is still an issue, noise-assisted MEMD (N-A MEMD) may be used.

7.2.2 Mode-Alignment in White Gaussian Noise

The mode-alignment property of MEMD in the case of white Gaussian noise (WGN) was illustrated in detail in Chapter 5. More specifically, it was shown that MEMD follows quasi-dyadic filter bank structure for multivariate WGN with the overlapping frequency spectra for same-indexed IMFs, from multiple channels, as was shown in Figure 5.3.

7.3 Application: Multiscale Image Fusion

Fusion of multiple images is aimed at producing a single output image which carries the salient features of all fused images [90]. Fusion techniques are particularly relevant in cases where it is difficult to obtain an image in which all relevant objects are 'in-focus', and multiple 'out-of-focus' images must be combined to yield a single 'in-focus' image. Another important application is the fusion of multiple multi-exposure images from a static scene, which is required when a wide range of luminosity/irradiance inhibits the camera to capture all features of a scene in a single shot. In such cases, there will always be regions of an image which are either over-exposed or under-exposed. These over- and under-exposed regions usually carry less information as compared to regions which are properly exposed to light, and therefore need to be fused.

For fusion of multiple images, one class of techniques perform 'local' fusion by obtaining local details from images by dividing them into several non-overlapping blocks. Subsequently, image block carrying greater information is selected in the fused image. Using this methodology, Goshtasby proposed entropy as an information measure for the fusion of multiple exposure images [91]. This technique, however, does not perform fusion at multiple intrinsic scales of the input signal (multiscale fusion), and is therefore suboptimal.

Other established techniques operate within the transform domain such as the wavelet transform [92] [38] and the discrete cosine transform (DCT) [93]. These techniques commonly decompose an image into its constituent scale-images, after which coefficients corresponding to each set of scale-images are conveniently combined in the fused image [92]. In effect, these techniques perform comparison between multiple images, at feature (scale) level, and keep the most informative scale in the fused image. However, they fail to accurately extract the local details at data level since they are mainly linear projection-based schemes.

Multivariate extensions of EMD provide a unique opportunity to perform fusion both locally and at feature (multiscale) level due to its data-driven nature. In addition,

its mode-alignment property allows a scale-by-scale comparison between multiple images. The next section present a framework for the fusion of multi-focus and multi-exposure images using multivariate extensions of EMD.

7.3.1 The Proposed Framework

In this section, a framework is given for the fusion of three gray scale images to a single enhanced image using multivariate EMD (MEMD). The methodology employed is similar to that used in [17] for the fusion of two out-of-focus images. Here, a new fusion rule is proposed for multiscale image fusion, which is more suited for the fusion of exposure images. Also, a method to fuse two color images using multiple applications of bivariate EMD (BEMD) is presented. In all subsequent simulations of MEMD, the stopping criterion given in section 4.4 is used with parameter values of $[\theta_1 = 0.05,\ \theta_2 = 0.5,\ \alpha = 0.05]$ and $S = 1$. The number of direction vectors considered in the simulations were $V = 64$.

Gray-Scale Image Fusion Scheme

A framework for fusion of three partially out-of-focus gray scale images is proposed as follows: Three input images, labeled A, B, and C, are first converted to row vectors and combined to form a trivariate signal. MEMD is then applied to the resulting trivariate signal which yields M IMFs, each corresponding to the intrinsic features (scales) of the input images. These IMFs are then reconverted back to 2D images[1], resulting in M scale images for each input image, denoted by A_m, B_m, and C_m for $m = 1, \ldots, M$, as shown in Figure 7.2. Scale images are then combined locally, based on values of coefficients calculated from local variance estimates at each spatial point, to give a fused image F given by

$$F(x,y) = \sum_{m=1}^{M} \alpha_m(x,y)A_m(x,y) + \beta_m(x,y)B_m(x,y) + \gamma_m(x,y)C_m(x,y) \tag{7.1}$$

[1]Applying standard EMD to inherently 2D images results in loss of information in vertical direction which is manifested in horizontal artifacts in the fused image. To alleviate this problem, the IMFs carrying sufficiently low frequencies are combined (added) together [17].

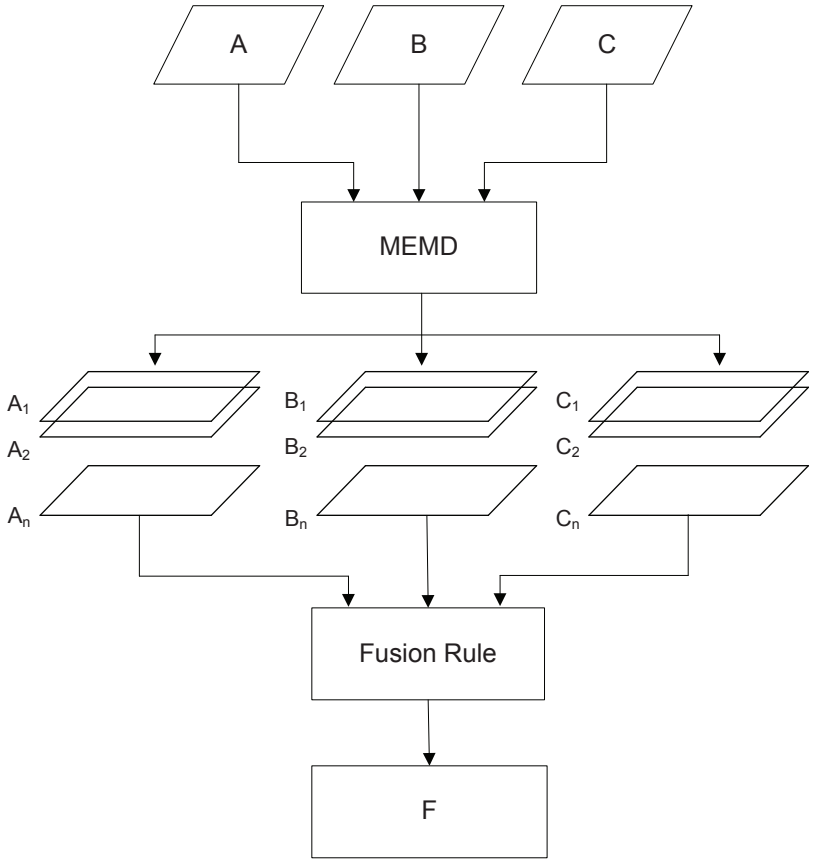

Figure 7.2: The proposed methodology for three gray scale image fusion using multivariate EMD (MEMD).

where $\alpha_m(x,y)$, $\beta_m(x,y)$, and $\gamma_m(x,y)$[2] are coefficients, determined at location (x,y), based on the relative values of the local variance for each scale, and are given by

$$\alpha_m(x,y) = \frac{\text{var}\{A_m(x,y)\}}{\text{var}\{A_m(x,y)\} + \text{var}\{B_m(x,y)\} + \text{var}\{C_m(x,y)\}} \tag{7.2}$$

$$\beta_m(x,y) = \frac{\text{var}\{B_m(x,y)\}}{\text{var}\{A_m(x,y)\} + \text{var}\{B_m(x,y)\} + \text{var}\{C_m(x,y)\}} \tag{7.3}$$

$$\gamma_m(x,y) = \frac{\text{var}\{C_m(x,y)\}}{\text{var}\{A_m(x,y)\} + \text{var}\{B_m(x,y)\} + \text{var}\{C_m(x,y)\}} \tag{7.4}$$

where $\text{var}[A_m(x,y)]$ represents the local variance of a scale image A_m, calculated across a small rectangular block around (x,y), as follows

[2]By choosing $C = 0$ and $\gamma(x,y) = 0$, the same methodology, as above, can be used for the fusion of two gray scale images.

$$\text{var}\{A_m(x,y)\} = \sum_{i=-W_i}^{W_i} \sum_{j=-W_j}^{W_j} [A_m(x+i, y+j) - \mu_{ij}]^2 \tag{7.5}$$

where μ_{ij} denotes the mean of all the elements inside the window, and W_i and W_j determine the rectangular window size. In the simulations presented in this chapter, a square window of size $W_i * W_j = 100$ was used.

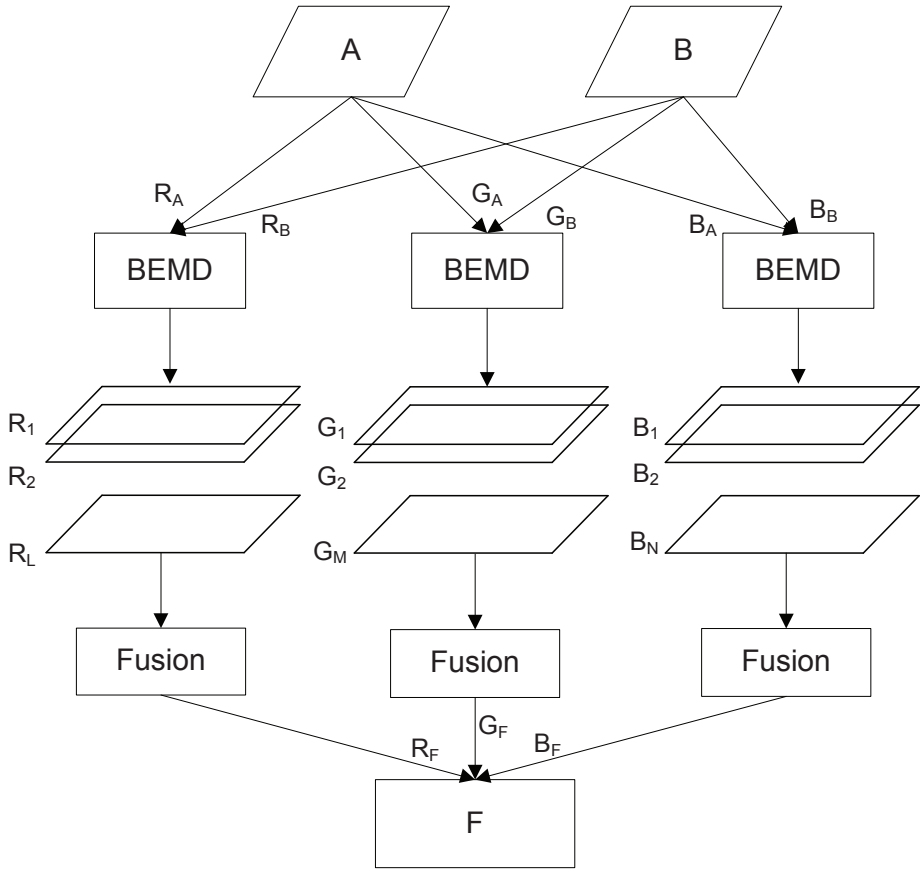

Figure 7.3: The proposed methodology for two RGB color image fusion using bivariate EMD (BEMD).

RGB-Color Image Fusion Scheme

In order to extend the above fusion methodology to RGB-based colored images, it is applied to three color channels, red (R), green (G), and blue (B), of an image separately. That is, the red, green, and blue channels from two input images are processed by three separate

applications of bivariate EMD algorithm, as shown in Figure 7.3. As a result, three sets of bivariate IMFs are obtained which correspond to the red, green, and blue channels of two input images. Note that although the three instances of bivariate EMD generally yield different numbers of IMFs, each set is processed separately by the fusion algorithm to yield the fused red, green and blue channel. The fusion rule on each color channel is similar to the one used for gray scale fusion, in equation (7.1), but with $\gamma(x, y) = 0$. Finally, the fused channels are combined to form a fused RGB-based color image, F.

7.3.2 Results: Multi-Exposure Image Fusion

The performance of the proposed method is evaluated on real-world multi-exposure images shown in Figure 7.4(a) and Figure 7.4(b); these are images of a work table obtained at multiple exposures. Observe that in the first input image, the details on the table are hidden due to over-exposure, but the area below the table is well exposed. In the second input image, the lower region is severely underexposed, whereas the upper part of the image, showing details on the table itself, is well exposed. For comparison, a multi-resolution wavelet-based fusion scheme is also used: the Discrete Wavelet transform (DWT) was first applied to both input images to obtain their multiscale decompositions. The wavelet transform coefficients corresponding to the same decomposition level of two images, were combined to obtain fused multiscale coefficients. The coefficients were then converted back to the fused image using the inverse wavelet transform. In simulations, the largest coefficient which corresponds to the sharpest brightness changes in the image, such as, edges and lines etc, were chosen. The selection of the largest wavelet coefficient is also consistent with the local variance based fusion algorithm used in EMD-based approach, since both criteria select variations in intensity as salient features in an image.

Figure 7.4(c) shows the results of the fusion of input images using the discrete Wavelet transform (DWT). In the fused image, distortions are clearly evident, especially in the upper part of the image where details on the table are shown; observe the artifacts around the cable and the paper. It can also be observed that the container on the right side of the table is still overexposed in the fused image.

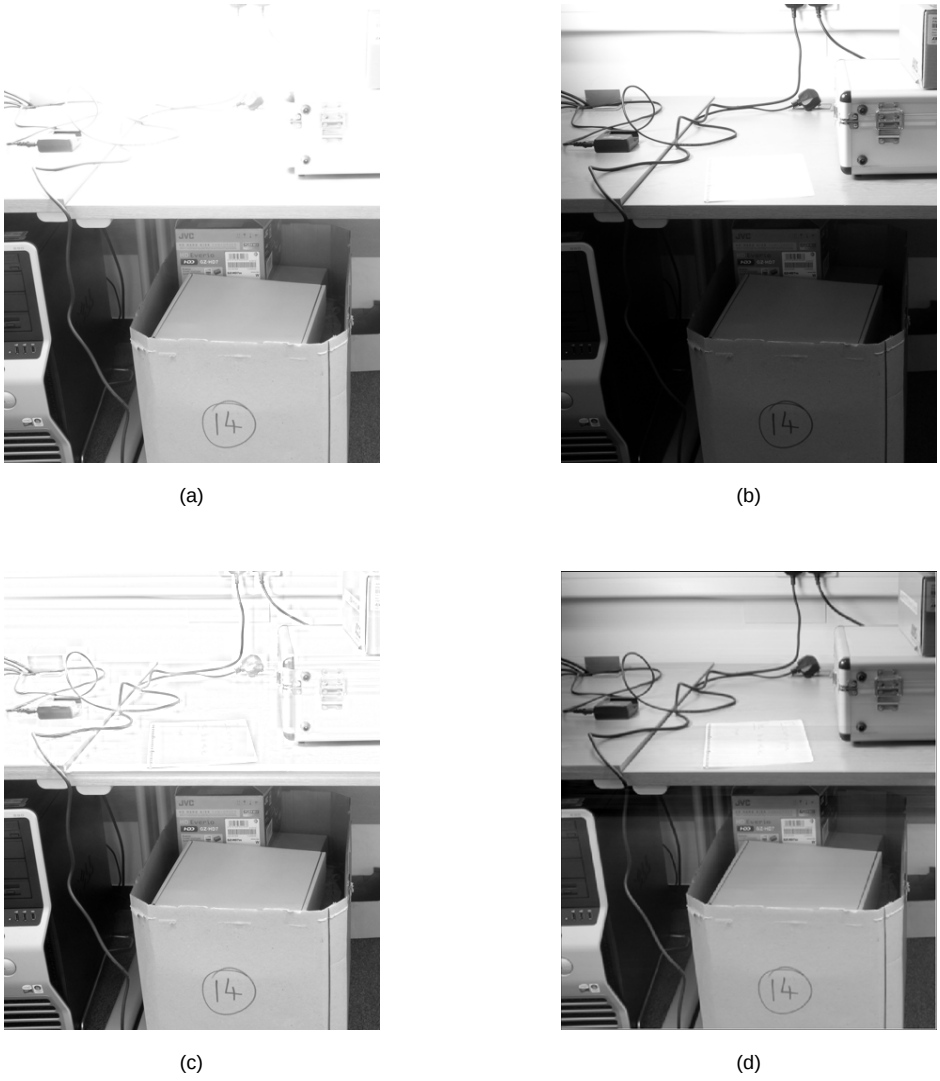

Figure 7.4: Local and Multiscale image fusion: (a, b) Images of a work table at different exposures. In (a), details on the table are hidden due to overexposure to light. whereas in (b), the lower region of the image is severely underexposed. (c) A fused image obtained using the discrete Wavelet transform. (d) A fused image obtained using the proposed framework in Figure 7.2.

The fused image from the EMD-based fusion scheme is shown in Figure 7.4(d); it is clear that EMD-based fusion outperforms wavelet-based fusion, as less distortions are present. The distortions around the wire and paper in the wavelet-based fusion arose due to the fact that it is not performed at 'local' level in the spatial domain; the coefficient merging occurs in the transform domain. As a result, the wavelet-based fusion scheme cannot accurately align, compare and process high frequency scales. On the other hand,

(a) (b)

(c)

Figure 7.5: RGB image fusion: (a) Over-exposed image. (b) Under-exposed image. (c) Fused color image obtained by using the proposed framework in Figure 7.3.

data-driven nature of EMD facilitates fusion at the local level, yielding better results even at high frequency scales.

The proposed scheme for RGB-based color image fusion, shown in Figure 7.3, was also used to perform fusion of two exposure images shown in the top row of Figure 7.5; The fused image is shown in Figure 7.5(c). Again, it is evident that both the local and multiscale nature of the proposed fusion framework yielded good results, with fused image being well exposed.

Figure 7.6: Gray-scale image fusion using MEMD: Three out-of-focus images are fused to extract all-in-focus image (lower right).

7.3.3 Results: Multi-Focus Image Fusion

The methodology given in Figure 7.2 for the fusion of gray images was applied to three partially out-of-focus gray scale images shown in Figure 7.6. In all three images, different portions of the girl's face are obscured but the fused image obtained from the proposed framework, as shown in Figure 7.6 (lower right), has all parts of the girl's face in focus.

7.4 Conclusions

It has been shown that multiscale analysis of a signal is a prerequisite for obtaining accurate results especially in fusion applications. While standard EMD has shown potential for obtaining multiple scales of a univariate signal, it is not suitable for multivariate signals as, generally, it fails to align common modes from multiple channels. Multivariate extensions of EMD, however, overcome these problems and thus are more suited for a robust fusion framework, which can also operate locally; the benefits of such frameworks have been shown in the context of real world image fusion.

Chapter 8

Conclusions and Future Work

8.1 Conclusions

IN this thesis, several algorithms have been proposed to process multivariate signals locally, at the data level, using data fission–the decomposition of a multivariate signal into a set of its intrinsic components. These extensions are crucial because of the two main reasons:

Firstly, the proposed extensions are aimed at handling real world signals exhibiting complex properties such as nonlinearity and nonstationarity. These attributes though commonly encountered in real world signals, such as inertial body motion data, images, and wind, are generally overlooked in classical signal processing algorithms and, hence, the need for nonstationary data-driven algorithms operating at multiple intrinsic scales of the data.

Secondly, the recent advances in the data acquisition systems have given rise to multivariate (multichannel) real world data in several fields, which in turn, has highlighted the need for direct processing of such data via multivariate signal processing tools. Applying univariate algorithms channel-wise may be suboptimal in such cases as they do not consider inter-channel correlations within the multivariate data.

In this thesis, extensions of Empirical Mode Decomposition (EMD) algorithm have been proposed for multivariate signals, whereby signals containing any number of chan-

nels can be processed. In addition to gaining benefits in terms of the direct processing of multivariate real world nonstationary signals; highly localized MEMD analysis at multiple scales; and accurate time-frequency (TF) distributions with the aid of Hilbert transform; the proposed multivariate extension has also been shown to circumvent the non-uniqueness problem in standard EMD algorithm, paving the way for its use in data fusion applications. The non-uniqueness in standard EMD is characterized by the emergence of different number of decompositions and properties even for signals with similar statistics, and this combined with other issues such as mode-mixing has rendered standard EMD not viable for data fusion applications, where scale-by-scale comparison between sources is a prerequisite. In this thesis, multivariate extensions of EMD have been shown to be a viable alternative in such cases. Moreover, by virtue of the filterbank property of MEMD on white Gaussian noise (WGN) and using the multivariate framework of MEMD, an enhanced MEMD method is presented which reduces the mode-mixing problem in MEMD and, hence, is even more suitable in practical scenarios.

In this thesis, details of the EMD algorithm and its complex extensions were first presented in Chapter 2. This was followed by trivariate extension of EMD (TEMD), presented in Chapter 3, which is designed for processing the signals containing three channels. The main principle of TEMD is based on taking input signal projections along multiple points on a spherical coordinate system, in 3D space, for estimating the local mean. Furthermore, TEMD algorithm was shown to align common oscillatory modes just like the complex extensions of EMD and was also demonstrated to perform accurate TF analysis in the case of real world trivariate wind signal. In addition, linearity analysis of IMFs from TEMD, via delay vector variance (DVV) method, showed that except for the first couple of IMFs which preserved original signal's modality, the rest of the IMFs were found to be largely linear and deterministic.

In Chapter 4, an extension of EMD algorithm for general multivariate signals (MEMD), containing any number of channels, was presented. Though the main principle of this extension is similar to that of BEMD and TEMD, i.e. taking projections of a signal in multiple directions, the main challenge was to choose a uniform point set

in n-dimensional spaces, which was achieved by a low-discrepancy Hammersley sequence. Moreover, MEMD was shown to exhibit similar characteristics to that of TEMD algorithm, including the alignment of similar scales across the same-indexed IMFs.

Next, the filterbank property of MEMD on multivariate white Gaussian noise (WGN) was demonstrated in Chapter 5. By virtue of this property and making use of the ability of MEMD to process any number of channels, the noise-assisted MEMD algorithm was proposed in Chapter 6, which aims to reduce mode-mixing in EMD and MEMD algorithms. The rationale behind N-A MEMD is to impose the filter bank structure on the input multivariate signal by adding separate noise channels to it. This way, the proposed method achieves the separation between the noise and the input signal while still making use of the desired filter bank property, resulting in significantly lower reconstruction errors as compared to other noise-assisted methods including ensemble EMD (EEMD). Moreover, through extensive simulations, the proposed method was also found to be more robust in terms of its sensitivity to noise power as compared to EEMD.

In Chapter 7, a fusion architecture was proposed for both bivariate and trivariate data, whereby the most informative data at each mode was retained in the output signal. The approach was used to perform image fusion of multiple out-of-focus images and multiple exposure images, and its performance was compared to the established image fusion algorithms. Despite its effectiveness, however, the proposed architecture may not be optimal for image fusion, since it is inherently designed for multivariate signal, rather than multidimensional data such as images [94]; complex/bi-dimensional EMD extensions must be designed for such applications.

8.2 Future Work

The material presented in this thesis has been published in leading research journals and top conferences in the signal processing field. Given the known potential of EMD in real world nonlinear and nonstationary signal processing, the proposed extensions are expected to find numerous applications in several fields. Indeed, since their inception, the extensions

proposed in this thesis have already found several practical applications, as evidenced by more than 50 citations for TEMD and MEMD algorithms, combined.

Some avenues for future work are discussed below:

8.2.1 Choice of Optimal Number of WGN Channels and Noise Power in N-A MEMD

Though N-A MEMD method is found to be stable for a wide range of values for the number of noise channels and added noise power, currently these parameters are chosen in an ad-hoc fashion, calling for a more systematic method for choosing their optimal values.

8.2.2 EMD-based Stationarity Testing via Surrogate Data

Stationarity within a signal is considered as a prerequisite for applying many signal processing algorithms [4]. Consequently, for a class of nonstationary signals, such as speech data, it is a common practice to first divide such data into stationary segments and then process those segments separately. Therefore, a robust framework aimed at testing the stationarity of a signal, in an operational sense, is required as a pre-processing step in many signal processing applications.

Recently, stationarity testing has been attempted via surrogate data framework [95], which was initially presented for the purpose of establishing a robust statistical test for nonlinearity[1] [96] [97] [98]. Though the test performs well in practice, it suffers from the limitations of Fourier transform, which is not applicable to nonstationary signals, and the lack of a robust discriminating statistic based on 'local' properties of a signal at multiple scales.

EMD can be a useful alternative to Fourier transform for stationarity testing, as it can handle nonstationary signals and can also perform multiscale analysis at the level of local oscillations. Due to these properties, EMD has already been considered for quantifying stationarity using the so-called 'degree of stationarity' (DOS) index [7]. The DOS measure is similar to the intermittency defined in the wavelet analysis, but has a drawback

[1] Refer to Appendix B for further details on surrogate methods.

that it is not a time-dependent measure and, thus, does not fully exploit the local nature nature of EMD.

Recently, a time-dependent intrinsic correlation (TDIC) method, based on EMD, has been proposed by Huang et. al which has a potential in stationarity testing at local level [89]. The method measures the autocorrelation coefficient of the data over multiple scales (IMFs), and uses the instantaneous frequency of the IMFs to determine a set of sliding window sizes for the computation of running autocorrelation coefficients. The method mainly gives an accurate intrinsic correlation analysis of the data but also has a tremendous potential in the context of stationarity testing which is yet to be explored; a robust framework using TDIC measure, as a discriminating statistic, in combination with the surrogate data methodology will lead to a powerful local stationarity test based on EMD.

Next, to alleviate the shortcomings of the Fourier transform in surrogate data methods for stationarity, the potential of other frequency measures, such as the EMD-based marginal Hilbert spectrum can be explored [7]. Thus, the main rationale behind the proposed work would be to preserve the marginal Hilbert spectrum of the signal, instead of Fourier spectrum, in order to yield the stationary surrogates. The resulting distribution of the TDIC measure obtained from stationary surrogates would be compared against the corresponding distribution of the original signal to obtain a statistical test for stationarity. The advantage of using the Hilbert spectrum over the Fourier spectrum stems from its improved accuracy as it is derived from the EMD, which, unlike Fourier transform, is a completely data-driven algorithm and considers the signal at the level of its local oscillations. In short, the resulting test is expected to provide better results for the following reasons:

1. The time dependent intrinsic correlation (TDIC) is based on EMD and is a completely local measure making it highly suitable for nonstationarity testing as compared to Fourier-based methods.

2. The proposed test will be performed at multiple intrinsic scales of the data; this is motivated by the fact that performing local autocorrelation analysis on signals

containing multiple scales may yield misleading estimates, if multiple scales are not considered separately [89] [17].

Bibliography

[1] S. M. Kay, *Fundamentals of statistical signal processing: Estimation theory.* Prentice-Hall PTR, 1993.

[2] S. M. Kay, *Fundamentals of statistical signal processing: Detection theory.* Prentice-Hall, 1998.

[3] P. J. Brockwell and R. A. Davis, *Time Series: Theory and Methods.* Springer, 1991.

[4] P. Flandrin, *Time-frequency/time-scale analysis.* San Diego; London: Academic Press, 1999.

[5] C. K. Chui, *An Introduction to Wavelets.* San Diego: Academic Press, 1992.

[6] L. Cohen, *Time-Frequency Analysis.* Prentice-Hall, New York, 1995.

[7] N. E. Huang, Z. Shen, S. Long, M. Wu, H. Shih, Q. Zheng, N. Yen, C. Tung, and H. Liu, "The empirical mode decomposition and Hilbert spectrum for non-linear and non-stationary time series analysis," *Proceedings of the Royal Society A*, vol. 454, pp. 903–995, 1998.

[8] N. E. Huang and S. S. P. Shen, *Hilbert-Huang Transform and its Applications.* Singapore: World Scientific, 2005.

[9] E. Pereda, R. Q. Quiroga, and J. Bhattacharya, "Nonlinear multivariate analysis of neurophysiological signals," *Progress in Neurobiology*, vol. 77, p. 137, 2005.

[10] Y. Liu and S. Aviyente, "Multichannel EEG analysis based on multi-scale multi-information," in *Proceedings of IEEE International Conference on Acoustics, Speech, and Signal Processing*, 2011.

[11] W. Yang, J. Jiang, P. J. Tavner, and C. J. Crabtree, "Monitoring wind turbine condition by the approach of empirical mode decomposition," in *Proceedings of International Conference on Electrical Machines and Systems, Wuhan*, 2008.

[12] C. Vincent, G. Giebel, P. Pinson, and H. Madsen, "Resolving nonstationary spectral information in wind speed time series using the Hilbert-Huang transform," *American Meteorological Society*, vol. 49, pp. 253–267, 2010.

[13] Y. L. Xu and J. Chen, "Characterizing nonstationary wind speed using empirical mode decomposition," *Journal of Structural Engineering*, vol. 6, pp. 912–920, 2004.

[14] N. E. Huang, M. Wu, W. Qu, S. R. Long, S. S. P. Shen, and J. E. Zhan, "Applications of Hilbert-Huang transform to non-stationary financial time series analysis," *Applied Stochastic Models in Bussiness Industry*, vol. 19, pp. 245–268, 2003.

[15] K. Guhathakurtaa, I. Mukherjeea, and A. R. Chowdhury, "Empirical mode decomposition analysis of two different financial time series and their comparison," *Chaos, Solitons and Fractals*, vol. 37, pp. 1214–1227, 2008.

[16] K. Drakakis, "Empirical mode decomposition of financial data," *International Mathematical Forum*, vol. 3, pp. 1191–1202, 2008.

[17] D. Looney and D. P. Mandic, "Multi-scale image fusion using complex extensions of EMD," *IEEE Transactions in Signal Processing*, vol. 57, no. 4, pp. 1626–1630, 2009.

[18] N. Rehman and D. P. Mandic, "Multivariate empirical mode decomposition," *Proceedings of the Royal Society A*, vol. 466, pp. 1291–1302, 2010.

[19] D. Looney, C. Park, P. Kidmose, M. Ungstrup, and D. P. Mandic, "Measuring phase synchrony using complex extensions of EMD," in *Proceedings of the IEEE Statistical Signal Processing Symposium*, pp. 49–52, 2009.

[20] T. Tanaka and D. P. Mandic, "Complex empirical mode decomposition," *IEEE Signal Processing Letters*, vol. 14, no. 2, pp. 101–104, 2006.

[21] M. U. Altaf, T. Gautama, T. Tanaka, and D. P. Mandic, "Rotation invariant complex empirical mode decomposition," in *Proceedings of the IEEE International Conference on Acoustics, Speech, Signal Processing*, 2007.

[22] G. Rilling, P. Flandrin, P. Goncalves, and J. M. Lilly, "Bivariate empirical mode decomposition," *IEEE Signal Processing Letters*, vol. 14, pp. 936–939, 2007.

[23] H. Hariharan, A. Gribok, M. A. Abidi, and A. Koschan, "Image fusion and enhancement via empirical mode decomposition," *Journal of Pattern Recognition Research*, vol. 1, pp. 16–32, 2006.

[24] C. M. Sweeny-Reed and S. J. Nasuto, "A novel approach to the detection of synchronisation in EEG based on empirical mode decomposition," *Journal of Computational Neuroscience*, vol. 23, no. 1, pp. 79–111, 2000.

[25] R. B. Pachori, "Discrimination between ictal and seizure-free EEG signals using empirical mode decomposition," *Research Letters in Signal Processing*, vol. 2008, pp. 1–5, January 2008.

[26] P. Flandrin, G. Rilling, and P. Goncalves, "Empirical mode decomposition as a filter bank," *IEEE Signal Processing Letters*, vol. 11, pp. 112–114, 2004.

[27] P. K. Varshney, "Multisensor data fusion," *Electronics and Communication Engineering Journal*, vol. 9, pp. 245–253, 1997.

[28] E. Waltz and J. Llinas, *Multisensor Data Fusion.* Artech House, 1990.

[29] D. P. Mandic, D. Obradovic, A. Kuh, T. Adali, U. Trutschell, M. Golz, P. D. Wilde, J. Barria, A. Constantinides, and J. Chambers, "Data fusion for modern engineering applications: An overview," *Proceedings of the IEEE International Conference on Artificial Neural Networks (ICANN)*, pp. 715–721, 2005.

[30] D. L. Hall and J. Llinas, "An introduction to multisensor data fusion," *Proceedings of the IEEE*, vol. 85, no. 1, pp. 6–23, 1997.

[31] Z. Wu and N. E. Huang, "Ensemble Empirical Mode Decomposition: A noise-assisted data analysis method," *Advances in Adaptive Data Analysis*, vol. 1, pp. 1–41, 2009.

[32] C. Damerval, S. Meignen, and V. Perrier, "A fast algorithm for bidimensional EMD," *IEEE Signal Processing Letters*, vol. 12, pp. 123–125, 2005.

[33] C. Junsheng, Y. Dejie, and Y. Yu, "Research on the intrinsic mode function (IMF) criterion in EMD method," *Mechanical Systems and Signal Processing*, vol. 20, pp. 817–824, 2006.

[34] D. J. Duffy, "The application of Hilbert-Huang transforms to meteorological datasets," *Journal of Atmospheric and Oceanic Technology*, vol. 21, no. 4, pp. 599–611, 2004.

[35] N. E. Huang and Z. Wu, "A review on Hilbert-Huang transform: Method and its applications to geophysical studies," *Reviews in Geophysics*, vol. 46, no. RG2006, 2008.

[36] M. Wu and C. Hu, "Empirical mode decomposition and synchrogram approach to cardiorespiratory synchronization," *Physical Review E*, vol. 73, p. 051917, 2006.

[37] S. G. Mallat, "A theory for multiresolution signal decomposition: The Wavelet representation," *IEEE Transaction on Pattern Analysis and Machine Intelligence*, vol. 11, pp. 674–693, 1989.

[38] S. G. Mallat, *A Wavelet Tour of Signal Processing.* Academic Press, 3 ed., 2008.

[39] P. Flandrin and P. Goncalves, "Empirical mode decomposition as data-driven Wavelet like expansions," *International Journal of Wavelets, Multiresolution and Information Processing*, vol. 2, pp. 1–20, 2004.

[40] N. E. Huang, Z. Wu, S. R. Long, K. C. Arnold, K. Blank, and T. W. Liu, "On instantaneous frequency," *Advances in Adaptive Data Analysis*, vol. 1, pp. 177–229, 2009.

[41] S. O. Rice, "Mathematical analysis of random noise," *Bell Sys. Tech. Jl*, vol. 23, pp. 282–310, 1944.

[42] S. O. Rice, "Mathematical analysis of random noise. ii. power spectrum and correlation functions," *Bell Sys. Tech. Jl*, vol. 23, pp. 310–332, 1944.

[43] S. O. Rice, "Mathematical analysis of random noise. iii. statistical properties of random noise currents," *Bell Sys. Tech. Jl*, vol. 24, pp. 46–108, 1945.

[44] B. Boashash, "Estimating and interpreting the instantaneous frequency of a signal. i. fundamentals," *Proceedings of the IEEE*, vol. 80, pp. 520–538, 1992.

[45] E. Bedrosian, "A product theorem for Hilbert transform," *Proceedings of the IEEE*, vol. 51, pp. 868–869, 1963.

[46] N. E. Huang, M. Wu, S. Long, S. Shen, W. Qu, P. Gloersen, and K. Fan, "A confidence limit for the empirical mode decomposition and Hilbert spectral analysis," *Proceedings of the Royal Society A*, vol. 459, pp. 2317–2345, 2003.

[47] C. de Boor, *A Practical Guide to Splines*. Springer-Verlag, New York, 1978.

[48] Y. Kopsinis and S. McLaughlin, "Investigation and performance enhancement of the empirical mode decomposition method based on a heuristic search optimization approach," *IEEE Transactions on Signal Processing*, vol. 56, pp. 1–13, 2008.

[49] Y. Kopsinis and S. McLauglin, "Improved EMD using doubly-iterative sifting and high order spline interpolation," *EURASIP Journal on Advances in Signal processing*, pp. 1–8, 2008.

[50] G. Rilling, P. Flandrin, and P. Gonalves, "On empirical mode decomposition and its algorithms," in *IEEE-EURASIP Workshop Nonlinear Signal Image Processing (NSIP)*, 2003.

[51] I. Daubechies, J. Lu, and H.-T. Wu, "Synchrosqueezed Wavelet transform: A tool for empirical mode decomposition," *Applied and computational harmonic analysis*, vol. 30, no. 2, pp. 1–23, 2010.

[52] Z. Wu and N. E. Huang, "A study of the characteristics of white noise using the empirical mode decomposition method," *Proceedings of the Royal Society A*, vol. 460A, pp. 1597–1611, 2004.

[53] P. Flandrin, G. Rilling, and P. Goncalves, *EMD equivalent filter banks, from interpetation to applications*, ch. 3, pp. 67–87. Hilbert-Huang Transform and Its Applications; Singapore: World Scientific, 1 ed., 2005.

[54] Y. Kopsinis and S. McLaughlin, "Development of EMD-based denoising methods inspired by wavelet thresholding," *IEEE Transactions in Signal Processing*, vol. 57, pp. 1351–1362, 2009.

[55] R. J. Gledhill, *Methods for investigating conformational change in biomolecular simulations*. PhD thesis, The Department of Chemistry, University of Southampton, 2003.

[56] M. E. Torres, M. A. Colominas, G. Schlotthauer, and P. Flandrin, "A complete ensemble empirical mode decomposition with adaptive noise," *Proceedings of the IEEE International Conference on Acoustics, Speech and Signal Processing*, pp. 4144–4147, 2011.

[57] G. Rilling and P. Flandrin, "One or two frequencies? The empirical mode decomposition answers," *IEEE Transactions on Signal Processing*, vol. 56, no. 1, pp. 85–95, 2008.

[58] R. Deering and J. F. Kaiser, "The use of a masking signal to improve empirical mode decomposition," *Proceedings of the IEEE International Conference on Acoustics, Speech and Signal Processing*, pp. 485–488, 2005.

[59] D. Looney and D. P. Mandic, "A machine learning enhanced empirical mode decomposition," *Proceedings of the IEEE International Conference on Acoustics, Speech, and Signal Processing*, pp. 1897–1900, 2008.

[60] N. Rehman, D. Looney, T. Rutkowski, and D. P. Mandic, "Bivariate EMD-based image fusion," in *Proceedings of the 2009 IEEE Workshop on Statistical Signal Processing*, 2009.

[61] D. P. Mandic and V. S. L. Goh, *Complex Valued Non-linear Adaptive Filters: Noncircularity, Widely Linear Neural Models*. Wiley, 2009.

[62] C. Park, D. Looney, and D. P. Mandic, "Time frequency analysis of asymmetry using EMD," *accepted in IEEE Transactions on Neural Systems and Rehabilitation Engineering*, 2010.

[63] H. Niederreiter, *Random number generation and quasi-Monte Carlo methods*. Society for Industrial and Applied Mathematics, 1992.

[64] D. Looney and D. P. Mandic, "A machine learning enhanced empirical mode decomposition," in *Proceedings of the International Conference on Acoustics, Speech, Signal Processing*, pp. 1897–1900, 2008.

[65] M. Chen, D. P. Mandic, P. Kidmose, and M. Ungstrup, "Qualitative assessment of intrinsic mode functions of empirical mode decomposition," in *IEEE International Conference on Acoustics, Speech, Signal Processing*, pp. 1905–1908, 2008.

[66] D. P. M. *et. al.*, ed., *Signal Processing Techniques for Knowledge Extraction and Information Fusion*. Springer, 2008.

[67] N. Williams, S. J. Nasuto, and J. D. Saddy, "Evaluation of empirical mode decomposition for event-related potential analysis," *EURASIP Journal on Advances in Signal Processing*, vol. 2011, pp. 1–11, 2011.

[68] T. M. Rutkowski, A. Cichocki, A. L. Ralescu, and D. P. Mandic, "Emotional states estimation from multichannel EEG maps," in *Advances in Cognitive Neurodynamics ICCN*, 2007.

[69] T. Rutkowski, D. P. Mandic, A. Cichocki, and A. Przybyszewski, "EMD approach to multichannel EEG data analysis - the amplitude and phase components clustering," *Journal of Circuits, Systems, and Computers*, vol. 19, no. 1, pp. 215–229, 2010.

[70] T. M. Rutkowski, A. Cichocki, T. Tanaka, D. P. Mandic, J. Cao, and A. L. Ralescu, "Multichannel spectral pattern separation-an EEG processing application," *Proceedings of the IEEE International Conference on Acoustics, Speech, Signal Processing*, pp. 373–376, 2009.

[71] N. Rehman and D. P. Mandic, "Empirical mode decomposition for trivariate signals," *IEEE Transactions in Signal Processing*, vol. 58, pp. 1059–1068, 2010.

[72] J. Ruppert and R. Seidel, "On the difficulty of triangulating three-dimensional nonconvex polyhedra," *Discrete Computational Geometry*, vol. 7, pp. 227–253, 1992.

[73] A. Yershova and S. M. LaValle, "Deterministic sampling methods for spheres and SO(3)," in *IEEE International Conference on Robotics and Automation*, pp. 3974–3980, 2004.

[74] J. Cui and W. Freeden, "Equidistribution on the sphere," *Siam Journal of Scientific Computations*, vol. 18, no. 2, pp. 595–609, 1997.

[75] V. V. Andrievskii, H. P. Blatt, and M. Gotz, "Discrepancy estimates on the sphere," *Mh. Maths*, vol. 128, pp. 179–188, 1999.

[76] Y. Kopsinis and S. McLaughlin, "Empirical mode decomposition-based denoising techniques," in *Proceedings of 1st IAPR Workshop Cogn. Inf. Process. (CIP), Santorini, Greece*, pp. 42–47, 2008.

[77] N. Rehman, Y. Xia, and D. P. Mandic, "Application of multivariate empirical mode decomposition for seizure detection in EEG signals," in *Proceedings of the Engineering in Medicine and Biology Society (EMBC)*, 2010.

[78] A. Y. Mutlu and S. Aviyente, "Multivariate empirical mode decomposition for quantifying multivariate phase synchronization," *EURASIP Journal on Advances in Signal Processing*, vol. 2011, pp. 1–13, 2011.

[79] M. Hu and H. Liang, "Adaptive multiscale entropy analysis of multivariate neural data," *accepted for pubication in IEEE Transactions on Biomedical Engineering*, 2011.

[80] D. Looney, *Data Fusion Via Fission Using Multiscale Methods*. PhD thesis, Imperial College London, 2011.

[81] Q. Shi, W. Zhou, J. Cao, D. P. Mandic, T. Tanaka, T. M. Rutkowski, and R. Wang, "An auditory oddball based brain-computer interface system using multivariate EMD," in *Proceedings of the Advanced intelligent computing theories and applications*, 2010.

[82] N. Rehman and D. P. Mandic, "Filterbank property of multivariate empirical mode decomposition," *IEEE Transactions on Signal Processing*, vol. 59, pp. 2421–2426, 2011.

[83] J. Fleureau, A. Kachenoura, J. C. Nunes, L. Albera, and L. Senhadji, "3a-EMD: A generalized approach for monovariate and multivariate EMD," *Proceedings on 10th International Conference on Information Science, Signal Processing and their Applications*, pp. 300 – 303, 2010.

[84] J. Fleureau, J. C. Nunes, A. Kachenoura, L. Albera, and L. Senhadji, "Turning tangent empirical mode decomposition: A framework for mono- and multivariate signals," *IEEE Transactions in Signal Processing*, vol. 59, no. 3, pp. 1309 – 1316, 2011.

[85] J.-R. Yeh, J.-S. Shieh, and N. Huang, "Complementary ensemble empirical mode decomposition: A novel noise enhanced data analysis method," *Advances in Adaptive Data Analysis*, vol. 2, pp. 135–156, 2010.

[86] N. E. Huang, Z. Shen, and R. S. Long, "A new view of nonlinear water waves – the Hilbert spectrum," *Annual Review of Fluid Mechanics*, vol. 31, pp. 417–457, 1999.

[87] H. Li, L. Yanga, and D. Huang, "The study of the intermittency test filtering character of Hilbert-Huang transform," *Mathematics and Computers in Simulation*, vol. 70, pp. 22–32, 2005.

[88] S. Papadimitriou, J. Sun, and S. P. Yu, "Local correlation tracking in time series," in *Proceedings of the Sixth International Conference in Date Mining*, pp. 456–465, 2006.

[89] X. Chen, Z. Wu, and N. Huang, "The time-dependent intrinsic correlations based on the empirical mode decomposition," *Advances in Adaptive Data Analysis*, vol. 2, no. 2, pp. 233–265, 2010.

[90] T. Stathaki, *Image Fusion: Algorithms and Applications*. Academic Press, 2008.

[91] A. A. Goshtasby, "Fusion of multi-exposure images," *Image and Vision Computing*, vol. 23, pp. 611–618, 2005.

[92] G. Pajares and J. M. Cruz, "A Wavelet-based image fusion tutorial," *Pattern Recognition*, vol. 37, no. 9, pp. 1855–1872, 2004.

[93] I. Zafar, E. Edirisinghe, and H. Bez, "Multi-exposure and multi-focus image fusion in transform domain," in *Proceedings of IET International Conference on Visual Information Engineering*, 2006.

[94] J. C. Nunes, Y. Bouaoune, E. . Dellechelle, O. Niang, and P. Bunel, "Image analysis by bidimensional empirical mode decomposition," *Image and Vision Computing*, vol. 21, pp. 1019–1026, 2003.

[95] P. Borgnat, P. Flandrin, P. Honeine, C. Richard, and J. Xiao, "Testing stationarity with surrogates: A Time-Frequency approach," *IEEE Transactions in Signal Processing*, vol. 58, pp. 3459–3470, 2010.

[96] J. Theiler, S. Eubank, A. Longtin, B. Galdrikian, and J. Farmer, "Testing for nonlinearity in time series: the method of surrogate data," *Physica D*, vol. 58, p. 77, 1992.

[97] T. Schreiber and A. Schmitz, "Surrogate time series," *Physica D*, vol. 142, pp. 346–382, 2000.

[98] H. Kantz and T. Schreiber, *Nonlinear Time Series Analysis*. Cambridge University Press, 2003.

[99] E. B. Dam, M. Koch, and M. Lillholm, "Quaternions, interpolation and animation," tech. rep., University of Copenhegan, Denmark, 1998.

[100] T. A. Ell and S. J. Sangwine, "Hypercomplex Fourier transform of color images," *IEEE Transactions on Image Processing*, vol. 16, no. 1, pp. 22–35, 2007.

[101] C. Cheong-Took and D. P. Mandic, "The quaternion LMS algorithm for adaptive filtering of hypercomplex real world processes," *IEEE Transactions on Signal Processing*, vol. 57, no. 4, pp. 1316–1327, 2009.

[102] A. M. Sabatini, "Quaternion-based strap-down integration method for applications of inertial sensing to gait analysis," *Medical and Biological Engineering and Computing*, vol. 43, pp. 94–101, 2005.

[103] T. Gautama, D. P. Mandic, and M. M. V. Hulle, "The delay vector variance method for detecting determinism and nonlinearity in time series," *Physica D*, vol. 190, no. 3-4, pp. 167–176, 2004.

[104] D. P. Mandic, M. Chen, T. Gautama, M. V. Hulle, and A. Constantinides, "On the characterization of the deterministic/stochastic and linear/nonlinear nature of time series," *Proceedings of the Royal Society of London A*, vol. 464, pp. 1141–1160, 2008.

[105] K. S. Narendra and K. Parthasarathy, "Identification and control of dynamical systems using neural networks," *IEEE Transactions on Neural Networks*, vol. 1, no. 1, pp. 4–21, 1990.

Appendix A

Quaternions

A.1 Quaternion Representation and its Rotation Property

A quaternion $q \in \mathbb{H}$ is defined as $q = s + x\imath + y\jmath + z\kappa$ where s, x, y, and z are real numbers and $\imath$, $\jmath$, and κ are the unit vectors along the three vector dimensions [99]. Addition of quaternions is defined as

$$\begin{aligned} q_0 + q_1 &= (s_0 + x_0\imath + y_0\jmath + z_0\kappa) + (s_1 + x_1\imath + y_1\jmath + z_1\kappa) \\ &= (s_0 + s_1) + (x_0 + x_1)\imath + (y_0 + y_1)\jmath + (z_0 + z_1)\kappa. \end{aligned} \tag{A.1}$$

and the unit elements $\imath$, $\jmath$, and κ are related as

$$\begin{aligned} \imath\jmath\kappa = \imath^2 = \jmath^2 = \kappa^2 = -1, \imath\jmath = \kappa = -\jmath\imath, \\ \jmath\kappa = \imath = -\kappa\jmath, \\ \kappa\imath = j = -\imath\kappa. \end{aligned} \tag{A.2}$$

From A.1 and A.2, observe that the quaternion multiplication is not commutative. Subtraction of quaternions can be described as the addition and multiplication by -1.

The conjugate of a quaternion q is defined as

$$q^* = (s + x\imath + y\jmath + z\kappa)^* = s - x\imath - y\jmath - z\kappa. \tag{A.3}$$

whereas the norm of the quaternion is given by

$$\|q\| = \|s + x\imath + y\jmath + z\kappa\| = \sqrt{s^2 + x^2 + y^2 + z^2}. \tag{A.4}$$

Of special interest for this work is the unit quaternion, which has a unit norm and can be written as

$$q = \cos\theta + \mathbf{u}\sin\theta \tag{A.5}$$

where $\mathbf{u}$ is a 3D vector of unit length. A unit quaternion also has an exponential form given by

$$e^{\mathbf{u}\theta} = \cos\theta + \mathbf{u}\sin\theta. \tag{A.6}$$

The above equation can be seen as the generalization of Euler's identity for complex numbers, and represents the rotation of a vector by an angle 2θ, about a 3D unit vector $\mathbf{u}$. Figure A.1 illustrates the rotation of a vector $\mathbf{v}$ by an angle θ, about the line segment $\overline{OA}$. The direction of $\overline{OA}$ is specified by a 3D unit vector $\mathbf{u} \in \mathbb{R}^3$, and the rotated vector is represented by $\mathbf{v}'$, that is

$$\mathbf{v}' = q\mathbf{v}q^* = e^{\mathbf{u}\frac{\theta}{2}}\mathbf{v}(e^{\mathbf{u}\frac{\theta}{2}})^*. \tag{A.7}$$

Note that both the quaternion q and $-q$ represent the same rotation of a 3D vector $\mathbf{v}$.

A.2 Benefits of Using Quaternion Representation Over $\mathbb{R}$

Quaternions can be considered as a non-commutative extension of complex numbers, and have found applications in image processing [100], adaptive filtering [101], gait analysis [102], and animation [99]. In computer science, quaternions are being frequently employed for modelling of 3D rotations due to their efficiency in terms of computational requirements, and convenient mathematical representation which they offer. The convenience of representation and the efficiency of quaternions in representing 3D rotations, is therefore, the main reason for using them in our work. In the context of our present work, quaternions have been preferred over rotation matrices, also known as Direction Cosine matrices (DCM), and Eulers' angles, mainly due to the following reasons:

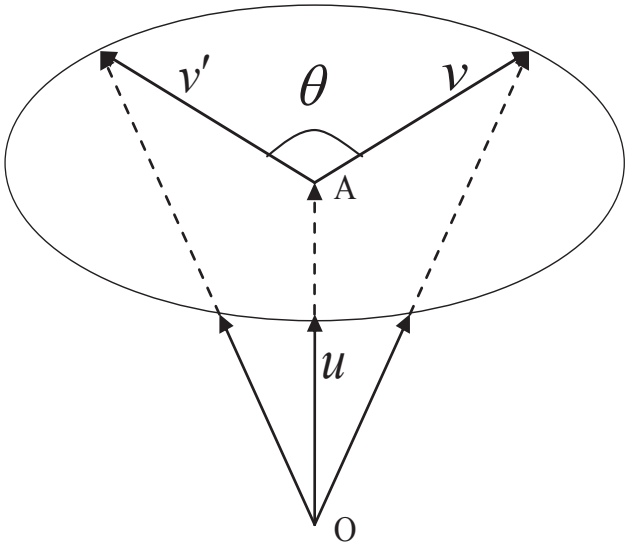

Figure A.1: Rotation of a 3D vector $\mathbf{v} \in \mathbb{R}^3$ about line segment $\overline{OA}$, by an angle θ.

- The most important reason for using quaternions in our work is that it gives a much more simplified and intuitive representation of rotation in terms of rotation axis and angle of rotation. This results in a more compact and convenient representation of 3D rotations as compared to rotation matrices and Euler's angle. Any rotation in 3D can be described by a rotation about an axis by an angle. Given an axis and an angle, the corresponding unit quaternion can be easily and directly constructed, whereas corresponding rotation matrices are normally indirectly obtained by conversion from unit quaternions. For example, the rotation matrix M corresponding to rotation about an axis $u = \frac{\imath+\jmath}{\sqrt{2}}$ by any given angle θ is very difficult to construct directly, and is normally obtained from corresponding quaternion $q = w + \imath x + \jmath y + \kappa$ using:

$$M = \begin{pmatrix} 1-2y^2-2z^2 & 2xy-2zw & 2xz+2yw \\ 2xy+2zw & 1-2x^2-2z^2 & 2yz-2xw \\ 2xz-2yw & 2yz+2xw & 1-2x^2-2y^2 \end{pmatrix} \tag{A.8}$$

whereas the quaternion q representing the same rotation can be easily and directly

constructed using:

$$q = e^{\mathbf{u}\theta}; \tag{A.9}$$

- Quaternions provide a more compact and simplified notation for 3D rotations as compared to rotation matrices. A unit quaternion represents rotation in 3D by using only four parameters. On the other hand, rotation matrices give coordinates of basis of new set of coordinate axes in terms of original, un-rotated coordinate axes, and therefore, require 9 parameters to represent rotations.

- When compared to rotation matrices, quaternion framework is much more robust to rounding errors which may accumulate during multiple operations. This is achieved because a slightly drifted quaternion, due to rounding error, can be easily normalised to again represent rotation, whereas rotation matrices have to be orthogonalised to represent rotation, which is computationally more demanding. This property along the availability of several interpolation tools for quaternions makes them suitable a suitable option for use in computer graphics.

- A quaternion framework provides a much faster and efficient method to implement 3D rotations as compared to rotation matrices.

Appendix B

Surrogate Data Methods and Delay Vector Variance (DVV)

B.1 Surrogate Data Methods

Surrogate data was initially proposed, in the context of nonlinear dynamics, for the purpose of linearization of the data to establish a robust statistical test for nonlinearity [96] [97] [98]. In its original formulation, the method generates 'surrogates' of the original data which are comparable to the measured data in certain respects, but which are also consistent with the specified null hypothesis; a null hypothesis of a linear Gaussian stochastic process is generally used for nonlinearity testing. Next, the values of a chosen nonlinear observable λ is computed both for the measured data, λ_0, and for the corresponding set of N surrogates, $\{\lambda_n\}_{n=1}^{N}$. Finally, if the value λ_0 falls significantly outside the distribution of the λ_n, then the null hypothesis can be rejected.

In the context of nonlinearity testing via surrogate data, the surrogates are a realisation of the null hypothesis of linearity. The three major aspects of the surrogate data method include: 1) the definition of the null hypothesis; 2) the method used to generate surrogate data; and 3) the test statistic. The two main types of null hypotheses include *simple* and *composite* null hypothesis. In simple null hypothesis the surrogate data is generated by a specific and known (linear) process, whereas the composite null hypothesis

asserts that the unknown underlying process is a member of a certain family of processes.

B.1.1 Iterative Amplitude Adjusted Fourier Transform (iAAFT) method

An important composite null hypothesis used in practice assumes that the series is generated by a linear stochastic process driven by Gaussian white noise. Since the linear signal properties can be fully described via its amplitude spectrum, this constraint can be approximated by forcing the original and surrogate time series to have identical amplitude spectra which leads to a simple and convenient method for generating surrogate data: it is based on phase randomisation of the Fast Fourier Transform (FFT) of the original time series and subsequently reconverting the resulting spectrum back to the time domain. This way, the surrogates are designed to have the same amplitude spectrum, ensuring linear properties similar to those of the original time series, but are otherwise random. This approach is referred to as the Fourier Transform (FT) surrogate data method.

In order to exclude false rejections caused due to changes in the signal distribution, Theiler [96] proposed an amplitude transform of the original time series such that the distribution becomes Gaussian prior to the FT method, which after phase randomization is reconverted to the original distribution via rank-ordering (Amplitude Adjusted Fourier Transform, or AAFT method).

In [97], a fixed point iteration scheme referred to as the iterative Amplitude Adjusted Fourier Transform (iAAFT) method is presented, which produces surrogates with identical signal distributions and approximately identical amplitude spectra as that of the original time series. Let $\{|S_k|\}$ be the spectrum of the original time series s, and $\{c_k\}$ the sorted version of the original time series: at every iteration j generate two series a) $r^{(j)}$ which has the correct signal distribution, and b) $s^{(j)}$, which has the correct amplitude spectrum. Starting with $r^{(0)}$, a random permutation of the time samples of the original time series, the iAAFT generation follows

1. compute the phase spectrum of $r^{(j-1)} \rightarrow \{\phi_k\}$
2. $s^{(j)}$ is the inverse transform of $\{|S_k| \exp(i\phi_k)\}$

3. $r^{(j)}$ is obtained by rank-ordering $s^{(j)}$ so as to match $\{c_k\}$

These steps are iterated until the discrepancy between $\{|S_k|\}$ and the amplitude spectrum of $r^{(j)}$ stops decreasing, which occurs after a finite number of iterations [97].

B.2 Delay Vector Variance

The Delay vector variance (DVV) method uses predictability of the signal in phase space to characterize the time series [103] [104]. Using the surrogate data methodology, so-called DVV plots and DVV scatter diagrams can be generated using the DVV method, *as a test statistic*, to examine the determinism/stochastisity and linearity/nonlinearity within a signal simultaneously. If m represents an optimal embedding parameter [98], then DVV method can be summarized as follows:

1. The mean, μ_d, and standard deviation, σ_d, are computed over all pairwise euclidean distances between delay vectors (DVs), $\|\mathbf{x}(i) - \mathbf{x}(j)\|$ $(i \neq j)$;

2. The sets of 'neighbouring' delay vectors $\Omega_k(r_d)$ are generated, such that, $\Omega_k(r_d) = \{\mathbf{x}(i) | \|\mathbf{x}(k) - \mathbf{x}(i)\| \leq r_d\}$, that is, sets which consists of all DVs that lie closer to $\mathbf{x}(k)$ than a certain distance r_d, taken from the interval $[max\{0, \mu_d - n_d\sigma_d\}; \mu_d + n_d\sigma_d]$, where n_d is a parameter controlling the span over which to perform the DVV analysis for N_{tv} uniformly spaced distances;

3. For every set $\Omega_k(r_d)$, the variance of the corresponding targets, $\sigma_k^2(r_d)$ is computed. The average over all sets $\Omega_k(r_d)$ normalised by the variance of the time series, σ_x^2, yields the target variance $\sigma^{*2}(r_d)$,

$$\sigma^{*2}(r_d) = \frac{\frac{1}{N}\sum_{k=1}^{N} \sigma_k^2(r_d)}{\sigma_x^2} \tag{B.1}$$

Variance measurements from (B.1) are considered valid only if the corresponding set $\Omega_k(r_d)$ contains atleast $N_o = 30$ DVs, to avoid unreliable estimates of variance.

The target variance is plotted as a function of standardized distance ($\frac{r_d - \mu_d}{\sigma_d}$) to get DVV plots in which the presence of strong deterministic component yields small target variances $\sigma^{*2}(r_d)$ for small spans r_d. To check for the nonlinearity within a signal, averaged DVV plots over a number of surrogate signals (generated using iAAFT method) can be generated and conveniently combined in a scatter diagram, where the horizontal axis corresponds to the target variance of the original time series and the vertical to that of the surrogate time series. DVV scatter diagram coincides with the bisector line if the original time series is similar in nature to the surrogate series.

For illustration, the DVV method is applied on a benchmark linear signal (AR(4)), given by

$$x(k) = 1.79x(k-1) - 1.85x(k-2) + 1.27x(k-3) - 0.41x(k-4) + n(k) \tag{B.2}$$

and a benchmark nonlinear signal, the Narendra Model Three [105], given by

$$z(k) = \frac{z(k-1)}{1 + z^2(k-1)} + x^3(k) \tag{B.3}$$

where $x(k)$ denotes the AR(4) signal defined above and $n(k) \sim \mathcal{N}(0, 1)$. The average DVV plots, computed over 25 iAAFT-based surrogates for these two benchmark signals are shown, respectively, in Figure B.1(a) and Figure B.1(b), whereas, the DVV scatter plots are shown in in Figure B.1(c) and Figure B.1(d). As expected, the scatter plot for the linear AR(4) model coincides with the bisector line; on the other hand, the scatter plot of nonlinear Narendra model deviates from the bisector line.

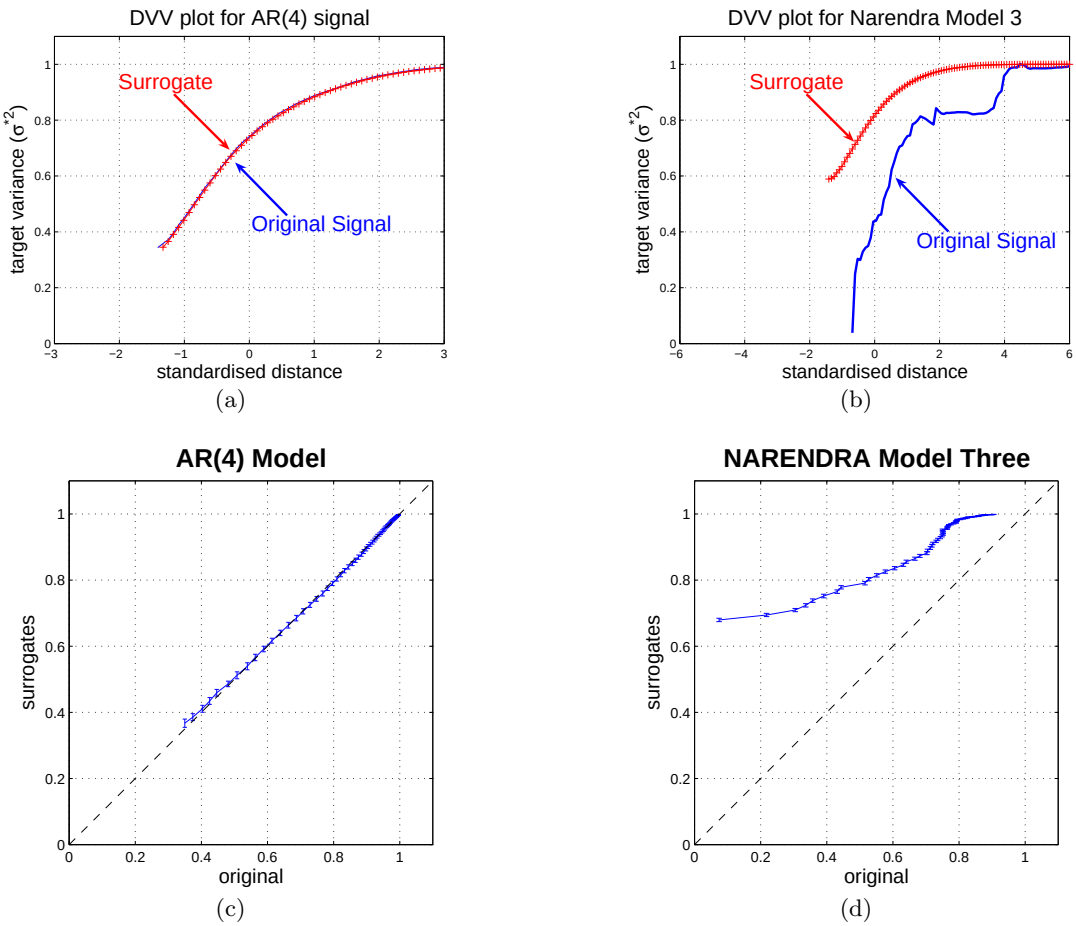

Figure B.1: The DVV plots (top row) and DVV scatter plots (bottom row) for linear AR4 (left) and nonlinear Narendra (right) signals.

Appendix C

Low-Discrepancy Hammersley Sequences

The discrepancy can be seen as a measure of irregularity of the distribution, or in other words, a quantitative measure for the deviation from the uniform distribution. It is important in quasi-Monte Carlo methods which are used to generate well-chosen deterministic point sets for solving numerical integration problems. The low-discrepancy quasi-Monte Carlo methods yield superior results as compared to Monte Carlo methods (using random sequences) in terms of deterministic and improved (lower) error bounds and their lower computational cost.

The discrepancy $D_N(\mathcal{B}; P)$ of a point set P containing N points, consisting of $x_1, x_2, \ldots, x_N \in I_s$ where I_s is the closed s-dimensional unit cube, is given by

$$D_N(\mathcal{B}; P) = \sup_{B \in \mathcal{B}} \left| \frac{A(\mathcal{B}; P)}{N} - \lambda_s(B) \right| \tag{C.1}$$

where $\mathcal{B}$ is a family of Lebesgue-measurable subsets of I_s and $A(\mathcal{B}; P)$ is the number of elements of the set $x_1, x_2, \ldots, x_N \in I_s$ in $\mathcal{B}$. The resulting value of D_N is always between $0 \leq D_N(\mathcal{B}; P) \leq 1$.

The error analysis of the quasi-Monte Carlo integration shows that the error bounds are small for point sets with low discrepancy measure. This leads to an informal definition

of the *low-discrepancy sequences* as those having lower value of $D_N(\mathcal{B}; P)$.

Some classical constructions for low-discrepancy sequences include: van der Corput sequence, only valid for univariate sequences; Halton sequence, which is a generalisation of van der Corput sequence for higher dimensions; and Hammersley sequence.

C.1 The van der Corput Sequence

If n is a positive integer $n \geq 0$, then it can be represented in base b using

$$n = \sum_{j=0}^{L-1} a_j(n) b^j \tag{C.2}$$

For an integer $b \geq 2$, a radical inverse function ϕ_b in base b can then be defined as

$$\phi_b(n) = \sum_{j=0}^{L-1} a_j(n) b^{-j-1} \text{ for all } n \geq 0, \tag{C.3}$$

The van der Corput sequence in base b is the sequence $x_1, x_2, \ldots$ with $x_n = \phi_b(n)$ for all $n \geq 0$.

C.2 Halton Sequence

Halton sequence is a natural generalisation of the van der Corput sequence in higher dimensions. Let $s \geq 1$ be the given dimension and $b_1, \ldots, b_s$ be arbitrary coprime integers ≥ 2. Then the Halton sequence in the bases $b_1, \ldots, b_s$ can be defined as the sequence $\mathbf{x}_1, \mathbf{x}_2, \ldots$ with

$$\mathbf{x}_n = \big(\phi_{b_1}(n), \ldots, \phi_{b_s}(n)\big) \text{ for all } n \geq 0, \tag{C.4}$$

For $s = 1$, this definition reduces to the van der Corput sequence given in equation (C.3).

C.3 Hammersley Sequence

Let $b_1, \ldots, b_{s-1}$ be the coprime positive integers ≥ 2. For a given value of s and N, the multidimensional Hammersley set of size N is defined by

$$\mathbf{x}_n = \left(\frac{n}{N}, \phi_{b_1}(n), \ldots, \phi_{b_{s-1}}(n)\right) \text{ for } n = 0, \ldots, N-1, \tag{C.5}$$

If S represents a Halton sequence, generated for bases $b_1, \ldots, b_s$, and P denotes the Hammersley sequence for bases $b_1, \ldots, b_{s-1}$, then their discrepancy estimates are given by

$$D_N^*(S) \leq A_s \frac{(\log N)^s}{N} \tag{C.6}$$

$$D_N^*(P) \leq A_{s-1} \frac{(\log N)^{s-1}}{N} \tag{C.7}$$

The discrepancy bounds for low-discrepancy Halton and Hammersley sequences serve as benchmarks for the construction of other low-discrepancy point sets, and its error bound $O(\frac{(\log N)^{s-1}}{N})$ provides a significant improvement over Monte Carlo error bound $O(N^{-1/2})$.

The original Hammersley sequence generates the point set in the range of $[0, 1)$ and hence, therefore, has to be modified to produce the directional vectors on $(n-1)$-sphere. For a particular case of a 2-sphere (three dimensional sphere), this is achieved by first performing a linear scaling of the sequence to the cylindrical domain $(\phi, t) \in [0, 2\pi) \times [-1, 1]$. The transformation from (ϕ, t) to the unit sphere is then achieved via the following radial projection:

$$(\phi, t) \mapsto (\sqrt{1-t^2}\cos(\phi), \sqrt{1-t^2}\sin(\phi), t)^T \tag{C.8}$$

To generate the uniform samples on a general n-sphere, a linear mapping to $(n-1)$ angular coordinates is first done, and then the direction vectors based on these coordinates are generated.